THE CANADIAN GEOID

P. VANICEK
A. KLEUSBERG
R. G. CHANG
H. FASHIR
N. CHRISTOU
M. HOFMAN
T. KLING
T. ARSENAULT

December 1987

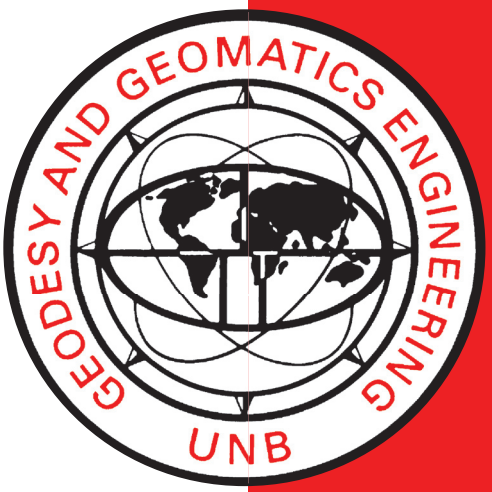

TECHNICAL REPORT
NO. 129

PREFACE

In order to make our extensive series of technical reports more readily available, we have scanned the old master copies and produced electronic versions in Portable Document Format. The quality of the images varies depending on the quality of the originals. The images have not been converted to searchable text.

THE CANADIAN GEOID

Petr Vaníček
Alfred Kleusberg
Ruey-Gang Chang
Hassan Fashir
Nick Christou
Marco Hofman
Thomas Kling
Terry Arsenault

Department of Geodesy and Geomatics Engineering
University of New Brunswick
P.O. Box 4400
Fredericton, N.B.
Canada
E3B 5A3

December 1987
Latest Reprinting March 1995

TABLE OF CONTENTS

LIST OF TABLES

LIST OF FIGURES

1. INTRODUCTION

This technical report is the final contract report for the research done on the Canadian Geoid partly for the Geodetic Survey of Canada, under contract DSS #24ST.23244-4-4020. The Scientific Authority for this contract was Dr. Demitris Delikaraoglou; the Principal Investigator was Petr Vaníček. A major part of the research was sponsored by the Principal Investigator's Natural Sciences and Engineering Research Council operating grant #IS 0115.

Under the terms of the contract, we were supposed to develop a software package for an analytical solution for the geoid in Canada. In addition, we were supposed to:

(1) Deliver a detailed report on the theoretical formulation of the models that are implemented and tested in the software package.

(2) Deliver a detailed report on the analysis of existing gravity, deflections of the vertical, Doppler derived undulation, GEOS-3 and SEASAT altimetry and their combination for the estimation of the accuracy of the geoid heights achievable in different parts of Canada by applying the proposed methodology.

(3) Deliver a graphical representation (e.g., computer plot) of the analytical geoid solution for Canada obtained by the method.

(4) Supply on tape the results of the point evaluation of the geoid undulations and the deviation of the vertical on a selected mesh of points.

This report addresses points (1) to (3).

We have developed a technique for computing point values of a gravimetric geoid to a very high short wavelength accuracy. These gravimetric values have been tested with respect to the Doppler derived values, SEASAT altimetry, and Rapp's 180° by 180° solutions. To the extent to which these 'external standards' are reliable, our gravimetric geoid shows a very high degree of integrity, agreeing with the 'external

standards' well within the indicated accuracies, which demonstrates the validity of our technique and tests the developed software.

To obtain the utmost accuracy of the gravimetric solution, it is necessary, among other things, to apply corrections for atmospheric attraction, topographic effect, and indirect effect. The evaluation of these corrections is very computationally intensive, particularly the correction for topographic effect. These corrections may change the value of geoidal height by several decimetres, and their neglect results in both long- and short-wavelength distortions. The short-wavelength distortions are above the short-wavelength noise level; the long-wavelength ones are not.

We have applied these corrections when testing our solution against the Doppler derived values and have seen, as expected, an improved fit. We have not, however, applied these corrections to all the point values computed on a 10' by 10' grid, generated as the background for the analytical solution. It would have been prohibitively expensive, from the computer time point of view and, as such, unjustified vis-à-vis the accuracy of the other data, i.e., the Doppler derived geoidal heights, the deflections, and the satellite altimetry.

The gravimetric geoid, as we present it here, appears to be very good; it is clearly superior to all our previous attempts (John [1976], Sosa-Torres [1977], Vaníček and John [1983], etc.). The amount of detail discernible on the presented plots, based on the 10' by 10' mesh, should make them very interesting to interpretative geophysicists—see, for instance, the clearly defined structure following the lower reaches of the St. Lawrence River. In spite of this, the gravimetric solution is not the best we can produce because of the reasons described earlier.

It was considered, therefore, computationally wasteful to merge this gravimetric solution with the other kinds of data in an analytical solution for the whole of Canada.

The main reason is that the gravimetric geoid contains too much detail (many short wavelength features) to be properly modellable by an algebraic surface. We have, of course, developed the software (really modified some existing software) to do it, but applied it to only a few blocks to demonstrate the technique. The coverage can be easily extended when the decision is taken to expend more computer time on the problem. We also suggest an alternative approach to the inclusion of the other kinds of data.

We have made the decision to refer the geoid to the Geodetic Reference System 1980 (GRS80). We believe that this will make the results useful to the largest variety of users.

The software developed for the task at hand is described in the Department of Surveying Engineering Technical Memorandum 10 [Chang et al., 1986].

2. THE GRAVIMETRIC GEOID

2.0 Introduction

The *gravimetric geoid*, represented by its undulations N_G with regard to a reference ellipsoid, is the geoid computed from observed gravity. The computational procedure can be visualized as a partial solution of the geodetic boundary value problem (e.g., Heiskanen and Moritz [1967]; Vaníček and Krakiwsky [1982]).

Defining the disturbing potential T by

$$T = W - U \,, \tag{2.1}$$

where U is some appropriately chosen reference potential and, assuming the centrifugal potentials in W and U to be identical, the Laplace equation

$$\nabla^2 T = 0 \tag{2.2}$$

is valid outside the gravitating masses. We assume for these derivations that all masses are inside the geoid.

If we have chosen the reference potential U in such a manner as to yield on the reference ellipsoid a constant potential value U_0 identical to the gravity potential W_0 on the geoid, we can express the geoid undulation by

$$N = \frac{T_B}{\gamma_{B_0}}, \tag{2.3}$$

where B and B_0 denote points on the geoid and the reference ellipsoid, respectively; γ is the normal derivative of the reference potential

$$\gamma = -\frac{\partial U}{\partial n}; \tag{2.4}$$

n is the outer ellipsoidal normal.

From eqn. (2.1) we obtain

$$\left.\frac{\partial T}{\partial H}\right|_B = \left.\frac{\partial W}{\partial H}\right|_B - \left.\frac{\partial U}{\partial H}\right|_B , \tag{2.5}$$

with H being the orthometric height. In spherical approximation we can replace

$$\left.\frac{\partial U}{\partial H}\right|_B = \left.\frac{\partial U}{\partial n}\right|_B = -\gamma_B , \tag{2.6}$$

and with the gravity g on the geoid being

$$g_B = -\left.\frac{\partial W}{\partial H}\right|_B \tag{2.7}$$

we obtain, from eqns. (2.5) and (2.6)

$$\begin{aligned} g_B - \gamma_{B_o} &\doteq -\left.\frac{\partial T}{\partial H}\right|_B + \gamma_B - \gamma_{B_o} \\ &= -\left.\frac{\partial T}{\partial H}\right|_B + \left.\frac{\partial \gamma}{\partial n}\right|_{B_o} N . \end{aligned} \tag{2.8}$$

In the spherical approximation, we replace

$$\left.\frac{\partial \gamma}{\partial n}\right|_{B_o} \doteq -\frac{2}{R}\gamma_{B_o} \tag{2.9}$$

with a mean earth radius R. Inserting eqn. (2.9) into eqn. (2.8) and denoting the gravity anomaly $g_B - \gamma_{B_o}$ by Δg we get the final equation

$$\Delta g \doteq -\left.\frac{\partial T}{\partial H}\right|_B - \frac{2}{R} T_B , \tag{2.10}$$

where we have used eqn. (2.3). Equation (2.10) shows that the gravity anomalies Δg are boundary values (of mixed type) for the solution of eqn. (2.2) at the unknown **geoidal** surface (and not ellipsoidal as wrongly stated by Vaníček and Krakiwsky [1982]). A classical procedure to obtain the geoid from boundary values (2.5) is the Stokes integration (cf. Vaníček and Krakiwsky [1982])

$$N(\phi, \lambda) = \frac{R}{4\pi\gamma} \iint_{\varepsilon} \Delta g(\phi', \lambda') \, S(\psi) \, d\upsilon \,, \tag{2.11}$$

where R and γ are mean earth's radius and normal gravity, respectively, ε is the unit sphere, ψ is the spherical distance between (ϕ, λ) and (ϕ', λ'); and $S(\psi)$ is the Stokes function having a series expansion

$$S(\psi) = \sum_{l=2}^{\infty} \frac{2l + 1}{l - 1} P_l(\cos \psi) \,. \tag{2.12}$$

Here $P_l(x)$ are Legendre polynomials of degree l (e.g., Abramowitz and Stegun [1964]).

We may separate the geoid undulations (2.11) in a low degree reference surface N^l and the high degree contribution δN^l according to

$$N(\phi, \lambda) = N^l(\phi, \lambda) + \delta N^l(\phi, \lambda) \tag{2.13}$$

where

$$N^l(\phi, \lambda) = \frac{R}{4\pi\gamma} \iint_{\varepsilon} \Delta g(\phi', \lambda') \sum_{k=2}^{l} \frac{2k+1}{k-1} P_k(\cos\psi) \, d\upsilon \tag{2.14}$$

$$\delta N^l(\phi, \lambda) = \frac{R}{4\pi\gamma} \iint_{\varepsilon} \Delta g(\phi', \lambda') \sum_{k=l+1}^{\infty} \frac{2k+1}{k-1} P_k(\cos\psi) \, d\upsilon \,. \tag{2.15}$$

Low degree gravity field constituents are rather well known from satellite geodesy. Thus we assume in the sequel N^l to be known and δN^l to be determined from gravity anomalies.

2.1 Satellite Solution as a Reference Spheroid

2.1.1 The Description of a Satellite Solution

Global gravity field solutions are usually given in terms of an expansion of the gravitational potential in spherical harmonics

$$V(r, \phi, \lambda) = \frac{GM}{r} \sum_{n=0}^{\infty} \sum_{m=0}^{n} \left(\frac{a}{r}\right)^n (J_{nm} Y^c_{nm}(\phi, \lambda) + K_{nm} Y^s_{nm}(\phi, \lambda)) \qquad (2.16)$$

where GM is the product of the gravitational constant and the mass of the earth; a is the mean earth equatorial radius; Y^c_{nm} and Y^s_{nm} are normalized spherical harmonic functions, and J_{nm}, K_{nm} are potential coefficients [Vaníček and Krakiwsky, 1982].

In practical applications, the series (2.16) is truncated at some $n=N$ and the potential coefficients of degree 1 are forced to be zero by selecting the CT-coordinate system

$$J_{1m} = K_{1m} = 0 \,. \qquad (2.17)$$

Since $Y_{00} = 1$, $Y^s_{00} = 0$, and $J_{00} = 1$, we obtain, from eqn. (2.16),

$$V(r, \phi, \lambda) = \frac{GM}{r}\{1 + \sum_{n=2}^{N} \sum_{m=0}^{n} \left(\frac{a}{r}\right)^n (J_{nm} Y^c_{nm} + K_{nm} Y^s_{nm})\} \,. \qquad (2.18)$$

2.1.2 The Choice of GEM9

Out of the variety of potential field models published so far, we have chosen to adopt the GEM9 coefficient set [Lerch et al., 1979] as probably the most complete, purely satellite solution available. More recently published gravity field models, tailored for special applications in satellite geodesy, seem to be inadequate for our purposes.

GEM9 is complete through degree $N=20$. This implies that the smallest gravity field features represented in GEM9 have a spatial extension of about 9° spherical distance or 1000 km.

2.1.3 Computation of GEM9 Spheroid Undulations Relative to the GRS80 Ellipsoid.

The truncated geoid undulations of a field (2.18) with respect to the GRS80 ellipsoid [Moritz, 1980] are given by the Bruns formula

$$N = \frac{T_B}{g_{B_o}} \tag{2.19}$$

with the disturbing potential (cf. eqn. (2.1)) T_B at the geoid

$$T = W - U = V - (U - Z) \tag{2.20}$$

where we used Z to denote the centrifugal potential. The gravitational part of the GRS80 normal potential is given by

$$U - Z = \frac{GM^*}{r}\{1 - \sum_{n=2,4,6,8} (\frac{a^*}{r})^n J^*_{no} Y^c_{no}(\phi, \lambda)\} . \tag{2.21}$$

We have marked the GRS80 values for GM, a, and J_{no} by an asterisk to distinguish them from the GEM9 parameters.

Combining eqns. (2.18) and (2.21) according to eqn. (2.20), we obtain the disturbing potential T as

$$T(r, \phi, \lambda) = (\frac{GM}{r} - \frac{GM^*}{r}) + \frac{GM}{a} \sum_{n=2}^{20} \sum_{m=0}^{n} (\frac{a}{r})^{n+1} (J_{nm} Y^c_{nm} + K_{nm} Y^s_{nm}) + \frac{GM^*}{a^*} \sum_{n=2,4,6,8} (\frac{a^*}{r})^{n+1} J^*_{no} Y^c_{no} \tag{2.22}$$

$$= (\frac{GM}{r} - \frac{GM^*}{r}) + \frac{GM}{a} \sum_{n=2}^{20} \sum_{m=0}^{n} (\frac{a}{r})^{n+1} (J'_{nm} Y^c_{nm} + K_{nm} Y^s_{nm}) . \tag{2.23}$$

The J'_{nm} are different than J_{nm} for m=0 and n=2,4,6,8 only. To compute these new values, we first have to normalize the potential coefficients of the normal gravitational potential

$$J^*_{no} = \frac{1}{\sqrt{(2n+1)}} J^*_{no} \quad . \tag{2.24}$$

Comparing eqns. (2.22) through (2.24) we find for n=2,4,6,8

$$J'_{no} = J_{no} + \frac{GM^*}{GM} \left(\frac{a^*}{a}\right)^n J^*_{no} \quad . \tag{2.25}$$

Taking numerical values for a, a^*, GM, GM^* from Mortiz [1980] and Lerch et al. [1979]

a = 6 378 140 m

a^* = 6 378 137 m

GM = 3 986 006.4 x $10^8 \frac{m^3}{s^2}$

GM^* = 3 986 005.0 x $10^8 \frac{m^3}{s^2}$

we find

$$\frac{GM^*}{GM}\left(\frac{a^*}{a}\right)^n = (1 - 0.351 \times 10^{-6})(1 - 0.470 \times 10^{-6})^n$$

$$\doteq 1 - (0.351 + n \cdot 0.470) \times 10^{-6} \quad .$$

Applying this factor to the normalized GRS80 potential coefficients

J^*_{20} = 484.166 86 x 10^{-6}

J^*_{40} = - 0.79030 $\times 10^{-6}$

J^*_{60} = 0.00169 $\times 10^{-6}$

$$J^{*}_{80} = -3.5 \times 10^{-12},$$

taking the GEM9 potential coefficients from Lerch et al. [1979], we obtain the following set of J'_{no}

$$J'_{20} = 0.000\,68 \times 10^{-6}$$

$$J'_{40} = -0.248\,76 \times 10^{-6} \qquad (2.27)$$

$$J'_{60} = -0.149\,52 \times 10^{-6}$$

$$J'_{80} = J_{80}\,.$$

Since the first term in eqn. (2.23) represents merely a constant change $U_0 = T_0$ in the reference potential between GRS80 and GEM9, we can finally write

$$T(r, \phi, \lambda) = T_0 + \frac{GM}{r} \sum_{n=2}^{20} \sum_{m=0}^{n} \left(\frac{a}{r}\right)^n \left(J'_{nm}\, Y^{c}_{nm}(\phi, \lambda) + K_{nm}\, Y^{s}_{nm}(\phi, \lambda)\right) \qquad (2.28)$$

with J'_{no} given by eqn. (2.27) for n=2,4,6 and $J'_{nm} = J_{nm}$ for $n \neq 2,4,6$.

Equations (2.19) and (2.28) are solved for $N(\phi, \lambda)$ using the subroutine POT [Tscherning et al., 1938]. This program evaluates also the gravity disturbance

$$\delta g_B = g_B - \gamma_B\,. \qquad (2.29)$$

In section 2.2, we will need the gravity anomaly computed for the disturbing potential T. In spherical approximation, we have

$$\delta g_B = -\left.\frac{\partial T}{\partial H}\right|_B,$$

and eqn. (2.10) gives

$$\Delta g = \delta g_B - \frac{2}{R} T_B\,. \qquad (2.30)$$

2.1.4 Accuracy of the Satellite Derived Spheroid

From now on we will denote the geoid undulations (really reference spheroid undulations) and gravity anomalies derived from the GEM9 coefficient set J'_{nm}, K_{nm} by the subscript 20, to indicate the degree of the reference field used.

In spherical approximation, we obtain from eqns. (2.19) and (2.28)

$$N_{20}(\phi, \lambda) = R \sum_{n=2}^{20} \sum_{m=0}^{n} (J'_{nm} Y^{c}_{nm}(\phi, \lambda) + K_{nm} Y^{s}_{nm}(\phi, \lambda)) \tag{2.31}$$

with R being some mean earth radius.

The accuracy of N_{20} depends on the variances and covariances of the potential coefficients J'_{nm} and K_{nm}. Assuming statistically independent potential coefficients, the law of error propagation gives

$$\sigma^2_{N_{20}}(\phi, \lambda) = R^2 \sum_{n=2}^{20} \sum_{m=0}^{n} [(\sigma^{c}_{nm} Y^{c}_{nm}(\phi, \lambda))^2 + (\sigma^{s}_{nm} Y^{s}_{nm}(\phi, \lambda))^2] \,. \tag{2.32}$$

To estimate the accuracy of N_{20}, we assume an average value for the standard deviation of potential coefficients of degree n

$$\forall m: \; \sigma^{c}_{nm} = \sigma^{s}_{nm} = \sigma_n \,, \tag{2.33}$$

and compute the variance of the position dependent spheroid undulation standard deviation according to

$$\bar{\sigma}^2_{N_{20}} = \frac{1}{4\pi} \iint_{\varepsilon} \sigma^2_{N_{20}}(\phi, \lambda) \, d\upsilon \,. \tag{2.34}$$

Since

$$\iint_{\varepsilon} Y^{c}_{nm}(\phi, \lambda) \, d\upsilon = \iint_{\varepsilon} Y^{s}_{nm}(\phi, \lambda) \, d\upsilon = 4\pi \,, \tag{2.35}$$

we obtain, from eqns. (2.32) minus (2.34) the final result

$$\bar{\sigma}^2_{N_{20}} = R^2 \sum_{n=2}^{20} (2n + 1)\, \sigma_n^2 \,. \tag{2.36}$$

The standard deviations σ_n of GEM9 potential coefficients of degree n are plotted in Figure 2.1. Their cumulative effect on the computation of GEM9 spheroid undulation according to eqn. (2.36) is shown in Figure 2.2. It can be seen that the commission error grows to about 1.75 m if the spheroid is computed complete to degree 20. We note, however, that this is purely a long wavelength (≥1000 m) error.

2.2 Contribution from Terrestrial Gravity

This section is concerned with the evaluation of δN^I according to eqn. (2.15). One requirement for the validity of this equation is that all terrestrial masses are inside the geoid. To meet this requirement, we may deploy the following process:

(a) Remove the topographic masses above the geoid, e.g., by condensing them at the geoid. This leads to a change δg_T in gravity anomalies.

(b) Solve the approximate problem posed by eqn. (2.2) with boundary conditions (2.10) given by

$$\Delta g = \Delta g_0 - \delta g_T,$$

where we have denoted by Δg_0 the 'observed' gravity anomaly. The integration (2.11) using these Δg gives the so-called *co-geoid.*

(c) The difference between the geoid and the co-geoid is called the indirect effect. It is due to the change in mass distribution (see (a)) and can be computed from the known distribution of topographical masses.

In addition, we have to account for the fact that the satellites 'see' the gravity field from the outside of the atmosphere while terrestrial measurements are carried out inside the atmosphere. To put them both on the same basis, we correct the observed Δg_0 for δg_A, the attraction of the atmospheric masses. In other words, the atmosphere

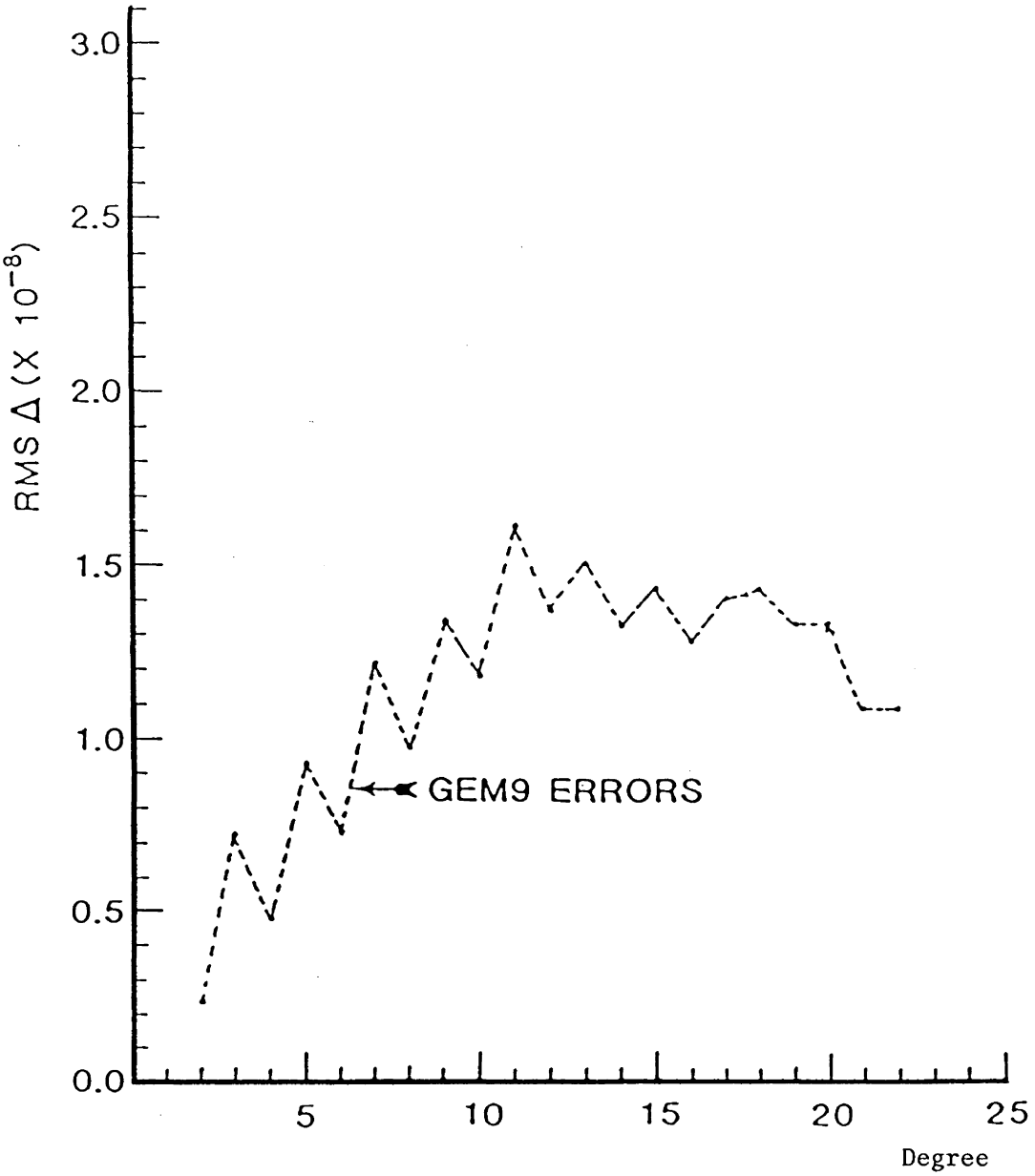

Figure 2.1: Accuracy of GEM9 potential coefficients[Lerch et al., 1984].

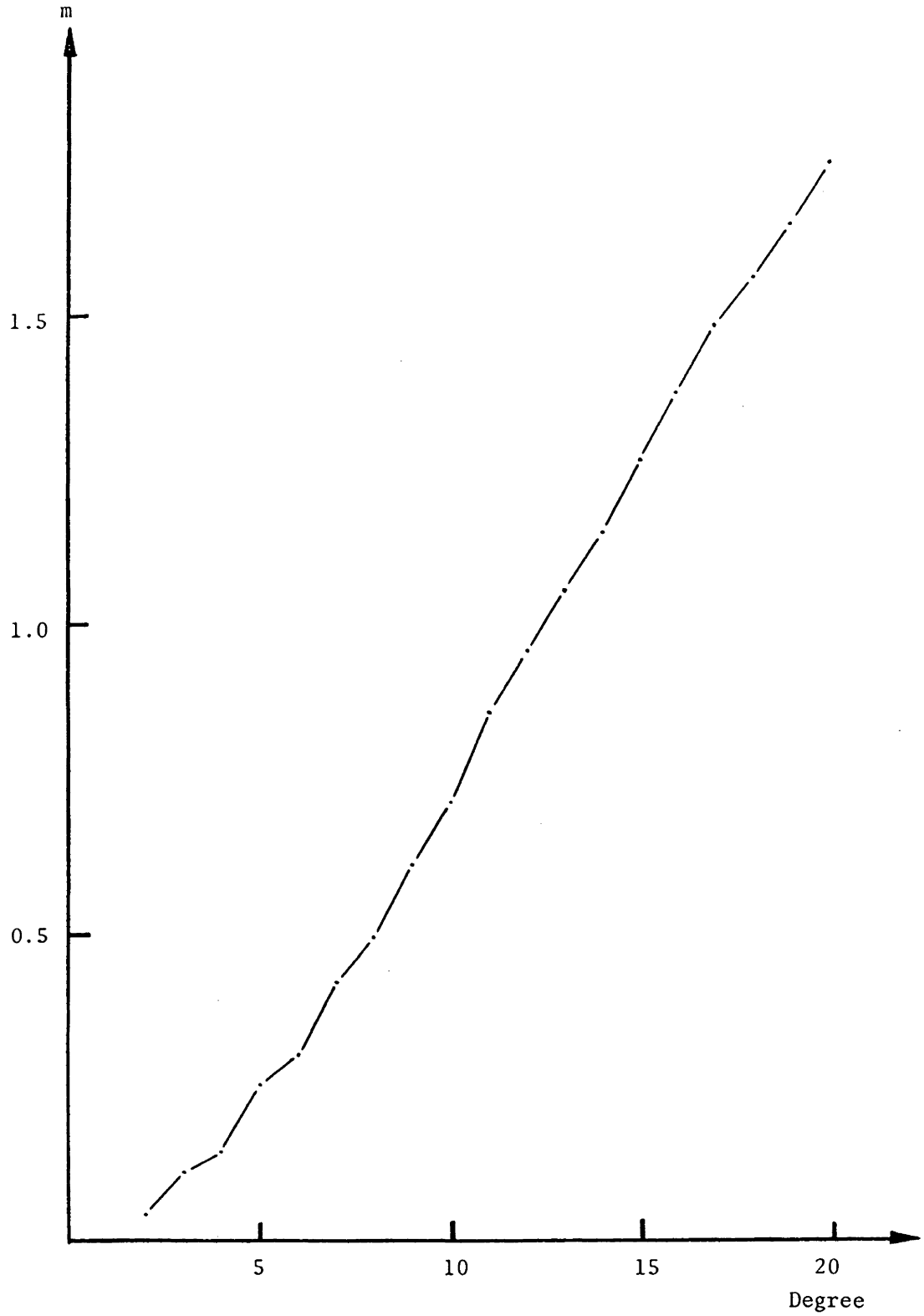

Figure 2.2: Geoid errors induced by GEM9 potential coefficient errors

must be accounted for, in the same way as the topographic masses, to satisfy the boundary value problem.

The computational procedures for evaluating the atmospherical attraction effect δg_A, the topographical attraction effect δg_T, and the indirect effect will be described in sections 2.2.3, 2.2.4, and 2.2.5, respectively. The following sections, 2.2.1 and 2.2.2, are devoted to the derivation of the spheroidal Stokes kernel S_l, its modification for truncated integration, and the numerical evaluation of the spheroidal Stokes integral.

2.2.1 Spheroidal Stokes's Kernel

The spheroidal Stokes kernel is given by (cf. eqn. (2.15))

$$S_l(\psi) = \sum_{k=l+1}^{\infty} \frac{2k+1}{k-1} P_k(\cos\psi) . \tag{2.37}$$

Using the series expansion of the (ellipsoidal) Stokes function $S(\psi) = S_l(\psi)$ (eqn. (2.12)) we may rewrite eqn. (2.37) as

$$S_l(\psi) = S(\psi) - \sum_{k=2}^{l} \frac{2k+1}{k-1} P_k(\cos\psi) . \tag{2.38}$$

The two functions $S(\psi)$ and $S_l(\psi)$ are shown in Figure 2.3. It is obvious that the spheroidal function $S_l(\psi)$ tapers off more rapidly than $S(\psi)$ for increasing spherical distance ψ. Thus we can expect that a truncation of the spheroidal integration (2.15) at a certain spherical distance ψ_0 leads to smaller truncation errors compared to the truncation of the ellipsoidal integration (2.11). The following section investigates these truncation errors and minimizes them by modifying the spheroidal Stokes function $S_l(\psi)$.

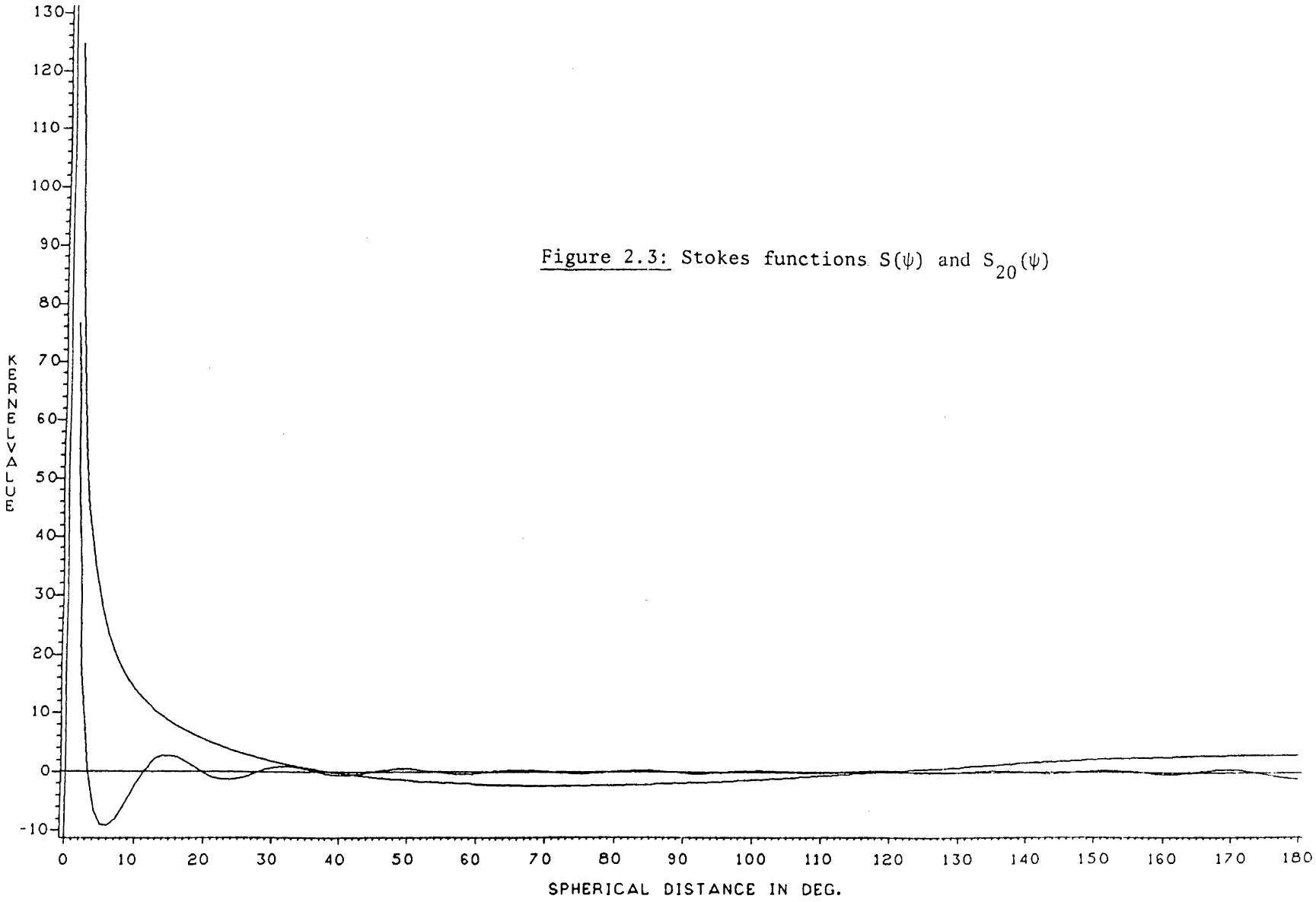

Figure 2.3: Stokes functions $S(\psi)$ and $S_{20}(\psi)$

2.2.2 Modification of the Spheroidal Kernel

The geoid contribution from terrestrial gravity observations is evaluated by integration according to eqn. (2.15)

$$\delta N^l = \frac{R}{4\pi\gamma} \int_{\psi=0}^{\pi} S_l(\psi) \int_{\alpha=0}^{2\pi} \Delta g(\psi, \alpha)\, d\alpha \sin\psi\, d\psi, \tag{2.39}$$

where we have switched to a polar coordinate system centred at the point of geoid evaluation.

Writing the gravity anomalies in an expansion of surface spherical harmonics

$$\Delta g(\psi, \alpha) = \sum_{i=2}^{\infty} \Delta g_i (\psi, \alpha) \tag{2.40}$$

$$\Delta g^l(\psi, \alpha) = \sum_{i=l+1}^{\infty} \Delta g_i (\psi, \alpha) \tag{2.41}$$

we realize that due to the orthogonality of spherical harmonics on the sphere the gravity anomaly constituents up to degree l do not contribute to δN^l. Thus we can replace the Δg in eqn. (2.39) by Δg^l defined by eqn. (2.41)

$$\delta N^l = \frac{R}{4\pi\gamma} \int_{\psi=0}^{\pi} S_l(\psi) \int_{\psi=0}^{\pi} \Delta g^l(\psi, \alpha)\, d\alpha \sin\psi\, d\psi\ . \tag{2.42}$$

Abbreviating

$$\frac{R}{2\gamma} = K$$

$$\frac{1}{2\pi} \int_{\alpha=0}^{2\pi} \Delta g^l(\psi, \alpha)\, d\alpha = \bar{\Delta g}^l(\psi) \tag{2.43}$$

we obtain finally

$$\delta N^l = K \int_{\psi=0}^{\pi} S_l(\psi)\, \bar{\Delta g}^l(\psi) \sin\psi\, d\psi. \tag{2.44}$$

Since we usually do not have gravity data all over the sphere, and want to save computer time anyway, we want to limit the integration area to a spherical cap $\psi \leq \psi_0$. To minimize the resulting truncation error ΔN, we modify the integration kernel $S_l(\psi)$ by low degree constituents

$$S_l^m(\psi) = S_l(\psi) - S_l^*(\psi) \tag{2.45}$$

such that

$$S_l^*(\psi) = \sum_{i=0}^{l} \frac{2i+1}{2} t_i P_i(\cos\psi) \tag{2.46}$$

with coefficient t_i to be determined.

Integrating within a spherical cap of radius ψ_0 we obtain

$$\delta N^l = K \int_{\psi=0}^{\psi_0} S_l^m(\psi)\, \Delta\bar{g}^l(\psi) \sin\psi\, d\psi + \Delta N \tag{2.47}$$

with the truncation error being equal to

$$\Delta N = K \int_{\psi=\psi_0}^{\pi} S_l^m(\psi)\, \Delta\bar{g}^l(\psi) \sin\psi\, d\psi \quad . \tag{2.48}$$

The coefficients t_i of the expansion (2.46) are now determined by minimizing the truncation error ΔN in an r.m.s. sense. The r.m.s. truncation error is the square root of

$$\Delta\bar{N}^2 = K^2 \left\{ \int_{\psi=\psi_0}^{\pi} S_l^m(\psi)\, \Delta\bar{g}^l(\psi) \sin\psi\, d\psi \right\}^2 . \tag{2.49}$$

The Schwarz inequality gives

$$\Delta\bar{N}^2 \leq K^2 \left\{ \int_{\psi=\psi_0}^{\pi} [S_l^m(\psi)]^2 \sin\psi\, d\psi \right\} \left\{ \int_{\psi=\psi_0}^{\pi} [\Delta g^l]^2 \sin\psi\, d\psi \right\} \tag{2.50}$$

and minimizing the right-hand side of eqn. (2.50) with respect to the coefficients t_i leads to the equation system:

$$\int_{\psi=\psi_0}^{\pi} S_l^m(\psi) \frac{\partial S_l^m(\psi)}{\partial t_i} \sin\psi \, d\psi = 0; \quad i=0,1,...,l \, . \tag{2.51}$$

Substituting for the modified kernel from eqns. (2.45) and (2.46), we obtain:

$$\int_{\psi=\psi_0}^{\pi} \left(S_l(\psi) P_i(\cos\psi) - \sum_{k=0}^{l} \frac{2k+1}{2} t_k P_k(\cos\psi) P_i(\cos\psi) \right) \sin\psi \, d\psi = 0 \, . \tag{2.52}$$

Abbreviating

$$\int_{\psi=\psi_0}^{\pi} S_l(\psi) P_i(\cos\psi) \sin\psi \, d\psi = Q_i^l(\psi_0) \tag{2.53}$$

$$\int_{\psi=\psi_0}^{\pi} P_i(\cos\psi) P_k(\cos\psi) \sin\psi \, d\psi = e_{ik}(\psi_0) \tag{2.54}$$

where both Q and e are functions of the integration radius ψ_0 only, leads to the linear equation system

$$\sum_{k=0}^{l} \frac{2k+1}{2} e_{ik}(\psi_0) \, t_k = Q_i^l(\psi_0) \, , \tag{2.55}$$

which can be solved for the coefficients t_k if the Q_i^l are known.

Replacing in eqn. (2.53) the spheroidal kernel by eqn. (2.38) we get

$$Q_i^l = \int_{\psi=\psi_0}^{\pi} S(\psi) P_i(\cos\psi) \sin\psi \, d\psi - \sum_{k=2}^{l} \frac{2k+1}{k-1} e_{ik}(\psi_0) \, . \tag{2.56}$$

The integral on the right-hand side is known to be the 'Molodenskij truncation coefficient' [Molodenskij et al., 1962]

$$Q_i(\psi_0) = \int_{\psi=\psi_0}^{\pi} S(\psi) P_i(\cos\psi) \sin\psi \, d\psi \, . \tag{2.57}$$

Efficient algorithms exist to compute the truncation coefficients Q_n (e.g., Paul [1973]). Once these are computed, the Q_n^l are evaluated from

$$Q_n^l(\psi_0) = Q_n(\psi_0) - \sum_{k=2}^{l} \frac{2k+1}{k-1} e_{nk}(\psi_0) . \tag{2.58}$$

Equations (2.55) and (2.58) completely determine the coefficients t_k in terms of $Q_n(\psi_0)$ and $e_{nk}(\psi_0)$. Once determined, they are used to modify the spheroidal Stokes kernel $S_l(\psi)$ according to eqns. (2.45) and (2.46).

Since the modified spheroidal Stokes function contains low degree constituents, the corresponding low degree constituents of Δg **must** be subtracted from the observed gravity anomalies. Figure 2.4 shows the spheroidal Stokes function S_{20} and the modified version for $\psi_0 = 6°$.

2.2.3 Numerical Evaluation

This section describes the numerical evaluation of the spheroidal Stokes integration using the modified Stokes kernel S_l^m. Since the low degree reference spheroid is obtained from GEM9, the subscript l is always 20.

The spherical cap $\psi \leq \psi_0$ is approximated by one degree squares of ellipsoidal coordinates ϕ, λ according to Figure 2.5. The complete integration area, delineated by bold lines in Figure 2.5, is divided into three zones.

- The **innermost zone** covers the immediate neighbourhood of the point of geoid evaluation and its latitude/longitude extension is 10'/10' (10'/20' for high latitudes). Its boundaries coincide with the grid division of the 5' by 5' gravity anomaly file (see section 2.2.7); i.e., the innermost zone may not be exactly centred at the point of geoid evaluation.
- The **inner zone** extends over an area of 2° by 2° minus the innermost zone. Its outer boundaries coincide with 1° coordinate lines; i.e., the inner zone may not be exactly centred at the point of geoid evaluation.

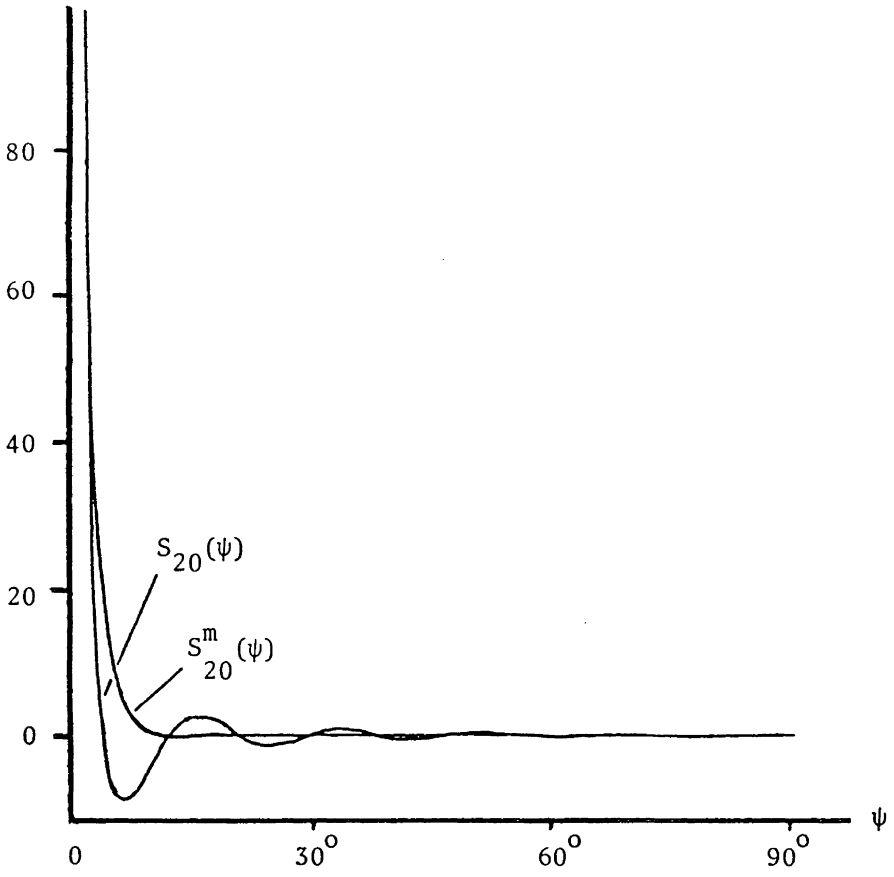

Figure 2.4: Modified and non modified spheroidal Stokes function

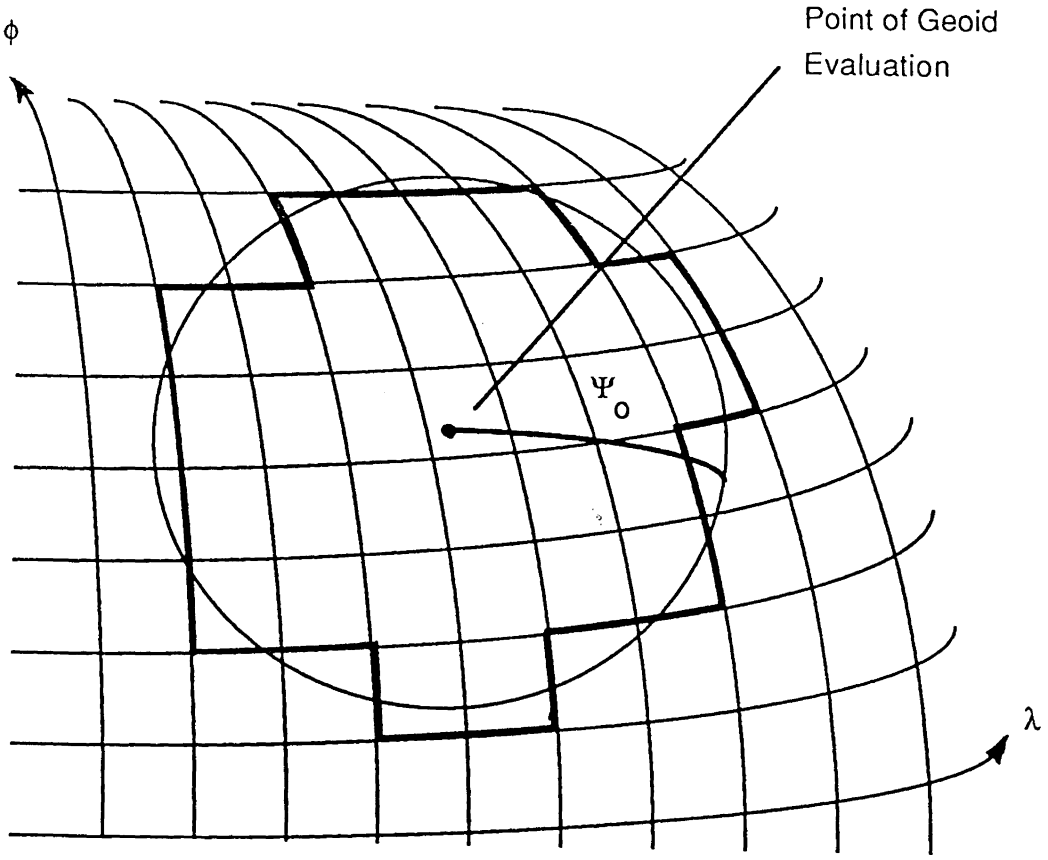

Figure 2.5: Approximation of spherical cap

- The **outer zone** is the area between the outer boundary of the inner zone and the boundary of the integration area.

The subdivision into these three zones is introduced to allow for different integration techniques and different data input Δg^l (see section 2.2.7) in the integration. The selection of these particular boundaries came from numerical tests we have conducted (see section 2.2.8).

2.2.3.1 The innermost zone integration.

Formally, the innermost zone integration can be written as

$$I_{\mathrm{IM}} = \frac{R}{4\pi\gamma} \iint_{\Sigma_{\mathrm{IM}}} S_l^{\mathrm{m}} \cdot \Delta g^l \, d\nu \,, \tag{2.59}$$

where Σ_{IM} is the area of the innermost zone. Parameterized in ellipsoidal coordinates ϕ, λ this reads

$$I_{\mathrm{IM}} = \frac{R}{4\pi\gamma} \int_{\lambda_2}^{\lambda_1} \int_{\phi_1}^{\phi_2} S_l^{\mathrm{m}}(\psi) \, \Delta g^l(\phi, \lambda) \cos\phi \, d\phi \, d\lambda \,. \tag{2.60}$$

Denoting the point of geoid evaluation by ϕ_0, λ_0, we approximate $\cos\phi$ by $\cos\phi_0$ and transform eqn. (2.60) onto a plane by the following mapping:

$$x = \cos\phi_0 \, (\lambda - \lambda_0) \,,$$
$$y = \phi - \phi_0 \,. \tag{2.61}$$

Accordingly, the integration boundaries become

$$x_1 = \cos\phi_0(\lambda_1 - \lambda_0), \; y_1 = \phi_1 - \phi_0$$
$$x_2 = \cos\phi(\lambda_2 - \lambda_0), \; y_2 = \phi_2 - \phi_0 \,, \tag{2.62}$$

and we can rewrite eqn. (2.60) as

$$I_{\mathrm{IM}} = \frac{R}{4\pi\gamma} \int_{x_1}^{x_2} \int_{y_1}^{y_2} S_l^{\mathrm{m}}(\psi) \, \Delta g^l(x, y) \, dx \, dy \,, \tag{2.63}$$

with

$$\psi = \psi(x, y) = \sqrt{(x^2 + y^2)} \, . \tag{2.64}$$

To obtain optimal integration accuracy, we evaluate eqn. (2.63) analytically. To perform this analytical integration we approximate both S_l^{m} and Δg^l by simple analytical functions.

From section 2.2.2 we have

$$S_l^{\mathrm{m}}(\psi) = S(\psi) - \sum_{\mathrm{i}=2}^{l} \frac{2i+1}{i-1} P_{\mathrm{i}}(\cos\psi) - \sum_{\mathrm{i}=2}^{l} \frac{2i+1}{2} t_{\mathrm{i}}(\psi_0) P_{\mathrm{i}}(\cos\psi)$$

$$= S(\psi) - S_l'(\psi, \psi_0) \, . \tag{2.65}$$

The closed form of the Stokes function $S(\psi)$ (e.g., Vaníček and Krakiwsky [1982]) reads:

$$S(\psi) = \operatorname{cosec}\frac{\psi}{2} - 6\sin\frac{\psi}{2} + 1 - 5\cos\psi - 3\cos\psi \ln(\sin\frac{\psi}{2} + \sin^2\frac{\psi}{2}) \tag{2.66}$$

and can be approximated by expanding the trigonometric functions into series:

$$S(\psi) \doteq \frac{2}{\psi} - 3\ln(\frac{\psi}{2}) - \frac{35}{12}\psi - 4 + \theta(\psi^2) \, . \tag{2.67}$$

For $\psi \leq 20'$, the approximation

$$S(\psi) \doteq \frac{2}{\psi} - 3\ln(\frac{\psi}{2}) - 4 \tag{2.68}$$

is better than 0.01%.

For the approximation of the second term in eqn. (2.65), we write

$$S_l'(\psi, \psi_0) = S_l'(\mathrm{o}, \psi_0) + \left.\frac{\partial S_l'}{\partial \psi}\right|_{\psi=0} \cdot \psi + \theta(\psi^2) \, . \tag{2.69}$$

Replacing $S'(\psi, \psi_0)$ on the right-hand side by eqn. (2.65) and noting

$$\frac{\partial}{\partial\psi} P_{\mathrm{i}}(\cos\psi)\,|_{\psi=0} = 0, \; P_{\mathrm{i}}(\cos\psi)\,|_{\psi=0} = 1 \, , \tag{2.70}$$

we obtain

$$S_l'(\psi, \psi_0) = \sum_{i=2}^{l} \frac{2i+1}{i-1} + \sum_{i=0}^{l} \frac{2i+1}{2} t_i \,. \tag{2.71}$$

Combining the results of eqns. (2.68) and (2.71), we get the approximation of the modified spheroidal Stokes function for the innermost zone integration

$$S_l^m(\psi, \psi_0) = \frac{2}{\psi} - 3\, ln(\frac{\psi}{2}) + C(\psi_0) \tag{2.72}$$

with

$$C(\psi_0) = -4 - \sum_{i=2}^{l} \frac{2i+1}{i-1} - \sum_{i=0}^{l} \frac{2i+1}{2} t_i(\psi_0) \,. \tag{2.73}$$

The dominating term in eqn. (2.72) is $2/\psi$. The other terms remain one order of magnitude smaller for $\psi < 20'$.

The gravity anomaly in the innermost zone is assumed to be representable by a second-order algebraic polynomial in x and y according to

$$\Delta g^l(x, y) = \alpha_0 + \alpha_1 x + \alpha_2 y + \alpha_3 xy + \alpha_4 x^2 + \alpha_5 y^2 \,. \tag{2.74}$$

It is expected that the dominant term in eqn. (2.74) is the constant α_0. As many α coefficients are determined as the geometry of the gravitational distribution of point gravity anomalies in the innermost zone allows.

Inserting eqns. (2.72) and (2.74) into eqn. (2.63), we obtain (neglecting the products of non-dominating terms):

$$I_{IM} = \sum_{i=1}^{8} I_i \,, \tag{2.75}$$

with

$$I_1 = \frac{R}{4\pi\gamma} 2\alpha_0 \int_{x_1}^{x_2} \int_{y_1}^{y_2} \frac{dx\, dy}{\sqrt{(x^2 + y^2)}} \tag{2.76}$$

$$I_2 = \frac{R}{4\pi\gamma} 2\alpha_1 \int_{x_1}^{x_2} \int_{y_1}^{y_2} \frac{x}{\sqrt{(x^2 + y^2)}}\, dx\, dy \tag{2.77}$$

$$I_3 = \frac{R}{4\pi\gamma} 2\alpha_2 \int_{x_1}^{x_2} \int_{y_1}^{y_2} \frac{y}{\sqrt{(x^2 + y^2)}}\, dx\, dy \tag{2.78}$$

$$I_4 = \frac{R}{4\pi\gamma}\, 2\alpha_3 \int_{x_1}^{x_2}\int_{y_1}^{y_2} \frac{xy}{\sqrt{(x^2+y^2)}}\, dx\, dy \tag{2.79}$$

$$I_5 = \frac{R}{4\pi\gamma}\, 2\alpha_4 \int_{x_1}^{x_2}\int_{y_1}^{y_2} \frac{x^2}{\sqrt{(x^2+y^2)}}\, dx\, dy \tag{2.80}$$

$$I_6 = \frac{R}{4\pi\gamma}\, 2\alpha_5 \int_{x_1}^{x_2}\int_{y_1}^{y_2} \frac{y^2}{\sqrt{(x^2+y^2)}}\, dx\, dy \tag{2.81}$$

$$I_7 = \frac{R}{4\pi\gamma}\, -3\alpha_0 \int_{x_1}^{x_2}\int_{y_1}^{y_2} ln\, \frac{\sqrt{(x^2+y^2)}}{2}\, dx\, dy \tag{2.82}$$

$$I_8 = \frac{R}{4\pi\gamma} \cdot C \cdot \alpha_0 \int_{x_1}^{x_2}\int_{y_1}^{y_2} dx\, dy\ . \tag{2.83}$$

The results of these integrations are given below.

$$I_1 = \frac{R}{4\pi\gamma}\, 2\alpha_0 \left\{ x_2\, ln \left| \frac{y_2+\sqrt{(y_2^2+x_2^2)}}{y_1+\sqrt{(y_1^2+x_2^2)}} \right| - x_1\, ln \left| \frac{y_2+\sqrt{(y_2^2+x_1^2)}}{y_1+\sqrt{(y_1^2+x_1^2)}} \right| \right.$$

$$\left. + y_2\, ln \left| \frac{x_2+\sqrt{(y_2^2+x_2^2)}}{x_1+\sqrt{(y_2^2+x_1^2)}} \right| - y_1\, ln \left| \frac{x_2+\sqrt{(y_1^2+x_2^2)}}{x_1+\sqrt{(y_1^2+x_1^2)}} \right| \right\} \tag{2.84}$$

$$I_2 = \frac{R}{4\pi\gamma}\alpha_1 \left\{ y_2(\sqrt{(y_2^2+x_2^2)} - \sqrt{(y_2^2+x_1^2)}) - y_1(\sqrt{(y_1^2+x_2^2)} - \sqrt{(y_1^2+x_1^2)}) \right.$$

$$\left. + x_2^2\, ln \left| \frac{y_2+\sqrt{(y_2^2+x_2^2)}}{y_1+\sqrt{(y_1^2+x_2^2)}} \right| - x_1^2\, ln \left| \frac{y_2+\sqrt{(y_2^2+x_1^2)}}{y_1+\sqrt{(y_1^2+x_1^2)}} \right| \right\} \tag{2.85}$$

I_3 : exchange x and y in I_2.

$$I_4 = \frac{R}{4\pi\gamma}\, \frac{2}{3}\, \alpha_3 \left((y_2^2+x_2^2)^{3/2} - (y_1^2+x_2^2)^{3/2} - (y_2^2+x_1^2)^{3/2} + (y_1^2+x_1^2)^{3/2} \right) \tag{2.86}$$

$$I_5 = \frac{R}{4\pi\gamma} 2\alpha_4 \left\{ \frac{1}{6} \left(x_2 y_2 \sqrt{(x_2^2+y_2^2)} - x_2 y_1 \sqrt{(x_2^2+y_1^2)} - x_1 y_2 \sqrt{(x_1^2+y_2^2)} + x_1 y_1 \sqrt{(x_1^2+y_1^2)} \right) \right.$$

$$+ \frac{1}{3} \left(x_2^3 \ln \frac{y_2+\sqrt{(y_2^2+x_2^2)}}{y_1+\sqrt{(y_1^2+x_2^2)}} - x_1^3 \ln \frac{y_2+\sqrt{(y_2^2+x_1^2)}}{y_1+\sqrt{(y_1^2+x_1^2)}} \right) \qquad (2.87)$$

$$\left. - \frac{1}{6} \left(y_2^3 \ln \frac{x_2+\sqrt{(x_2^2+y_2^2)}}{x_1+\sqrt{(x_1^2+y_2^2)}} - y_1^3 \ln \frac{x_2+\sqrt{(x_2^2+y_1^2)}}{x_1+\sqrt{(x_1^2+y_1^2)}} \right) \right\}$$

I_6 : exchange x and y in I_5

$$I_7 = -\frac{R}{4\pi\gamma} \cdot 3\alpha_o \left\{ x_1 y_1 \left[-\frac{3}{2} + \ln \frac{\sqrt{(x_1^2+y_1^2)}}{2} \right] + |x_1 y_2| \left[-\frac{3}{2} + \ln \frac{\sqrt{(x_1^2+y_2^2)}}{2} \right] \right.$$

$$+ |x_2 y_1| \left[-\frac{3}{2} + \ln \frac{\sqrt{(x_2^2+y_1^2)}}{2} \right] + x_2 y_2 \left[-\frac{3}{2} + \ln \frac{\sqrt{(x_2^2+y_2^2)}}{2} \right]$$

$$+ x_1^2 \operatorname{arccot}\left(\frac{x_1}{y_1}\right) + x_1^2 \operatorname{arccot}\left|\frac{x_1}{y_2}\right|$$

$$+ x_2^2 \operatorname{arccot}\left|\frac{x_2}{y_1}\right| + x_2^2 \operatorname{arccot}\left(\frac{x_2}{y_2}\right) \qquad (2.88)$$

$$+ \frac{1}{2}(x_1^2 + y_1^2) \operatorname{arccot}\left(\frac{y_1}{x_1}\right) + \frac{1}{2}(x_1^2+y_2^2) \operatorname{arccot}\left|\frac{y_2}{x_1}\right|$$

$$\left. + \frac{1}{2}(x_2^2+y_1^2) \operatorname{arccot}\left|\frac{y_1}{x_2}\right| + \frac{1}{2}(x_2^2 + y_2^2) \operatorname{arccot}\left(\frac{y_2}{x_2}\right) \right\} ,$$

$$I_8 = \frac{R}{4\pi\gamma} C \alpha_o (x_2 - x_1)(y_2 - y_1) . \qquad (2.89)$$

In the real world, the number of point gravity values in the innermost zone will vary quite widely, from none to several tens. Also, the distribution of these values will vary from quite uniform to linear. The integration algorithm has to be designed to reflect this.

The algorithm implemented in our software first checks on the number and distribution of the existing point values, by evaluating the determinant of the matrix of normal equations. If the determinant is too small, in absolute value, the degree of the surface for the integration (originally equal to 2) is lowered and the test is repeated. If the surface, following this procedure, degenerates to a plane, then the point values are automatically replaced by the four mean 5' by 5' anomalies in the innermost zone. In higher latitudes ($\phi > 54°$), the default solution is a constant plane, computed from the two 5' by 10' mean anomalies in the innermost zone.

2.2.3.2 The inner zone integration.

Formally, the integration in the inner zone can be written as:

$$I_{\mathrm{I}} = \frac{R}{4\pi\gamma} \iint_{\Sigma_{\mathrm{I}}} S_l^{\mathrm{m}} \cdot \Delta g^l \, dv \tag{2.90}$$

where Σ_{I} is the area of the inner zone, consisting of an integer number L of 5 ' by 5' cells.

Replacing the area of the inner zone Σ_{I} by the sum of the 5' by 5' cells, we obtain, from eqn. (2.90),

$$I_{\mathrm{I}} = \frac{R}{4\pi\gamma} \sum_{\mathrm{i=i}}^{\mathrm{L}} \iint_{\Sigma_{\mathrm{i}}} S_l^{\mathrm{m}} \cdot \Delta g^l \, dv, \tag{2.91}$$

where we have denoted the area of the *ith* individual 5' by 5' cell by Σ_{i}.

The data to be used in the inner zone integration are mean gravity anomalies $\bar{\Delta g}_i^l$ assigned to the 5' by 5' blocks, leading to

$$I_I = \frac{R}{4\pi\gamma} \sum_{i=1}^{L} \bar{\Delta g}_i^l \iint_{\Sigma_i} S_l^m \, dv \quad . \tag{2.92}$$

To simplify the integration procedure (2.92) further, we approximate the modified spheroidal Stokes function by its value at the centre of the 5' by 5' cell

$$S_l^m(\psi) = S_l^m(\psi_i) \, , \tag{2.93}$$

with ψ_i being the spherical distance between the point of geoid evaluation and the centre of the 5' by 5' cell.

The final integration procedure now reads

$$I_I = \frac{R}{4\pi\gamma} \sum_{i=1}^{L} S_l^m(\psi_i) \, \bar{\Delta g}_i^l \, \Sigma_i \tag{2.94}$$

with the surface element

$$\forall i : \Sigma_i = \cos\phi_i \cdot a^2 \tag{2.95}$$

and a is the cell size (5') in radians.

2.2.3.3 The outer zone integration.

Formally, the integration in the outer zone can be written as:

$$I_O = \frac{R}{4\pi\gamma} \iint_{\Sigma_O} S_l^m \, \bar{\Delta g}^l \, dv \, , \tag{2.96}$$

where Σ_O is the area of the outer zone, consisting of an integer number M of 1° by 1° cells.

Replacing the kernel $S_l^m(\psi)$ by its value at the centre point of the 1° by 1° cell, we obtain

$$I_o = \frac{R}{4\pi\gamma} \sum_{i=1}^{M} S_l^m(\psi_i)\, \bar{\Delta g}^l\, \Sigma_i \qquad (2.97)$$

with

$$\forall i : \Sigma_i = \cos\phi_i \cdot b^2$$

and b is the cell size (1°) in radians.

2.2.3.4 Approximation of modified kernel

Clearly, the evaluation of $S_{20}^m(\psi)$ for different values of ψ (eqns. (2.45), (2.46)) is a time consuming task. Yet it has to be done at least 650 times for each point of interest. It is, therefore, imperative that a more simple expression be found for its evaluation.

This expression is sought in the following form:

$$S'(\psi) = \alpha_o + \frac{\alpha_1}{\psi} + \alpha_2 \ln\left(\frac{\psi}{2}\right) + \alpha_3\, \psi^2 \ln\left(\frac{\psi}{2}\right), \qquad (2.98)$$

such that the uniform (Tchebyshev) fit of S' to S_{20}^m is as good as possible and the maximum relative error $((S' - S_{20}^m)/S_{20}^m)$ is at most 10^{-3}. Assuming that $|\delta N^{20}|$ is smaller than 10 metres everywhere, this approximation will not introduce errors in absolute value larger than 1 cm.

To the best of our knowledge, there exists no algorithm for evaluating $\alpha_0,\ldots,\alpha_3$ which would make the uniform fit the best. This is because the functions used in eqn. (2.98) are not algebraic. We have thus started by selecting the four Tchebyshev interpolation nodes appropriate for algebraic functions and moved these around empirically to improve the fit. The final expression for $S'(\psi)$, appropriate for $\psi \in \langle 0°, 6°\rangle$, is

$$S'(\psi) = -32.435\,44 + \frac{1.997\,27}{\psi} - 3.449\,27 \ln\left(\frac{\psi}{2}\right) - 173.244\,17\, \psi^2 \ln\left(\frac{\psi}{2}\right). \qquad (2.99)$$

Figure 2.4 shows the difference between S' and S_{20}^m.

The approximate kernel (eqn. (2.99)) was tested on several Δg data sets and gave results which departed from those obtained with S_{20}^{m} always by no more than 1 cm in either direction.

2.2.4 The Atmospheric Attraction Effect

For the solution of the geodetic boundary value problem (eqn. (2.2)), we assumed the disturbing gravity potential T to be harmonic outside the geoid. Since the potential produced by the atmospheric masses is not harmonic outside the geoid, we have to correct the results of the computations in section 2.2 accordingly.

The atmospheric masses produce the atmospheric attraction effect δg_A on gravity. This effect has been investigated by Ecker and Mittermayer [1969] and tables for δg_A have been published by the IAG [1971]. δg_A is a function of the topographical height and varies between +0.87 mGal and +0.54 mGal for heights of 0 km and 4 km, respectively. It has to be added to the observed gravity anomaly Δg [Rapp and Rummel, 1975]. The effect of δg_A on computed geoid undulations is discussed in section 3.2.

The procedure described above is based on the assumption that the atmosphere consists of ellipsoidal layers of constant density. Lateral inhomogeneities introduce an additional second-order effect [Vaníček and Krakiwsky, 1982]. This second-order effect leads to less than 10 cm distortion of the geoid in the Canadian territory and will be neglected in the sequel.

2.2.5 The Topographical Attraction Effect

The reasoning used in the previous section for the influence of the atmospheric masses holds equally for the topographic masses above the geoid: to solve the boundary value problem (eqn. (2.2)) we have to move all topographic masses mathematically below the geoid surface. This dislocation of masses changes the gravitational attraction at the physical surface of the earth. We call this change in gravity the *topographical attraction effect* δg_T. After applying this δg_T to the gravity anomalies, we can solve eqn. (2.2). Since we change (mathematically) the mass distribution, this solution will not coincide exactly with the geoid. The difference between the solution and the geoid is known as the *indirect effect* [Vaníček and Krakiwsky, 1982] and will be dealt with in section 2.2.6.

Since there is no prescribed way on how to move the topographical masses below the geoidal surface, we have infinitely many choices. For the present task, we choose to condense the topographic masses mathematically on the geoid surface. This method is known to produce small indirect effects [Heiskanen and Moritz, 1967].

Both the topographical attraction effect and the indirect effect are rather small and certain simplifications and approximations can be employed in the computational procedures. The computational procedure is illustrated in Figure 2.6. We approximate the geoid locally by a tangential plane. The topographical masses are assigned a constant density ρ. l is the horizontal distance between the point P_A where δg_T is to be computed and the point P_Q where masses are condensed onto the geoid. The topographical heights at P_A and P_Q are denoted by H_A and H_Q, respectively.

A mass element dm_1 located somewhere below P_Q at a height $H_A + z$ gives a rise to the gravitational potential

$$dW_1 = \frac{G dm_1}{L_1} \tag{2.100}$$

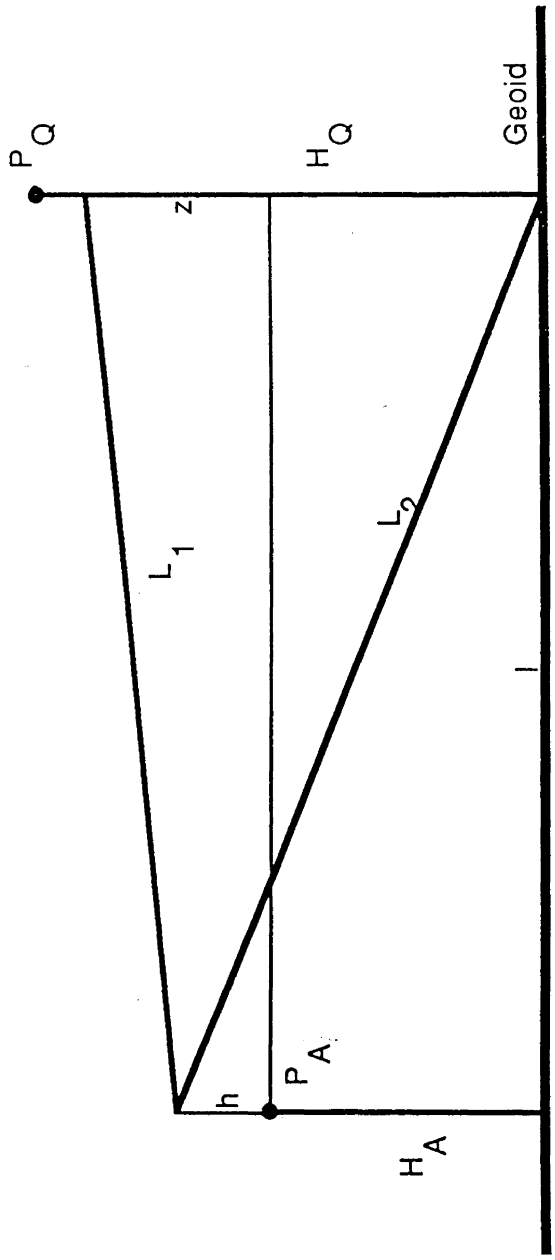

Figure 2.6: Computation of the topographical attraction effect

at height h above P_A. If we move the mass element onto the geoid and denote it by dm_2, we obtain another potential

$$dW_2 = \frac{G dm_2}{L_2}. \tag{2.101}$$

When dm_1 is 'moved onto the geoid, the observer at P_A will experience a change in gravitational acceleration equal to the negative vertical gradient of the difference between dW_1 and dW_2

$$d\delta g_T = - \partial/\partial h|_{h=0} (dW_2 - dW_1) . \tag{2.102}$$

The total change in gravitational attraction is obtained by integrating over all possible mass elements dm_1. In a local coordinate system, α = azimuth, l = distance, y = height, centred at the geoid below P_A, with the mass element being

$$dm = \rho\, l\, d\alpha\, dl\, dy \tag{2.103}$$

we obtain for the gravitational potentials W_1 and W_2

$$W_1 = G\rho \int_{\alpha=0}^{2\pi} \int_{l=0}^{\infty} \int_{y=0}^{H_Q} \frac{l}{L_1}\, dy\, dl\, d\alpha \tag{2.104}$$

$$W_2 = G\rho \int_{\alpha=0}^{2\pi} \int_{l=0}^{\infty} \frac{l}{L_2}\, H_Q\, dl\, d\alpha . \tag{2.105}$$

Before evaluating integrals (2.104) and (2.105) we note that a plate of constant thickness H_A, density ρ, and infinite extension gives at P_A a gravitational attraction identical to the attraction created by the same masses condensed at the lower surface of the plate. Thus we can in our approximate solution neglect this plate and obtain, from eqns. (2.104) and (2.105),

$$W_1 = G\rho \int_{\alpha=0}^{2\pi} \int_{l=0}^{\infty} \int_{y=H_A}^{H_Q} \frac{l}{L_1} dy\, dl\, d\alpha \tag{2.106}$$

$$W_2 = G\rho \int_{\alpha=0}^{2\pi} \int_{l=0}^{\infty} \frac{l}{L_2} (H_Q - H_A)\, dl\, d\alpha\,. \tag{2.107}$$

The resulting topographical attraction effect can then be written

$$\delta g_T = - \partial/\partial h|_{h=0} (W_2 - W_1)$$

$$= - \partial/\partial h|_{h=0} G\rho \int_{\alpha=0}^{2\pi} \int_{l=0}^{\infty} \left\{ \frac{H_Q - H_A}{L_2} - \int_{y=H_A}^{H_Q} \frac{dy}{L_1} \right\} l\, dl\, d\alpha\,. \tag{2.108}$$

To evaluate the subintegral functions, we express the distances L_1 and L_2 in the chosen coordinate system. From Figure 2.6 we obtain

$$L_1^2 = l^2 + (z - h)^2 = l^2 + (y - H_A - h)^2$$
$$L_2^2 = l^2 + (H_A + h)^2\,. \tag{2.109}$$

Correct to quadratic terms in H_A/l, h/l, y/l, we get from eqn. (2.109)

$$\frac{1}{L_1} = \frac{1}{l} \left\{ 1 - \frac{(y - H_A - h)^2}{2l^2} \right\}$$

$$\frac{1}{L_2} = \frac{1}{l} \left\{ 1 - \frac{(H_A + h)^2}{2l^2} \right\} \tag{2.110}$$

and

$$\int_{y=H_A}^{H_Q} \frac{1}{L_1}\, dy = (H_Q - H_A) \frac{1}{l} \left(1 - \frac{(H_A + h)^2}{2l^2} \right)$$

$$+ \frac{1}{6l^3} [3(H_A + h)(H_Q^2 - H_A^2) - (H_Q^3 - H_A^3)]\,. \tag{2.111}$$

Equations (2.110) and (2.111) give, for the subintegral function in eqn. (2.108),

$$\frac{H_Q - H_A}{L_2} - \int_{y=H_A}^{H_Q} \frac{dy}{L_1} = - \frac{1}{6l^3} [3(H_A + h)(H_Q^2 - H_A^2) - (H_Q^3 - H_A^3)] \tag{2.112}$$

and performing the differentiation with respect to h we obtain, from eqn. (2.108),

$$\delta g_T = \frac{G\rho}{2} \int_{\alpha=0}^{2\pi} \int_{l=0}^{\infty} \frac{H_Q^2 - H_A^2}{l^3} \, l \, dl \, d\alpha \, . \tag{2.113}$$

For practical computations, eqn. (2.113) has to be discretized. The topographical height data available for the computation of the topographical attraction effect are 5' by 5' mean topographical heights (see section 2.2.7). Denoting by $\bar{l}_i$ the mean distance of the i*th* 5' by 5' cell from the point of interest and by $\bar{H}_i$ the corresponding mean topographical height, we obtain from eqn. (2.113)

$$\delta g_T = \frac{G\rho R^2}{2} \sum_i \frac{\bar{H}_i^2 - H_A^2}{\bar{l}_i^3} \Sigma_i \tag{2.114}$$

with Σ_i given by eqn. (2.95) and the summation extended over all 5' by 5' cells with significant contributions. Due to the fast decreasing integral kernel l^{-3}, only the immediate neighbourhood of the point of interest has to be considered in the computation of δg_T. δg_T has to be added to the original free air gravity anomalies.

2.2.6 The Indirect Effect

The indirect effect δN_I of the geoid undulations can be computed (e.g., Heiskanen and Moritz [1967])

$$\delta N_I = \frac{W_I}{\gamma} \tag{2.115}$$

where W_I is the gravitational potential difference due to the mathematical condensation of the topographical masses onto the geoid. W_I is to be evaluated at the geoid. The computational procedure is illustrated on Figure 2.7.

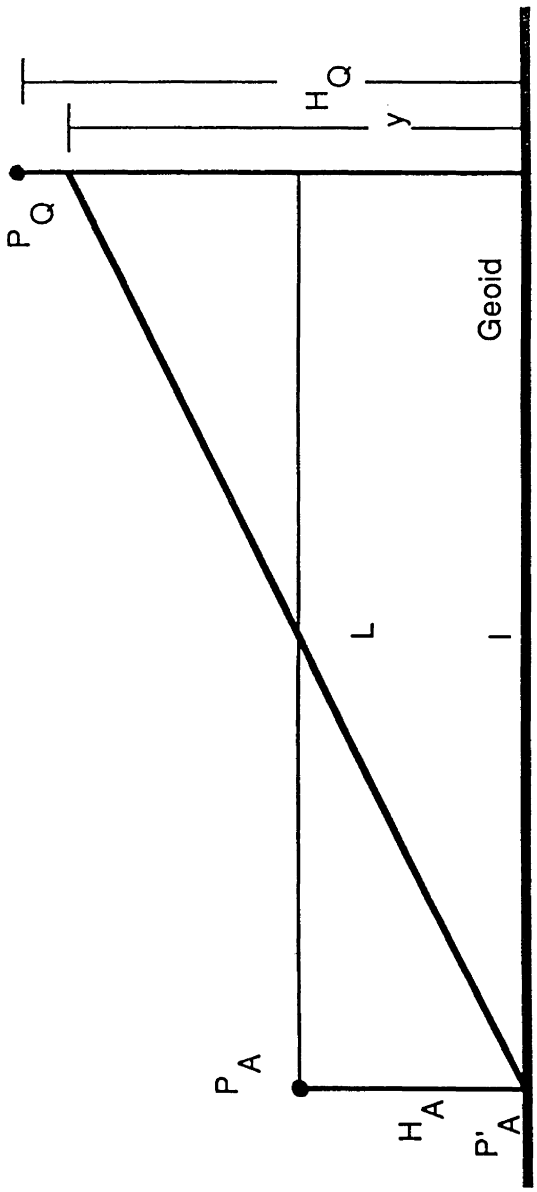

Figure 2.7: Computation of the indirect effect

A column of matter below P_Q gives at P_A', the projection of P_A onto the geoid, a gravitational potential (cf. eqn. (2.104))

$$W_1' = G\rho \int_{\alpha=0}^{2\pi} \int_{l=0}^{\infty} \int_{y=0}^{H_Q} \frac{1}{L}\, l\, dl\, d\alpha\, dy\,. \tag{2.116}$$

The potential of the same matter condensed on the geoid reads (cf. eqn. (2.105))

$$W_2' = G\rho \int_{\alpha=0}^{2\pi} \int_{l=0}^{\infty} H_Q\, dl\, d\alpha\,. \tag{2.117}$$

We evaluate the potential $W_I = W_1' - W_2'$ separately for a plate of uniform thickness H_A and the deviations of the topography from this plate.

Denoting the former by w_1 and the latter by w_2, we obtain from eqns. (2.116) and (2.117)

$$w_1 = G\rho \int_{\alpha=0}^{2\pi} \int_{l=0}^{\infty} \left\{ \int_{y=0}^{H_A} \frac{l}{\sqrt{(l^2+y^2)}}\, dy - H_A \right\} dl\, d\alpha \tag{2.118}$$

and

$$w_2 = G\rho \int_{\alpha=0}^{2\pi} \int_{l=0}^{\infty} \left\{ \int_{y=H_A}^{H_Q} \frac{l}{\sqrt{(l^2+y^2)}}\, dy - (H_Q - H_A) \right\} dl\, d\alpha\,. \tag{2.119}$$

Performing the integration with respect to α and l first, we get, from eqn. (2.118),

$$w_1 = 2\pi G\rho \lim_{q\to\infty} \left\{ \int_{y=0}^{H_A} [\sqrt{(q^2+y^2)} - y]\, dy - q\, H_A \right\}$$

and the integration with respect to y gives

$$w_1 = 2\pi G\rho \lim_{q\to\infty} \left\{ -\frac{H_A^2}{2} + \frac{1}{2}\left[H_A\sqrt{(q^2+H_A^2)} + q^2 \ln \frac{H_A+\sqrt{(q^2+H_A^2)}}{q} \right] - q\, H_A \right\}.$$

Developing the square root and the logarithmic function in power series and performing the limiting operation, we abtain

$$w_1 \doteq - \pi G\rho H_A^2 . \tag{2.120}$$

The second potential term (2.119) due to the deviations of the actual topography from the plate is evaluated by integrating with respect to y

$$w_2 = G\rho \int_{\alpha=0}^{2\pi} \int_{l=0}^{\infty} \left\{ l \ln \frac{H_Q + \sqrt{(H_Q^2+l^2)}}{H_A + \sqrt{(H_A^2+l^2)}} - (H_Q - H_A) \right\} dl \, d\alpha .$$

Power series expansions of the square roots and the logarithmic functions lead finally to

$$w_2 = - \frac{G\rho}{6} \int_{\alpha=0}^{2\pi} \int_{l=0}^{\infty} \frac{H_Q^3 - H_A^3}{l^3} l \, dl \, d\alpha . \tag{2.121}$$

Combining eqns. (2.120) and (2.121) we obtain the indirect effect in the following form:

$$\delta N_I = - \frac{\pi G\rho}{\gamma} H_A^2 - \frac{G\rho}{6\gamma} \int_{\alpha=0}^{2\pi} \int_{l=0}^{\infty} \frac{H_Q^3 - H_A^3}{l^3} l \, dl \, d\alpha . \tag{2.122}$$

The indirect effect δN_I has to be algebraically added to the geoid undulations determined by Stokes's integration.

For numerical computations, equation (2.122) has to be discretized. Height data is available for 5' by 5' blocks (see section 2.2.7). For this type of data, we obtain

$$\delta N_I = - \frac{\pi G\rho}{\gamma} \bar{H}_A^2 - \frac{G\rho R^2}{6\gamma} \sum_i \frac{\bar{H}_i^2 - \bar{H}_A^2}{\bar{l}_i^2} \Sigma_i \tag{2.123}$$

with $\bar{H}_i$, $\bar{H}_A$, $\bar{l}_i$, and Σ_i as in eqn. (2.114).

The three 'corrections' δg_A, δg_T, and δN_I are evaluated numerically within the modified spheroidal Stokes integration described in sections 2.2.1 and 2.2.2. The integrations for δg_T and δN_I are extended over the inner zone (2° by 2°). All three effects are computed from mean heights of 5' by 5' blocks.

2.2.7 Gravity Data

2.2.7.1 Point gravity data.

These data include point gravity anomalies on land and at sea contained in two files (Figures 2.8 and 2.9) provided by the Division of Gravity, Geothermics and Geodynamics, Earth Physics Branch (EPB); Energy, Mines and Resources Canada (EMR) [Hearty, 1985; 1986]. For our purpose, the two files have been merged.

The region containing 628 019 records extends from 40°N to 80°N and from 218°E to 320°E. For each record there are the following items:

- latitude (in degrees and decimals of degree)
- longitude (east, in degrees and decimals of degree)
- free air gravity anomaly (in mgal to 0.1 mGal)
- standard deviation of the gravity anomaly (in mgal to 0.1 mGal)
- height (in metres to 0.1 m)
- standard deviation of height (in metres to 0.1 m).

The observed gravity values are based on the International Gravity Standardization Net 1971 (IGSN 71), the free air anomaly refers to the reference ellipsoid 1980 (GRS80).

In order to save computation time, the data are divided into 20 sequential access files, each of which covers a 10 degree (latitude) by 20 degree (longitude) area, except the rightmost files (east of $\lambda = 298°$), which are 10 by 22 degrees. Each block has 10 minutes overlap with the right and upper adjacent blocks. Within each block the data are sorted in increasing latitude, with points of equal latitude arranged in order of

Figure 2.8: Point Gravity Data on Land and Sea

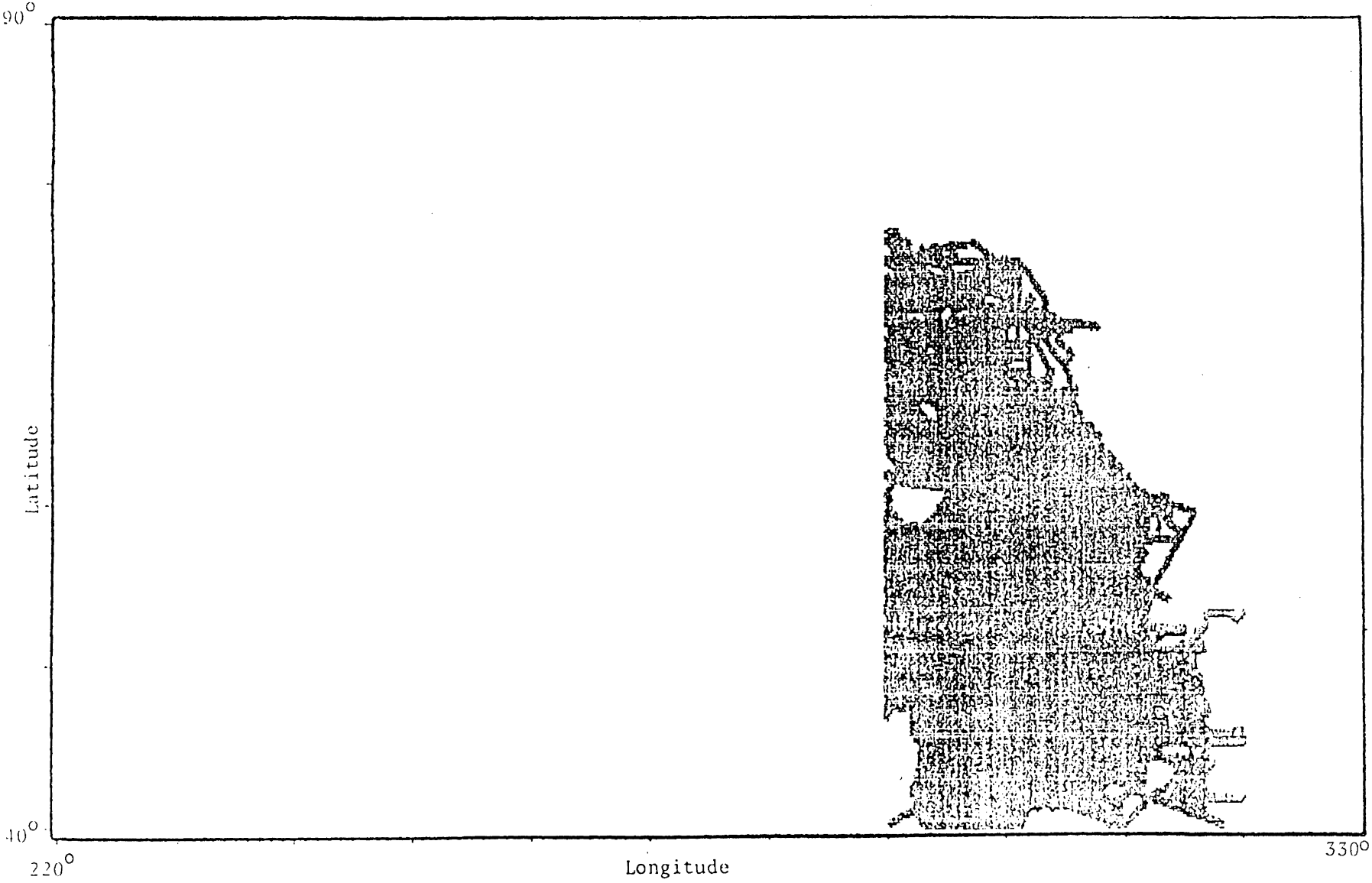

Figure 2.9: New Point Gravity Data Set Containing Additional Sea Gravity

increasing longitude. The arrangement is shown on Figure 2.10. All gravity anomalies have been modified by subtracting the corresponding Goddard's Earth Model 9 (GEM9) low order harmonic gravity anomaly. The original standard deviation of the free air gravity anomaly is kept also for the modified gravity anomaly.

The data have been stored on disk and on magnetic tapes (also supplied to Geodetic Survey of Canada). Upon giving the computation point, the fetching subroutine fetches a 10 minutes by 20 degrees strip of point gravity data needed for the innermost integration.

2.2.7.2 5' by 5' mean gravity anomaly data.

These data originate from EMR [Winter, 1979], and have been updated by us by predicting about 3000 additional means from corresponding point gravity anomalies. The 5' by 5' updated anomalies and heights are obtained by taking the straight arithmetic mean of the point gravity anomaly in the appropriate 5' by 5' square:

$$\overline{\Delta g} = \frac{\sum_{i=1}^{n} \Delta g_i}{n} \tag{2.124}$$

$$\overline{h} = \frac{\sum_{i=1}^{n} h_i}{n} , \tag{2.125}$$

where Δg_i is the i*th* gravity anomaly in the square, and h_i is the i*th* height in the square. If there is no point gravity anomaly data in the 5' by 5' square, then we take the average value from the surrounding 15' by 15' square. The standard deviation values of the updated anomalies are obtained as geometrical averages:

$$\sigma_{\overline{\Delta g}} = \sqrt{\frac{\sum_{i=1}^{n} \sigma^2_{\Delta g_i}}{n}} \tag{2.126}$$

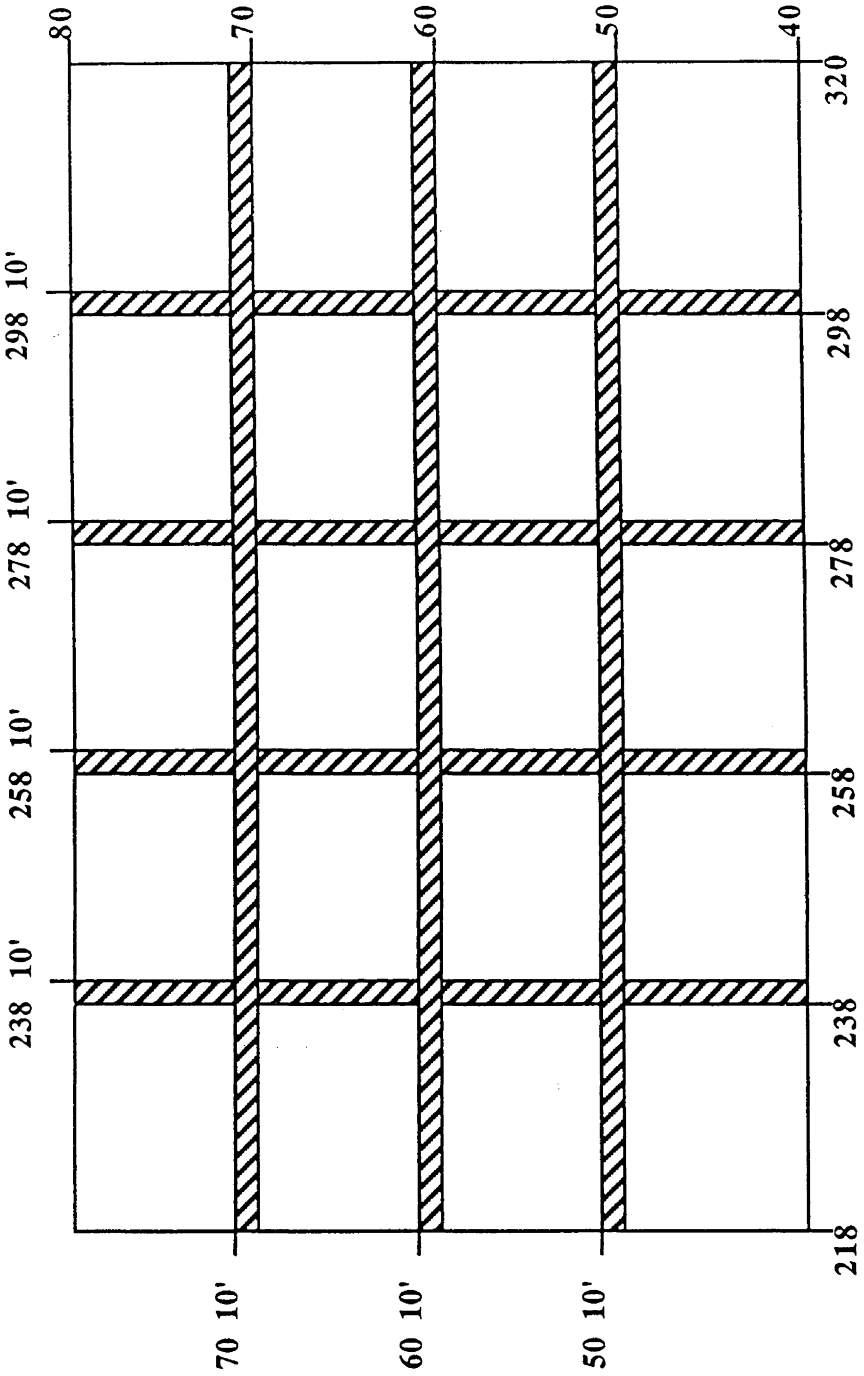

FIGURE 2.10
Arrangement of point gravity data files.

One direct access file has been created. This file is divided (conceptually) into 200, 8° by 8° blocks. Their boundaries are shown in Table 2.1. Each block overlaps with the right and upper adjacent blocks by four degrees. Again the records in each block are sorted in the order of increasing latitude, and increasing longitude for points of equal latitude. Given the computation point, a specific subroutine can obtain the appropriate 8° by 8° block for the integration in the inner zone, and the southwestern corner position of this block. As a result, one can easily figure out the coordinates of each record from its position within the file.

Table 2.1
Boundaries of 5' by 5' gravity anomaly files

Longitude Interval	Latitude Interval
214 - 222	40 - 48
218 - 226	44 - 52
222 - 230	48 - 56
226 - 234	52 - 60
230 - 238	56 - 64
234 - 242	60 - 68
238 - 246	64 - 72
242 - 250	68 - 76
246 - 254	
250 - 258	
254 - 262	
258 - 266	
262 - 270	
266 - 274	
270 - 278	
274 - 282	
278 - 286	
282 - 290	
286 - 294	
290 - 298	
294 - 302	
298 - 306	
302 - 310	
306 - 314	
310 - 318	

The region covered is from 40°N to 76°N, and from 214°E to 318°E (Figure 2.11). From 40°N to 56°N, the 8° by 8° blocks contain 9216, 5' by 5' means each; and from 52°N to 76°N, 4608, 5' by 10' means each. Each record contains three elements:

- free air gravity anomaly (in mgal to 0.1 mGal),
- standard deviation of the free air gravity anomaly (in mgal to 0.1 mGal),
- height (in metres to 0.1 m).

For records containing no original data and where no mean can be generated from the point gravity anomalies, the gravity anomaly and its standard deviation are set to 9999 mGal, and height to 0.0 m. The gravity values refer to the IGSN71, and the free air gravity anomalies refer to the GRS80. Corresponding GEM9 gravity anomalies have been subtracted from the data, and the standard deviation of the modified free air gravity anomaly are the same as that of the original free air gravity anomaly.

2.2.7.3 1 by 1 degree mean gravity anomaly data.

The original 1 by 1 degree mean gravity anomaly data were provided by the Department of Geodetic Science and Surveying of The Ohio State University. These data are termed "The January 1983 1 × 1 Degree Mean Free-Air Anomaly Data" [Rapp, 1983].

In our project, only data from the region of 30°N to 80°N and from 190°E to 340°E are used (Figure 2.12). The original data file contains 7516 records in that region and has 185, 1 by 1 degree cells with no other information but heights. Using eqn. (2.124), 24, 1 by 1 degree mean gravity anomalies have been predicted (Table 2.2) from existing point gravity anomalies. The standard deviations of these predicted gravity anomalies are set to $1/2|\Delta g(\text{Pre}) - \Delta g(\text{GEM9})|$ [Rapp, 1983], and the original heights for the predicted cells remain. Each record has the following items:

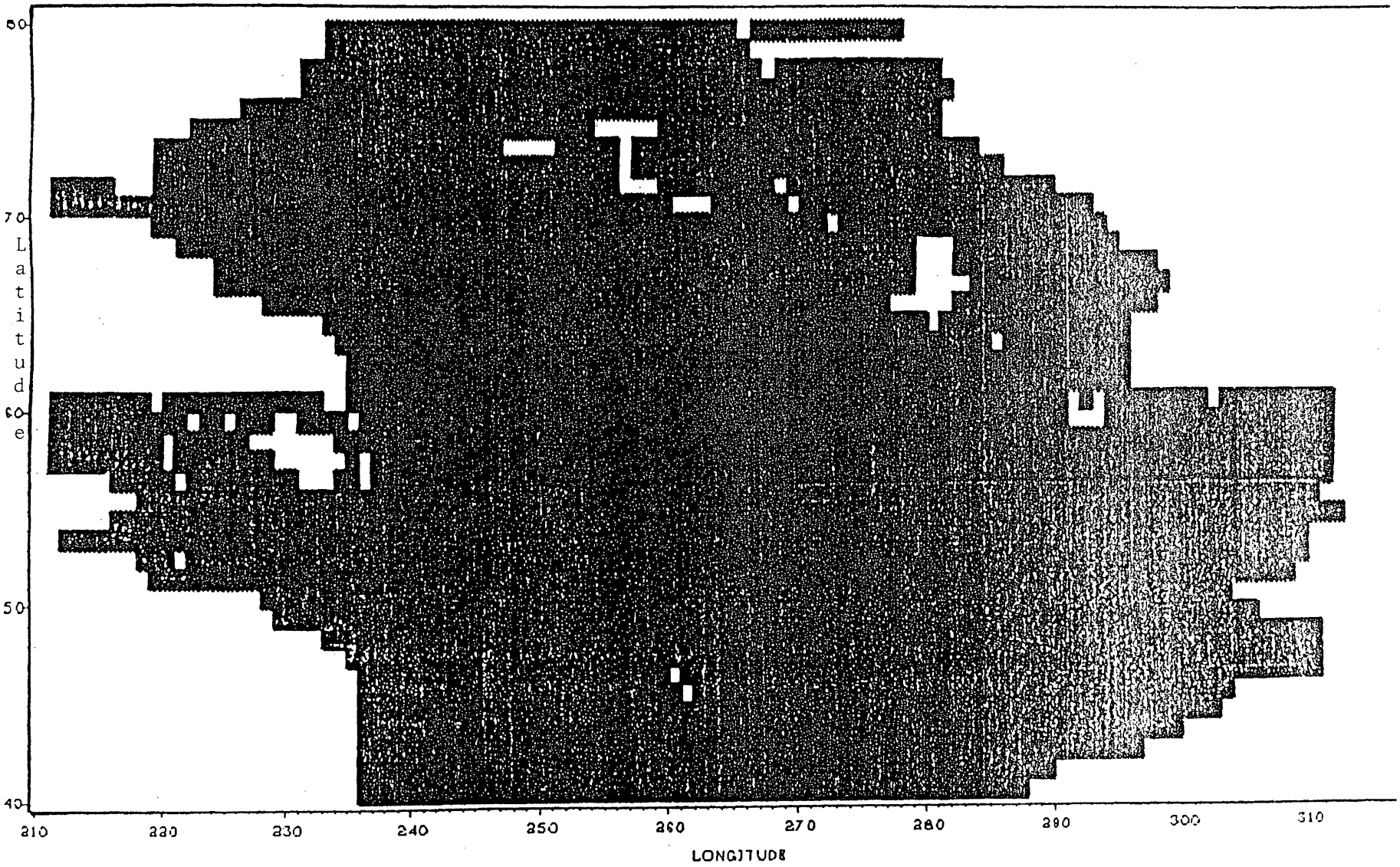

Figure 2.11: 5' x 5' mean gravity anomaly.

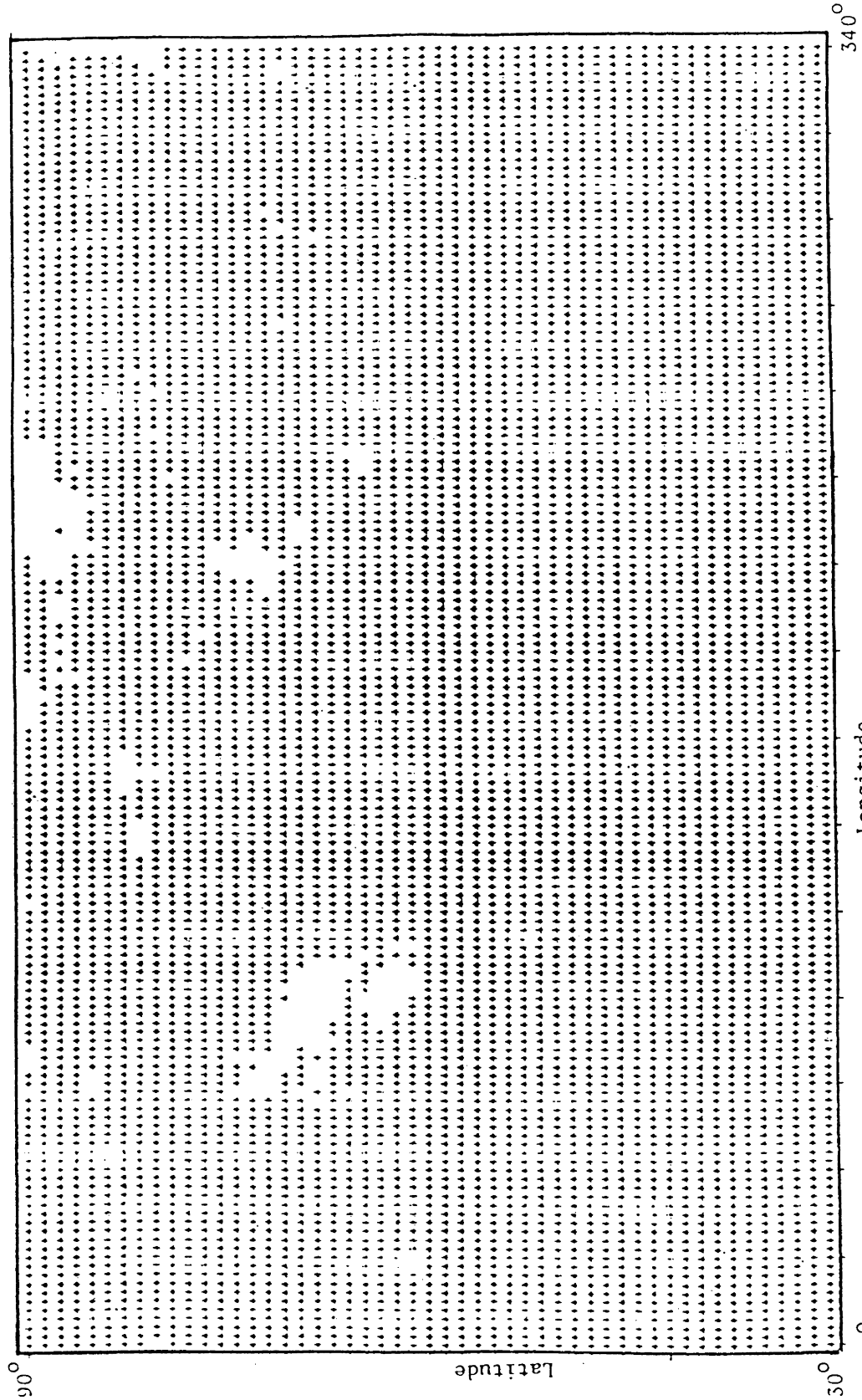

Figure 2.12: The January 1983 1x1 Degree Mean Free-Air Anomaly

TABLE 2.2

24, 1 × 1 degree updated predicting mean gravity anomalies.

Latitude (degree)	Longitude (degree)	$\overline{\Delta g}$ (Terr.) (mgal)	$\overline{\Delta g}$ (GEM9) (mgal)	$\sigma_{\overline{\Delta g}}$ (mgal)	Height (metre)
79	265	-52.2	-1.8	25	143
78	267	-47.8	-4.9	21	104
78	271	-40.9	-3.8	19	189
78	274	-28.6	-2.8	13	319
77	267	-36.3	-8.3	14	-298
74	254	-38.8	-17.9	10	-123
74	255	-34.8	-18.1	8	-210
74	256	-27.3	-18.3	5	-210
74	257	-23.1	-18.5	2	-210
74	258	-20.5	-18.6	1	-109
73	247	-35.1	-16.7	9	-263
73	248	-34.9	-17.3	9	-225
73	249	-38.8	-17.8	10	-235
73	250	-47.4	-18.3	15	-235
73	256	-51.1	-20.6	15	-109
72	256	-58.0	-22.6	18	-47
68	282	-50.8	-18.6	16	-40
67	279	-34.7	-25.3	5	0
65	277	-37.0	-32.7	2	-210
65	281	-30.9	-26.9	2	-53
64	280	-21.4	-30.7	5	-236
63	283	-56.3	-27.6	14	-225
63	284	-53.7	-25.8	14	-260
63	285	-55.1	-23.9	16	-252

- free air gravity anomaly (in mgal to 0.1 mGal)
- standard deviation of the free air anomaly (in mgal to 0.1 mGal)
- height (in metres to the nearest metre).

The free air anomaly is taken with respect to the GRS80. Again, all gravity anomalies have the corresponding GEM9 gravity anomalies subtracted from them.

Blocks with no information available have their gravity anomaly and its standard deviation set to 0.0 mGal and 50 mGal, respectively, and keep the original heights.

2.2.8 Accuracy of the Terrestrial Gravity Contribution

Various sizes and shapes of the individual integration zones have been experimented with. It was found that the shape and extent of the boundaries between inner and outer zones, and between the innermost and inner zones, make very little difference. Fluctuations of the order of at most a few centimetres resulted from even fairly significant shifts of these boundaries.

On the other hand, the selection of the (outer) radius of the outer zone does have an appreciable effect on the computed δN^l even when the integration kernel is appropriately modified (cf. section 2.2) for that particular radius ψ_0. To decide what value of ψ_0 should be selected, we have taken the Rapp 180 by 180 gravity field defined by potential coefficients [Rapp, 1983], subtracted from it the low order (20 by 20) field defined by Rapp's low order coefficients and used this remaining higher order field to generate gravity anomalies on 5' by 5' and 1° by 1° grids. This was done for 18 different areas within three 100° long longitude strips located at latitudes 45, 53, and 71 degrees.

The higher order potential coefficients were then used to compute the higher order contribution δN_{20} to geoidal height (geoidal height above the 20 by 20 reference

spheroid), which could be directly compared with the result of the integration. These comparisons are shown in Table 2.3: listed there are the differences "generated minus integrated," for five different radii of integration.

There does not seem to be any bias introduced by the integration: mean differences are fairly close to zero for all the integration radii. Table 2.3, and even more clearly Figure 2.13, show that the integration discretization accuracy grows with growing integration radius. The levelling off of the RMS curve appears to occur from $\psi_0 = 6^\circ$ and this is the radius we have chosen for our computations.

Table 2.3
Test of numerical integration.

ϕ	λ	ψ_0=3°	ψ_0=4°	ψ_0=5°	ψ_0=6°	ψ_0=7°
45	215	1	2	0	-3	-3
	235	37	19	11	1	-2
	255	4	-4	-4	-5	-5
	275	-26	-15	-3	-3	3
	295	-17	-34	-24	-15	-12
	315	157	108	85	71	67
53	215	-5	-26	-24	-14	-8
	235	24	4	-8	-17	-21
	255	3	6	8	10	5
	275	-82	-62	-48	-33	-26
	295	-36	-31	-10	0	2
	315	32	31	25	11	4
71	215	10	10	11	12	13
	235	-9	-39	-30	-19	-20
	255	34	30	31	18	11
	275	13	9	-9	-13	-8
	295	-40	-27	-11	6	8
	315	-18	17	12	4	4
mean		4.6	-0.6	0.7	0.6	0.7

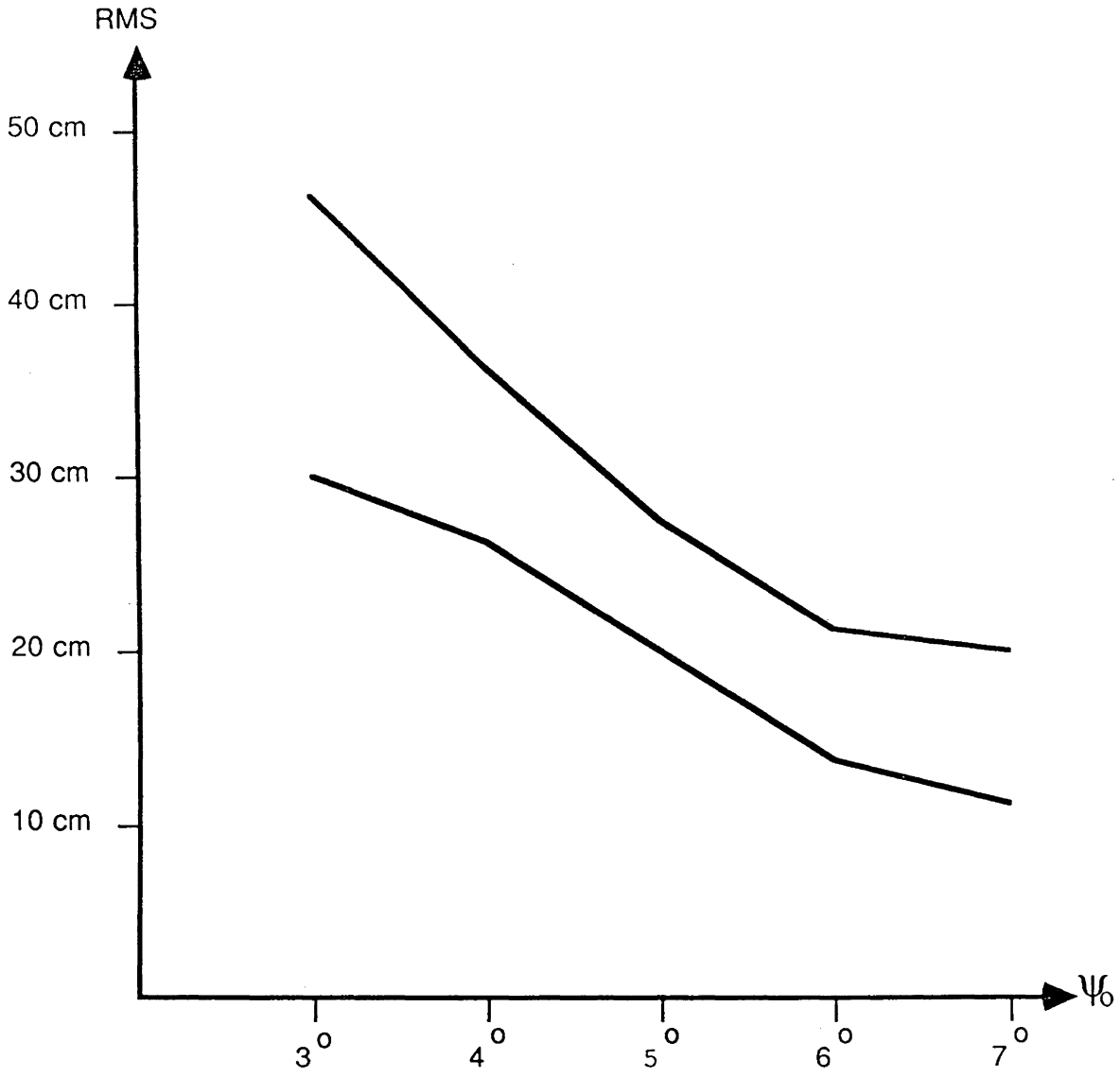

Figure 2.13: Decrease of RMS with growing radius of integration

We note that there are only two localities for which the differences are in absolute value larger than 20 cm for $\psi_0 = 6°$: (45°, 315°) and (53°, 275°). Even the rest of the results do not push the discretization RMS close enough to zero for $\psi_0 = 7°$. We suspect that this is because all the results reflect the fact that the anomalies used are not mean anomalies, as they should be, but point anomalies as obtained from the potential series evaluation. This would be responsible for an effect that is locally systematic but regionally random, i.e., compatible with our results. Indeed, point (45°, 315°) is in the area where the isogravity surface is systematically concave which would explain the large difference. Unfortunately, we do not have enough time to investigate this point further.

It is of interest to observe that if the offensive point (45°, 315°) were excluded from the sample, the RMS for $\psi_0 = 6°$ would drop to 13.5 cm (from 21.3 cm). We can only speculate, without a further investigation, what the real accuracy of the integration discretization is. It is our feeling that the discretization RMS for $\psi_0 = 6°$ should really be closer to 5 cm than 10 cm.

The other contributors to the error in δN_{20} are, of course, errors in the Δg's. This part of the error is evaluated from the law of propagation of errors, assuming the standard deviations contained in the files to be uncorrelated. This assumption results in an overestimation of the magnitude of $\sigma_{\delta N}$ and thus it compensates somewhat for the discretization errors. More will be said about this point in section 3.2.1.

3. TESTING THE GRAVIMETRIC GEOID

3.1 TRANSIT Derived Geoidal Heights (N_D)

3.1.1 Doppler Derived Ellipsoidal Heights (h)

An adjustment of TRANSIT Doppler observations gives primarily station coordinates (x, y, z) and their covariance matrix C_x referred to a geocentric Cartesian coordinate system. The (x, y, z) coordinates and C_x are transformed to GRS80 ellipsoidal coordinates (ϕ, λ, h) and their covariance matrix C_e (e.g., Vaníček and Krakiwsky [1982]).

Since covariance matrices C_x and C_e were not made available to us, some standard deviation for the height coordinate had to be assumed based on experience. All Doppler station positions were computed using 'precise ephemerides' and the translocation technique. The distribution of the Doppler stations is shown in Figure 3.1. Therefore, we expect the accuracy of the ellipsoidal height h (geometrical height, height above reference ellipsoid) to be at the half metre level:

$$\sigma_h = 0.5 \text{ m} \tag{3.1}$$

3.1.2 Orthometric Heights (H)

The geoidal height N_D is obtained from

$$N_D = h - H , \tag{3.2}$$

where the orthometric heights H originate from one of three different sources:

- spirit levelling
- simultaneous reciprocal trigonometric levelling
- inertial survey system measurement.

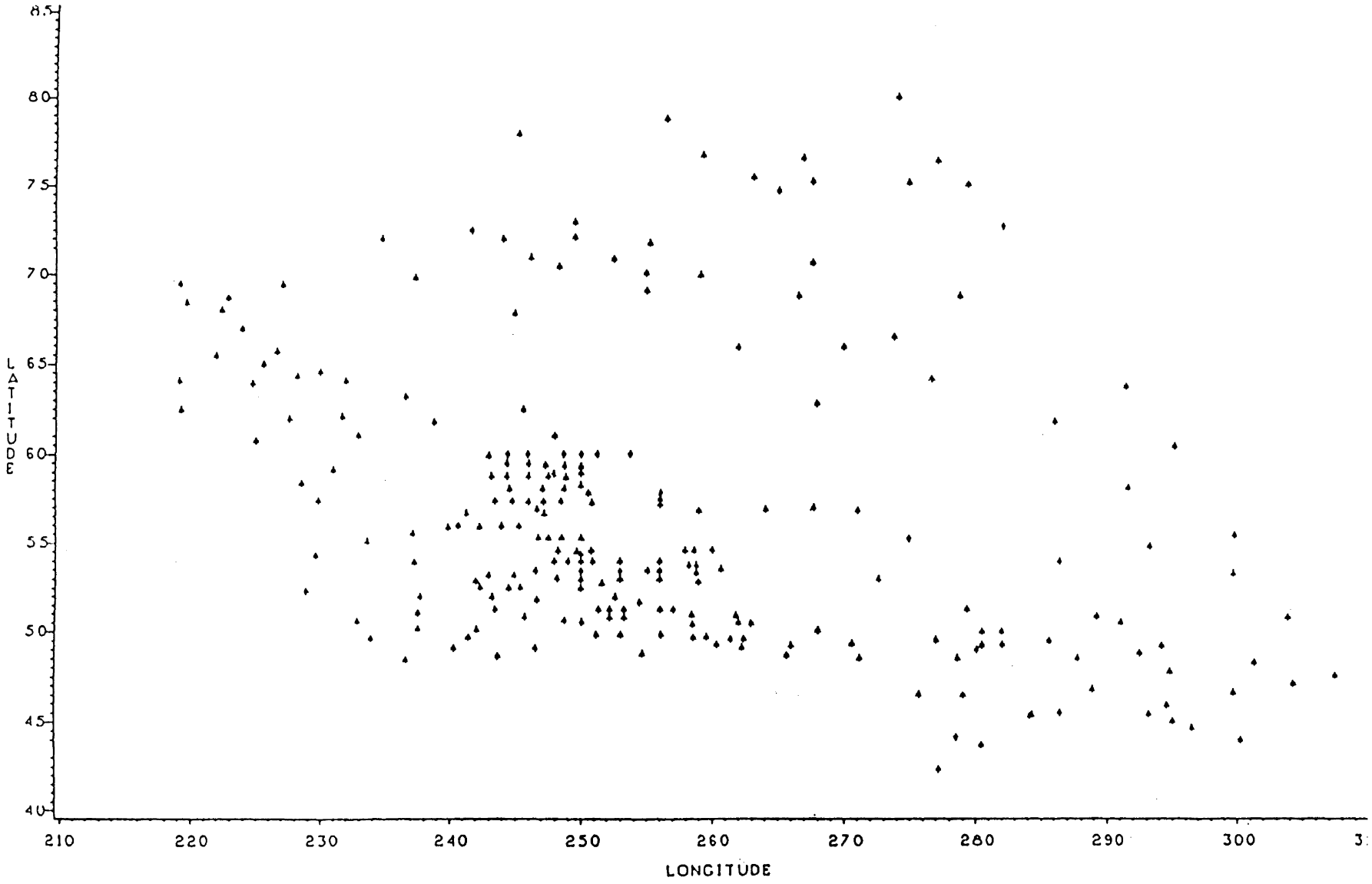

Figure 3.1: Distribution of Available Doppler Points

Spirit levelled heights are believed to be accurate only at the 1.0 m level, mainly because of the neglect of the 'sea surface topography' during the 1928 adjustment of levelling networks [Vaníček and John, 1983]. Since the two other height determination methods listed above have to start from one of the spirit levelled points, their error variance will be the sum of the spirit level error variance and the error variance of the additional measurement. Since numerical values for the accuracy of the methods were not provided, an estimated standard deviation of 1.2 m was assigned the orthometric heights determined by simultaneous reciprocal trigonometric levelling and by inertial survey system measurements.

3.1.3 Accuracy of N_D

For geoid undulations given by eqn. (3.2), the law of error propagation gives

$$\sigma_{N_D} = (\sigma_h^2 + \sigma_H^2)^{1/2} \ . \tag{3.3}$$

Substitution for σ_H and σ_h from sections 3.1.1 and 3.1.2 results in

$$\sigma_{N_D} = 1.1 \text{ m (spirit levelling)}$$

$$\sigma_{N_D} = 1.3 \text{ m (other)} \ . \tag{3.4}$$

These values are then used in all subsequent computations.

3.2 Point Testing Against TRANSIT Derived N

3.2.1 Gravimetric Solution Without Corrections

The gravimetric geoid height N_G was computed for the 212 positions for which the TRANSIT derived geoidal height N_D is known. (Gravimetric solution for the other

points was attempted in vain—there is not sufficient gravity coverage there to obtain a solution.) The distribution of these points is shown in Figure 3.2. In the first run, no correction to the gravimetric solution was applied.

The differences N_D - N_G have then been analysed statistically, regarding the 212 values as a statistical sample. Table 3.1 summarizes the analysis, with the differences being treated as having equal weight. The last column lists the expected values, zero mean, and an average standard deviation evaluated from the three component standard deviations. The average $\sigma_{\delta N}$ turns out to be 16.7 cm.

TABLE 3.1
Statistics of N_D - N_G (without corrections), in centimetres.

	Estimated	Expected
Mean μ	86	0
with respect to 0	183	213
RMS		
with respect to μ	162	213

We see that there is a significant constant bias in the differences. The 'Doppler' geoidal heights are systematically larger by 86 cm. This bias reflects the real difference between the two systems.

Further, we observe that the actual RMS is smaller than expected from the component standard deviations. This shows that the component standard deviations have been overestimated: they should, in fact, be smaller than expected by some 24%. An average σ_{ND} of 91 cm and an average σ_N = 1.33 m of the GEM9 contribution would explain the observed differences.

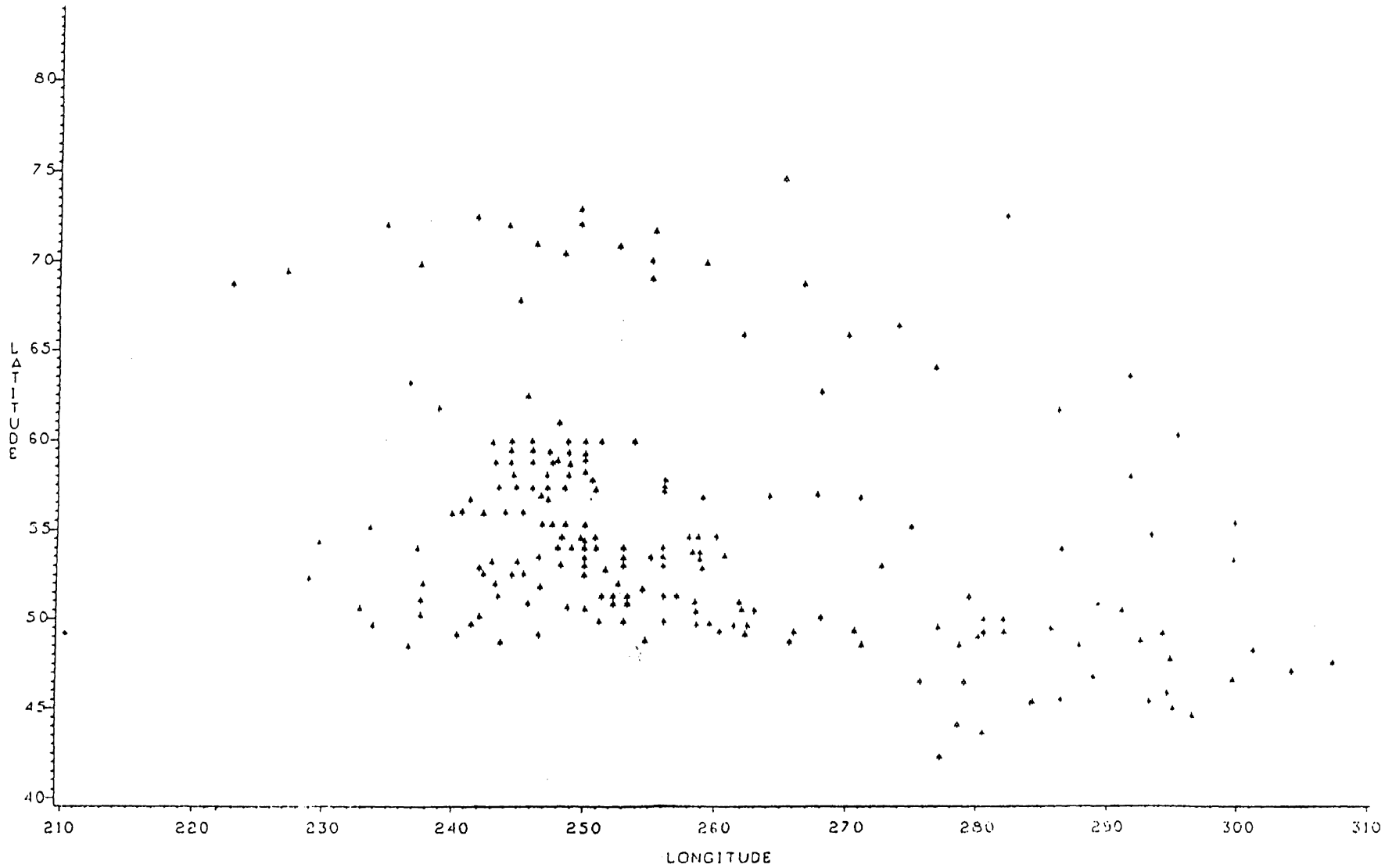

Figure 3.2: Location of Those Doppler Points for which N_G is Available

What is very important, of course, is to see if these differences are distributed systematically in the geographical sense. To study this, however, we have decided to first apply the three corrections: for the atmospheric attraction (see section 2.2.4), for the topographic effect (see section 2.2.5), and for the indirect effect (see section 2.2.6).

3.2.2 Gravimetric Solution with all the Corrections

Table 3.2 summarizes the statistical behaviour of this new sample. Although the corrections amount to several decimetres, the sample of N_D - N_G differences looks much the same as that of the differences when no corrections were applied. The only significant difference is that the mean is now closer to the expected value of 0 by 7 cm, i.e., by about 9%, and the RMS values have been reduced by some 7%.

TABLE 3.2
Statistics of N_D - N_G (with corrections), in centimetres.

	Estimated	Expected
Mean μ	79	0
with respect to 0	171	213
RMS		
with respect to μ	151	213

The differences have been plotted against latitude (Figure 3.3) and longitude (Figure 3.4). Visually, there is no discernible trend in the latitude plot, suggesting that there is no latitude dependence in either of the two solutions. On the other hand, there

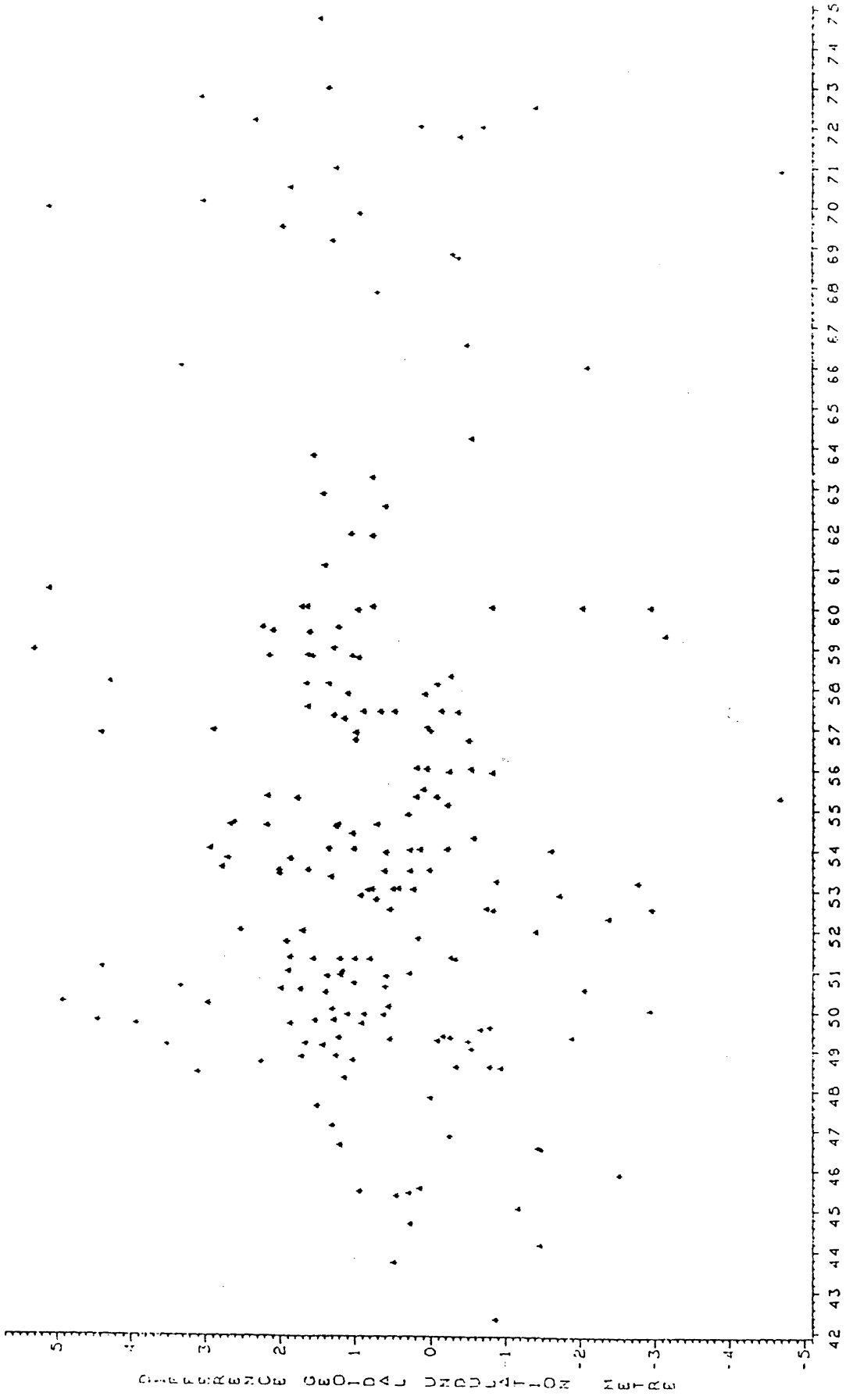

Figure 3.3: Plot of $N_D - N_G$ Against Latitude

Figure 3.4: Plot of N_D-N_G Against Longitude

is a visible longitude dependent effect (Figure 3.4) which may easily reflect the inaccuracy of GEM9.

We have also plotted the absolute values of the differences against heights of the Doppler points (Figure 3.5). Once more, there is no visible dependence of the differences on heights which would seem to rule out the inaccuracy of the gravimetric solution in mountainous regions as the main cause of the differences.

Judging from the last three plots, it appears that the differences are fairly randomly distributed. Figure 3.6, which shows the histogram of the differences N_D - N_G, seems to support this conclusion.

To trace the probable origin of the N_D - N_G differences, we have plotted them once more on a (ϕ, λ) plane using different symbols for different values (Figure 3.7). No regional trends are discernible, and we have to conclude again that the differences are distributed randomly and that the GEM9 reference spheroid and the Doppler derived geoidal heights are both to be blamed about equally.

The last investigation we have undertaken is based on regional difference averages in squares of sides $\Delta\phi = 7^\circ$ and $\Delta\lambda = 14^\circ$. These were plotted and contoured (Figure 3.8) in the hope of showing some systematic variations. There clearly are some small variations present, but it is questionable if these are statistically significant. In any case, they do not look very convincing.

All in all, it seems to us that the Doppler derived N_G do not make an accurate enough external standard to test the gravimetric solution against. Doppler derived N_D's should be treated 'on a par' with the other sources of data. The situation will change when GPS derived N become available.

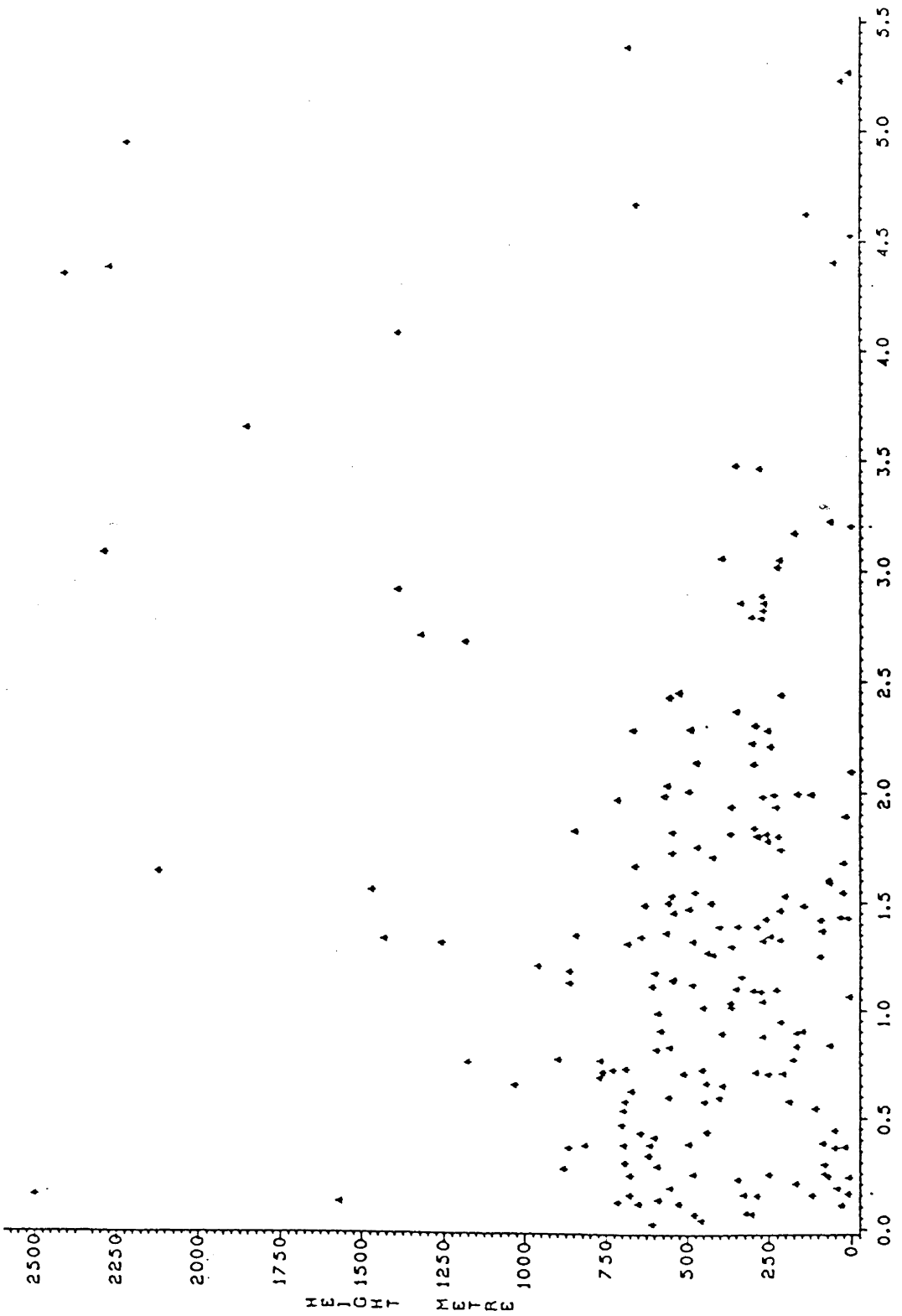

Figure 3.5: Plot of $|N_D - N_G|$ Against Height

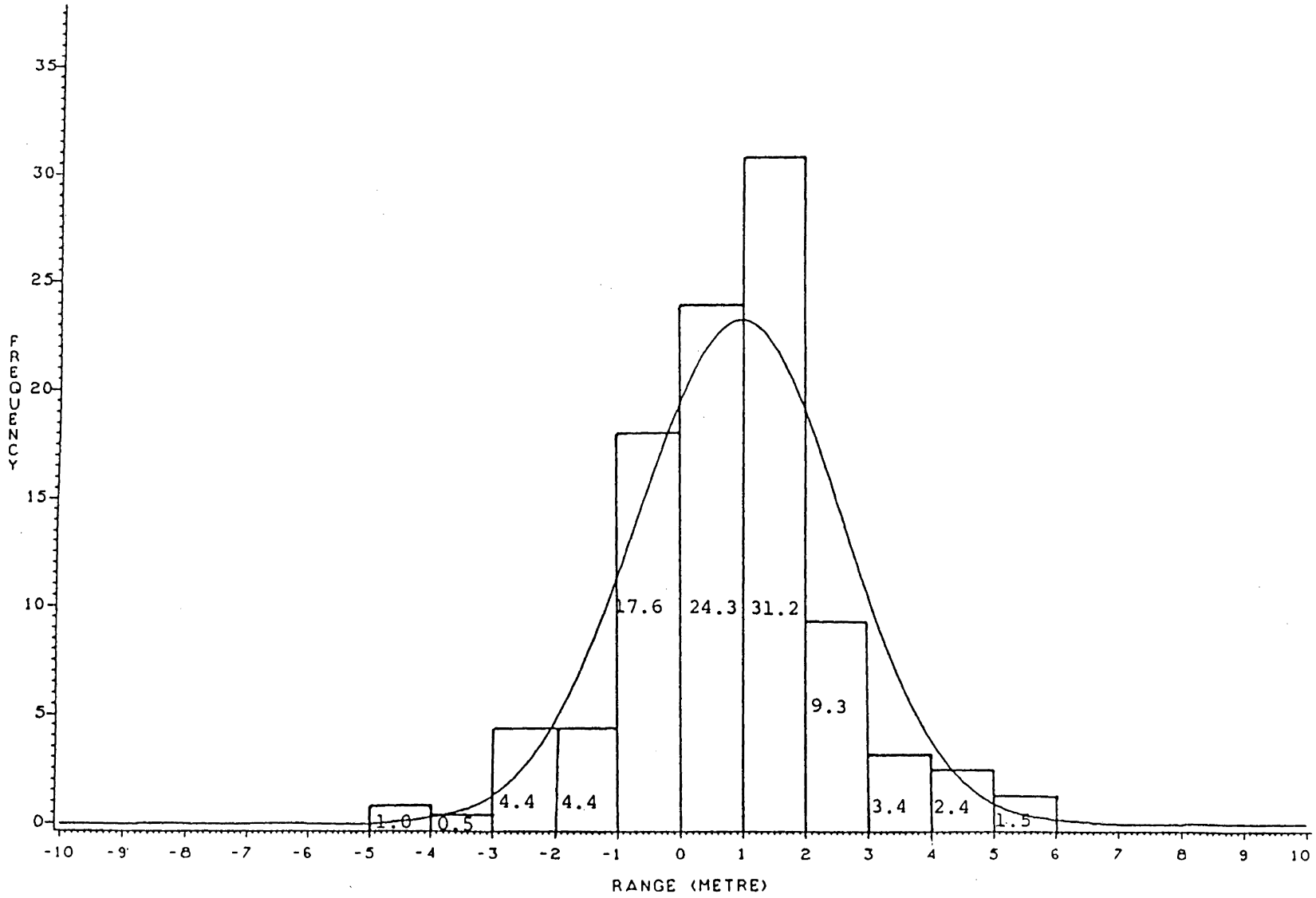

Figure 3.6: Histogram of differences N_D-N_G

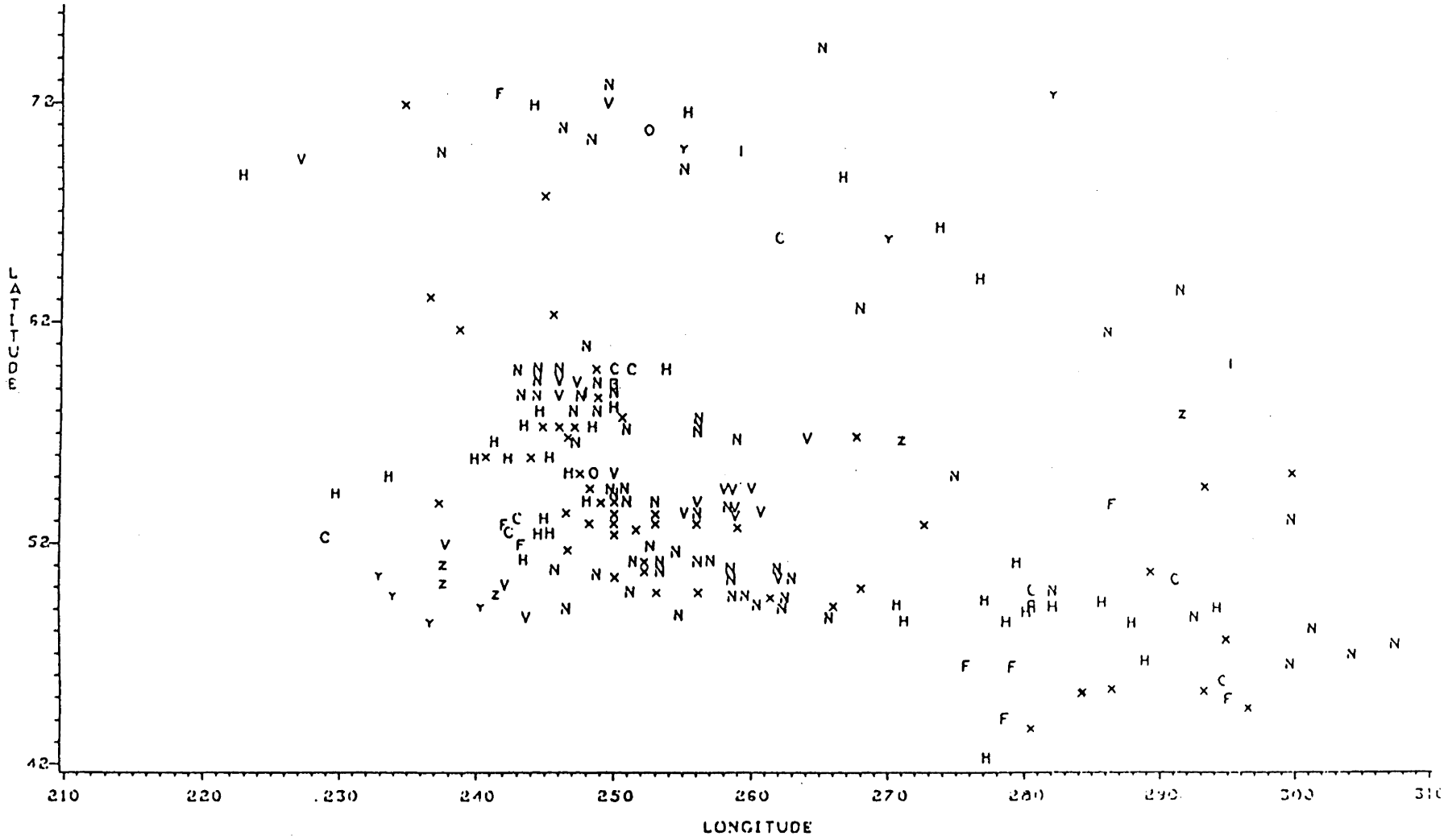

Figure 3.7: "Symbol Plot" of N_D-N_G (Legend: O: -5 m $\leq \delta N <$ -4 m; B: -4 m $\leq \delta N <$ -3 m; C: -3 m $\leq \delta N <$ -2 m; F: -2 m $\leq \delta N <$ -1 m; H: -1 m $\leq \delta N <$ 0 m; X: 0 m $\leq \delta N <$ 1 m; N: 1 m $\leq \delta N <$ 2 m; V: 2 m $\leq \delta N <$ 3 m; Y: 3 m $\leq \delta N <$ 4 m; Z: 4 m $\leq \delta N <$ 5 m; I: 5 m $\leq \delta N <$ 6 m.

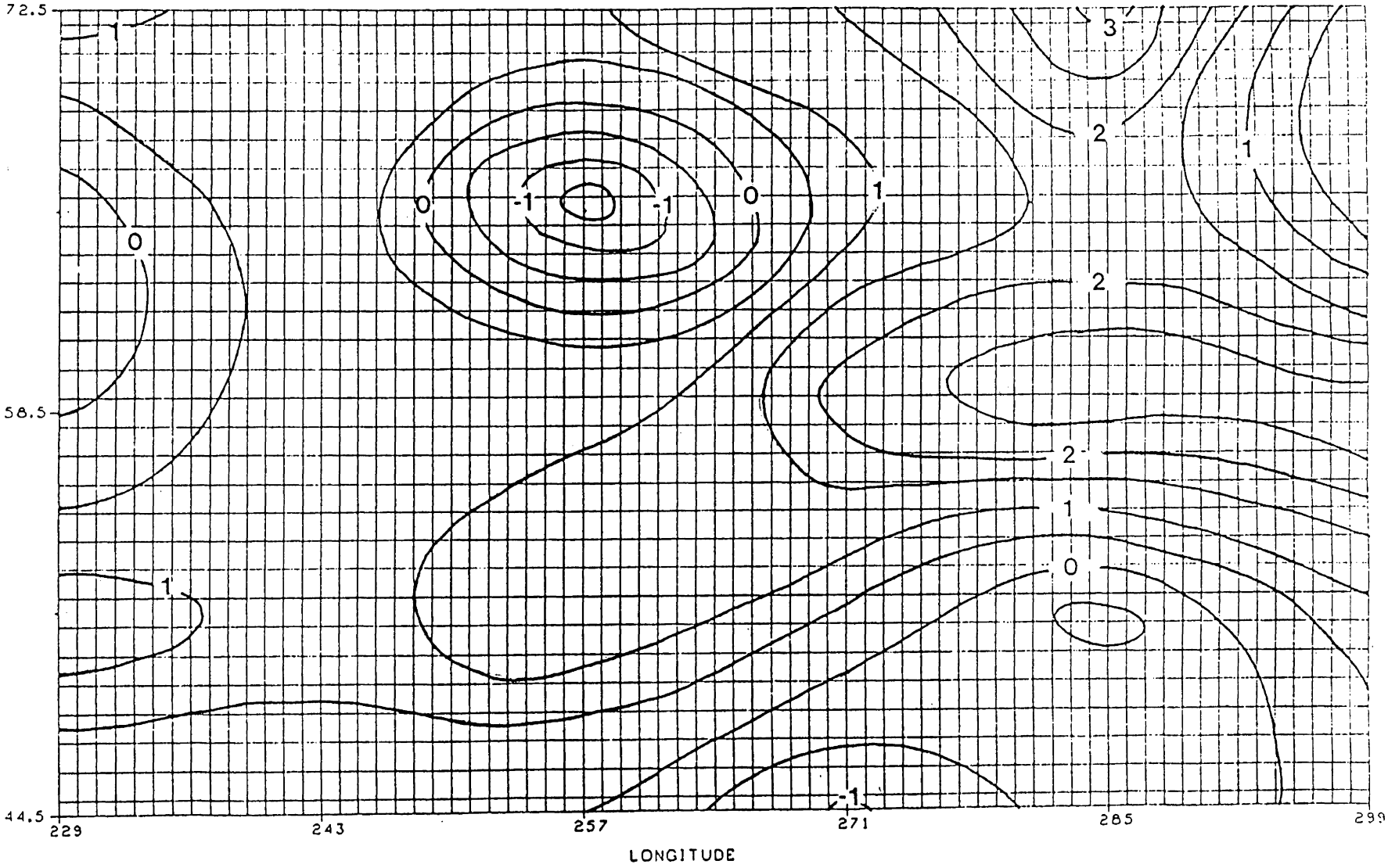

Figure 3.8: Contour Plot of N_D-N_G from 2D Histogram (Contours in Metres)

3.3 Testing of the Gridded Gravimetric Geoid

3.3.1 Gravimetric Geoid on a 10' by 10' Grid

A very detailed gravimetric geoid has been produced on a 10' by 10' grid of points for the whole area covered by the 5' by 5' mean anomalies. Because of the large amount of computer time needed, it was not possible to apply the corrections described in sections 2.2.4, 2.2.5, and 2.2.6, even though these corrections amount to several decimetres. The grid values of the gravimetric geoid presented here are thus not the best values we could compute.

The detailed gravimetric geoid has been produced in 14, 10° by 20° blocks, which are shown in Figures 3.9 through 3.22. Half metre contour lines are used to preserve the wealth of detailed features which should be of interest to interpretative geophysists. Of the many features, we point out the well-defined trough of the lower reaches of the St. Lawrence River. The complexity of the geoid in the Rockies is also worth noting.

When producing the geoid off the western seaboard, we discovered an area ($\phi \in \langle 53°, 55° \rangle$, $\lambda \in \langle 225°, 227° \rangle$) where the 5' by 5' mean anomalies reach values of up to minus 440 mGal (with standard deviations of the order of 5 to 10 mGal). Yet these values are not reflected in the 1° by 1° file, where the four mean anomalies have values of only -23, -31, -42, and 24 mGal (with standard deviations of 4 and 5 mGal).

This discrepancy between the two data files has produced an artifact in the computed gravimetric geoid—a fairly localized depression of more than 10 metres (see Figure 3.23)—traceable back to the inner zone contribution. Rather than attempting to clean up the $\bar{\Delta}g$ files, we have decided to discard the results (N_G) from the 'diseased' area (cf. Figure 3.14).

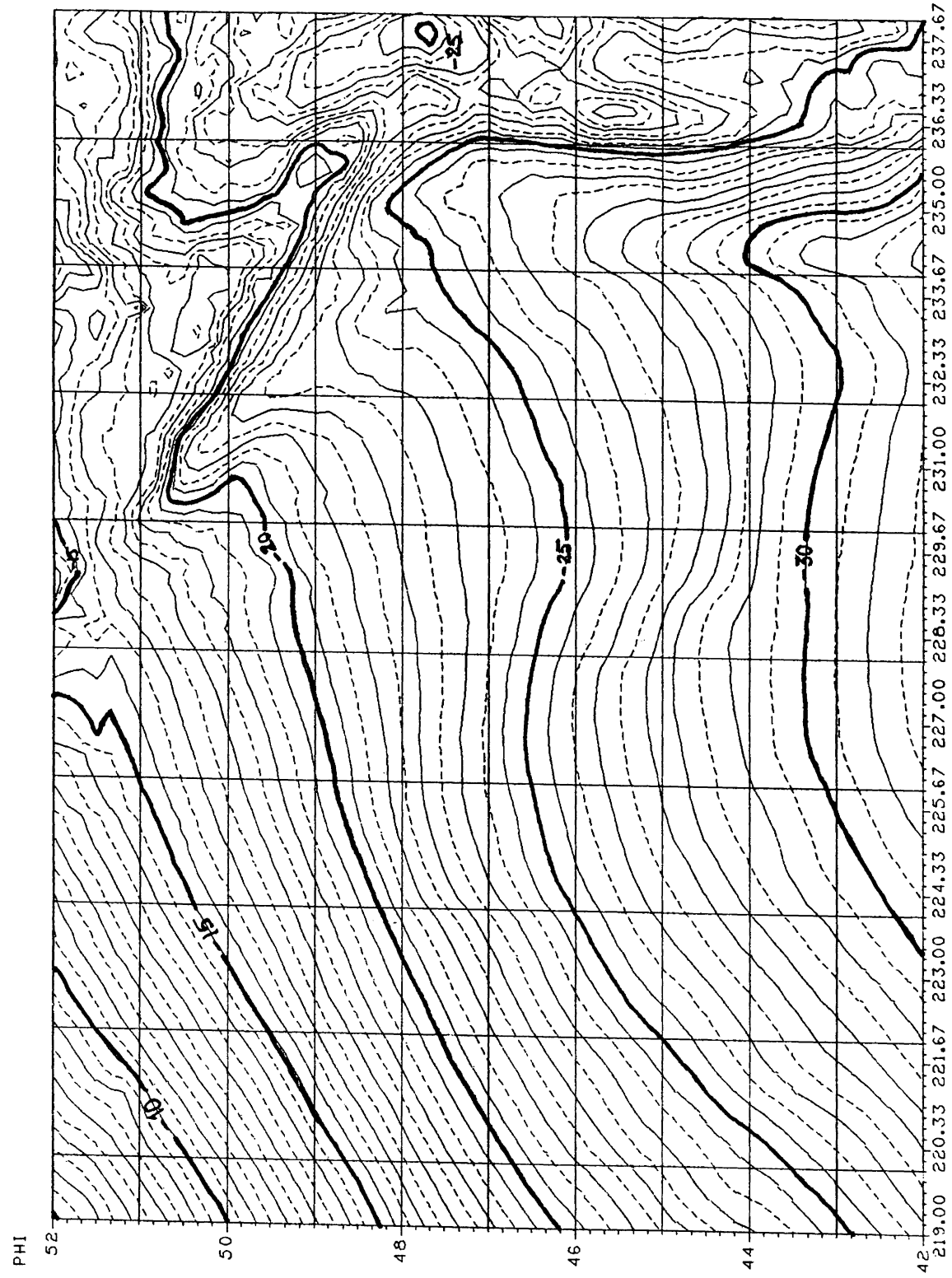

Figure 3.9: The gravimetric geoid.

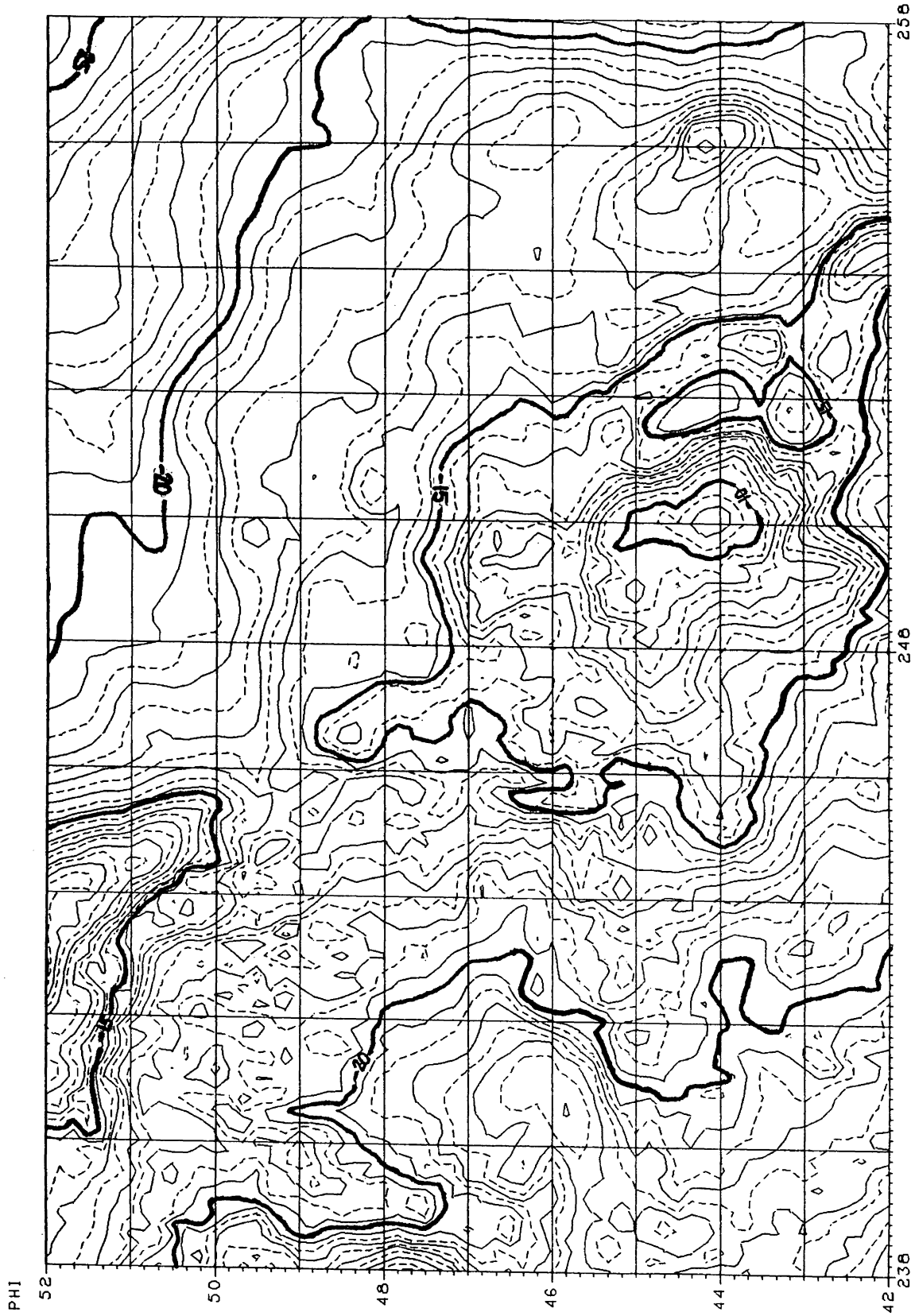

Figure 3.10: The gravimetric geoid.

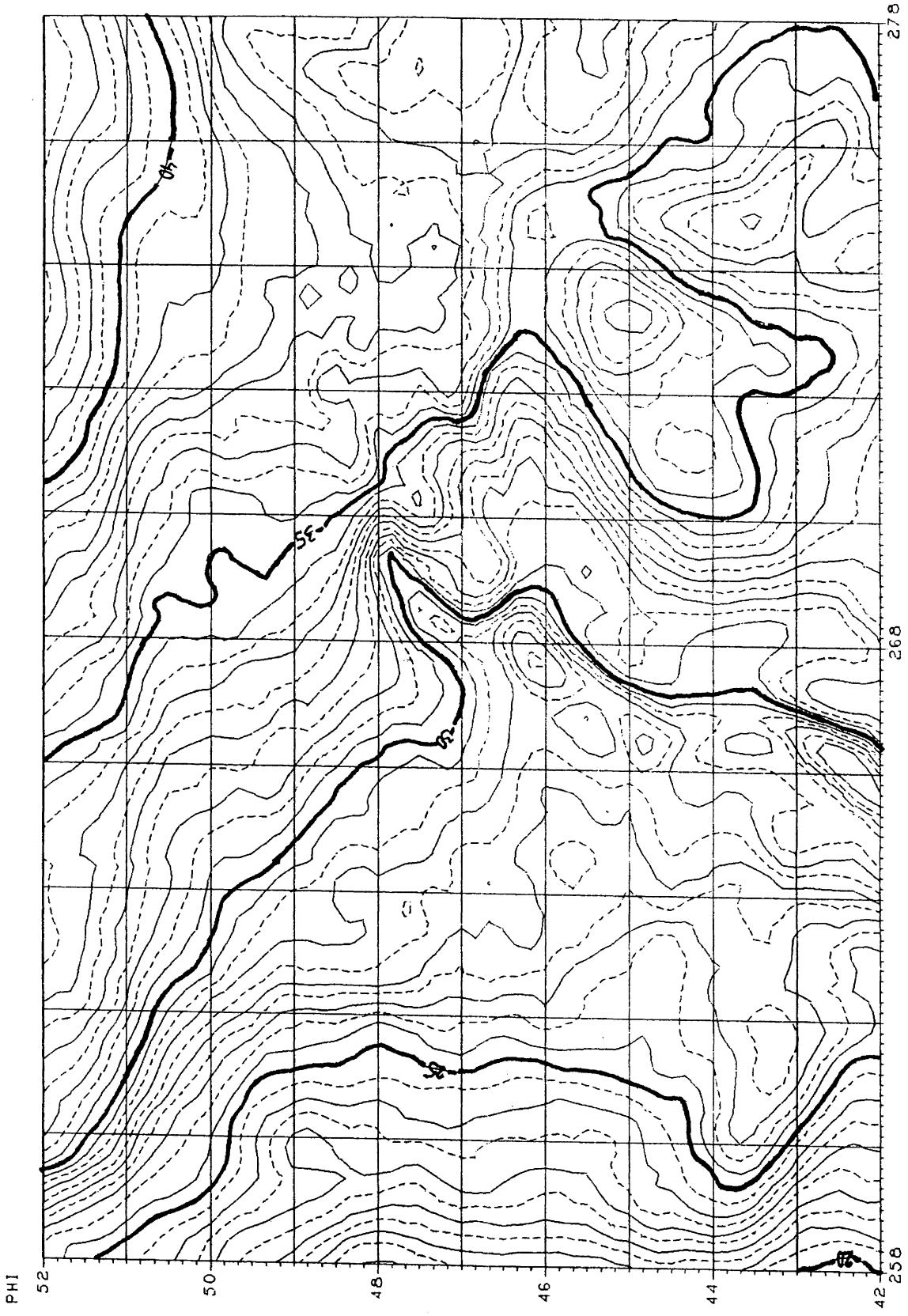

Figure 3.11: The gravimetric geoid.

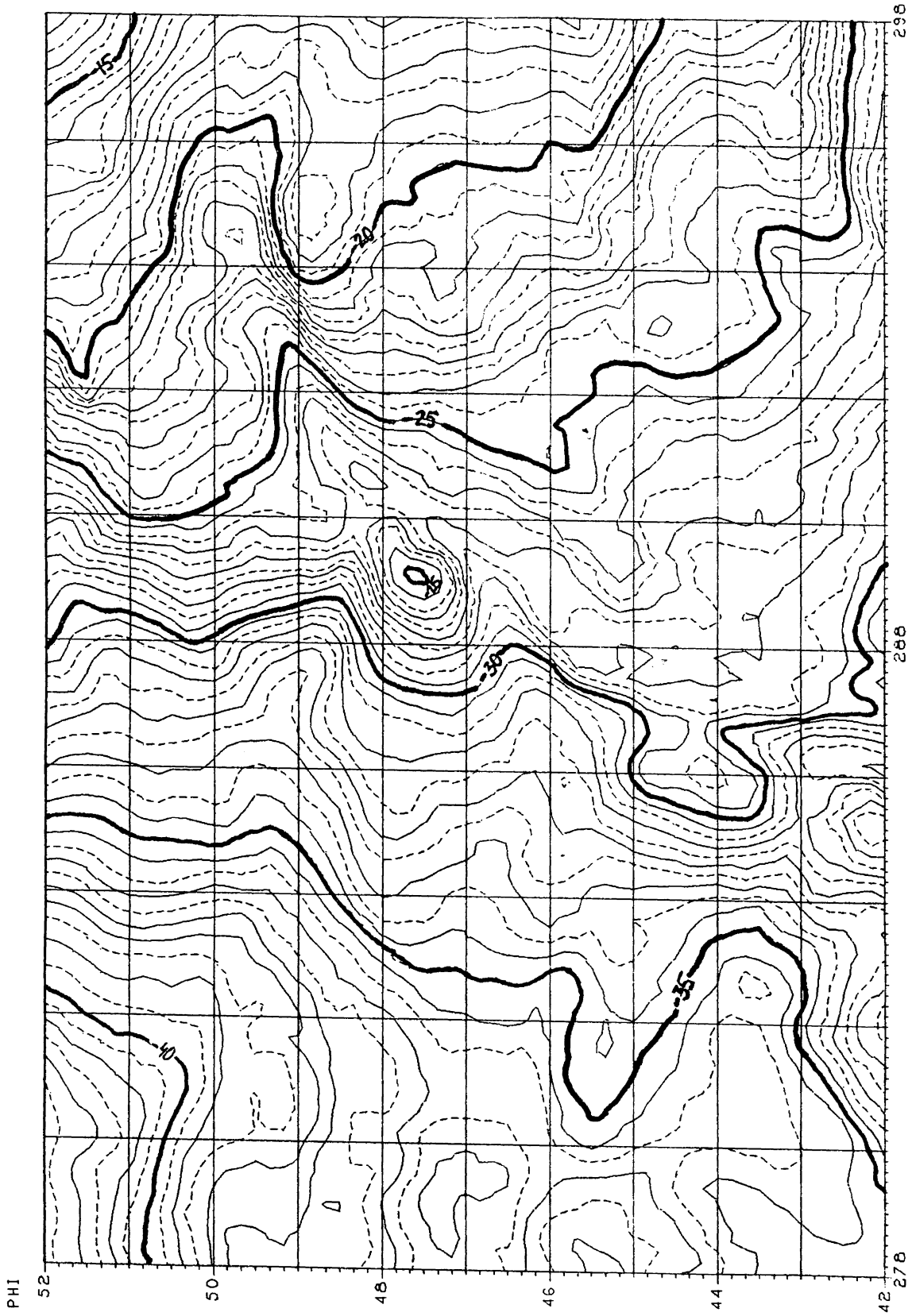

Figure 3.12: The gravimetric geoid.

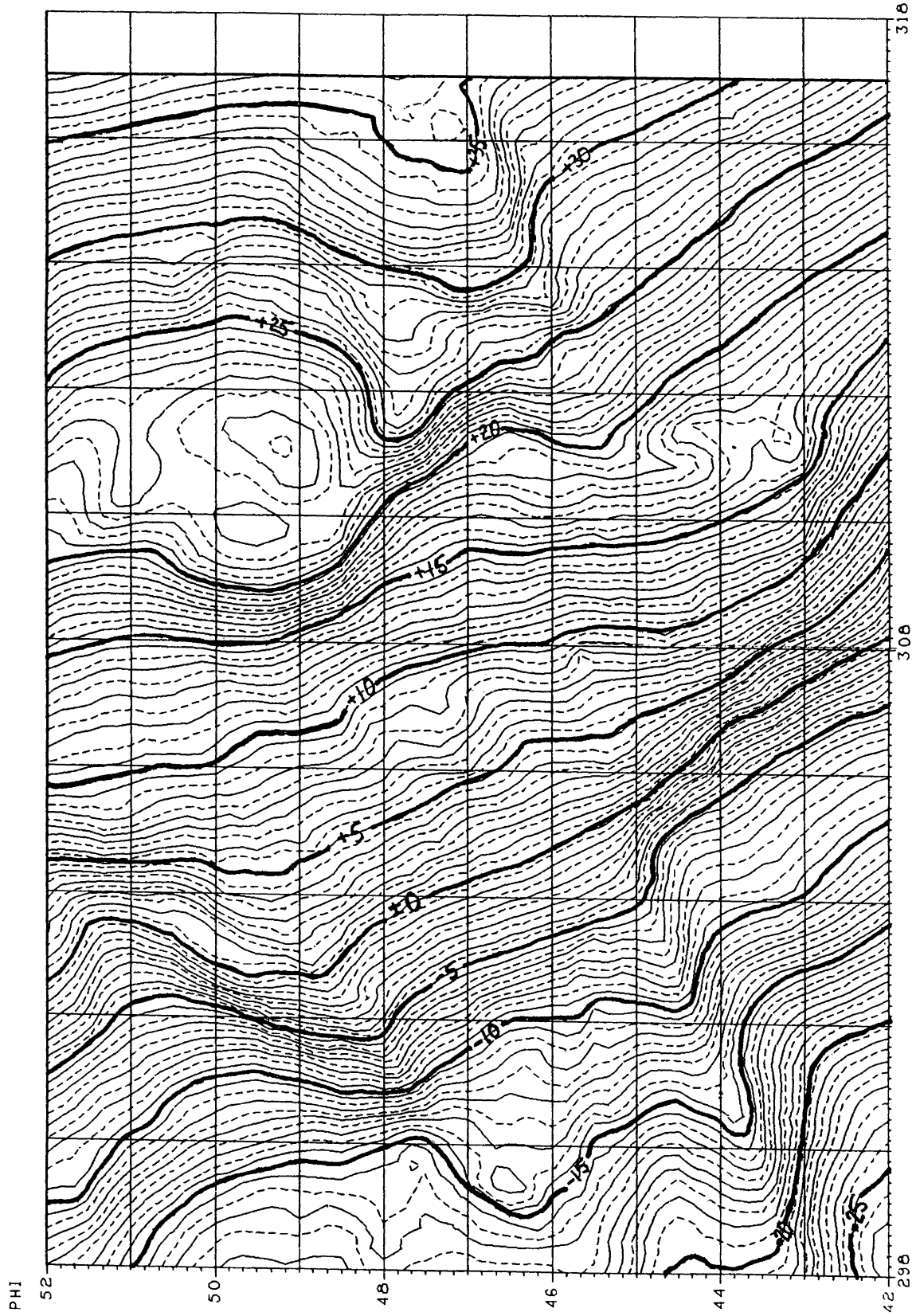

Figure 3.13: The gravimetric geoid.

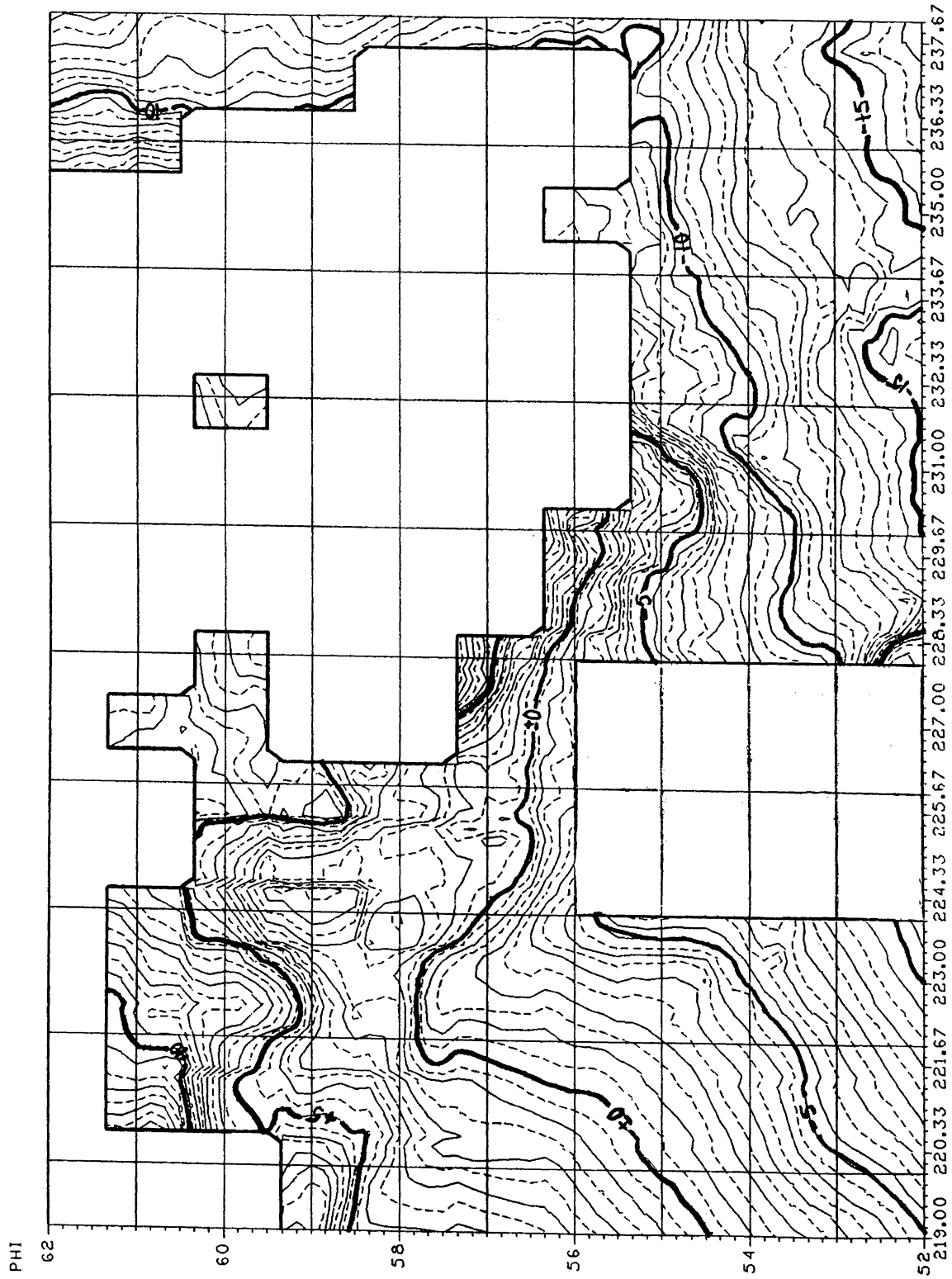

Figure 3.14: The gravimetric geoid.

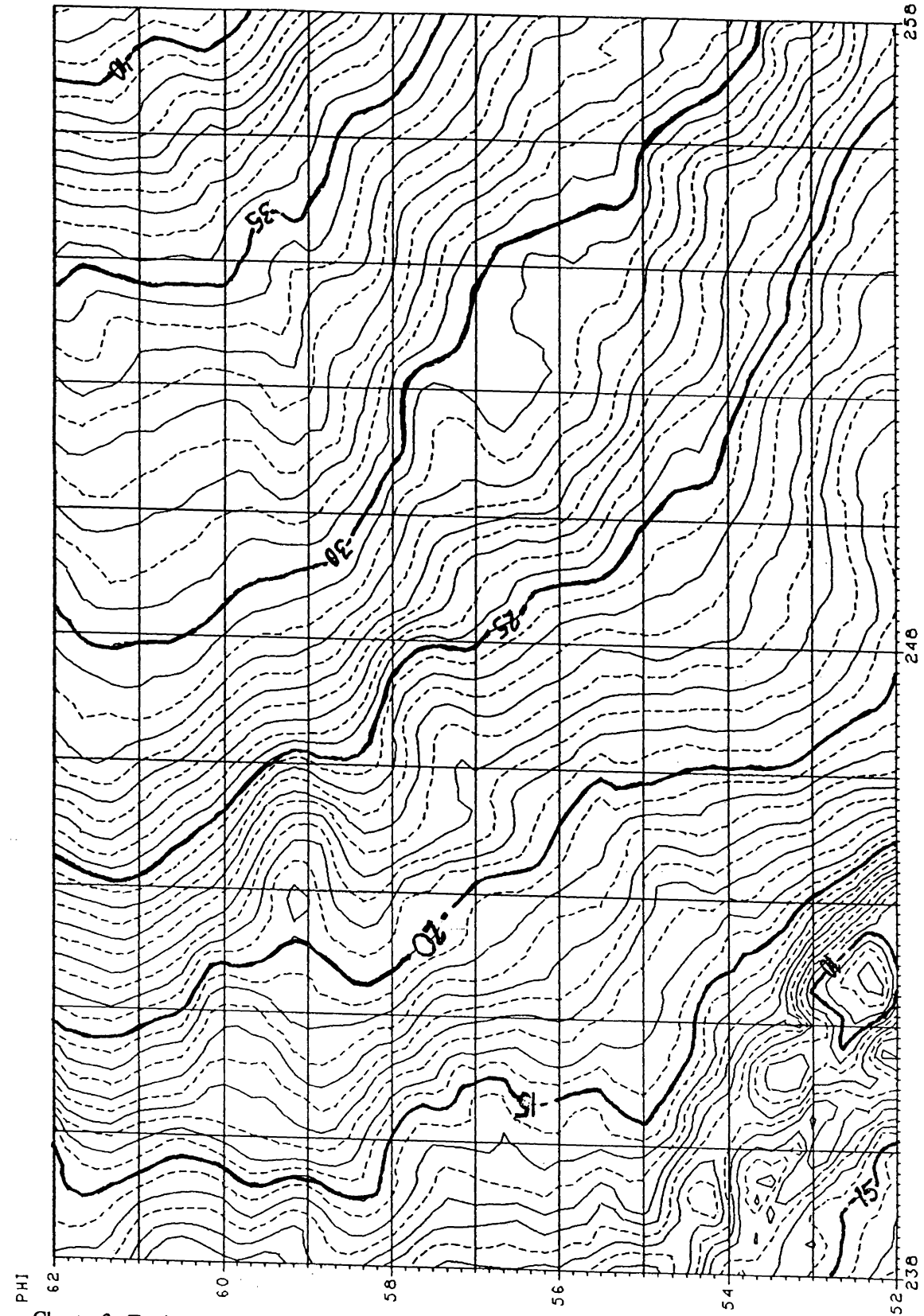

Figure 3.15: The gravimetric geoid.

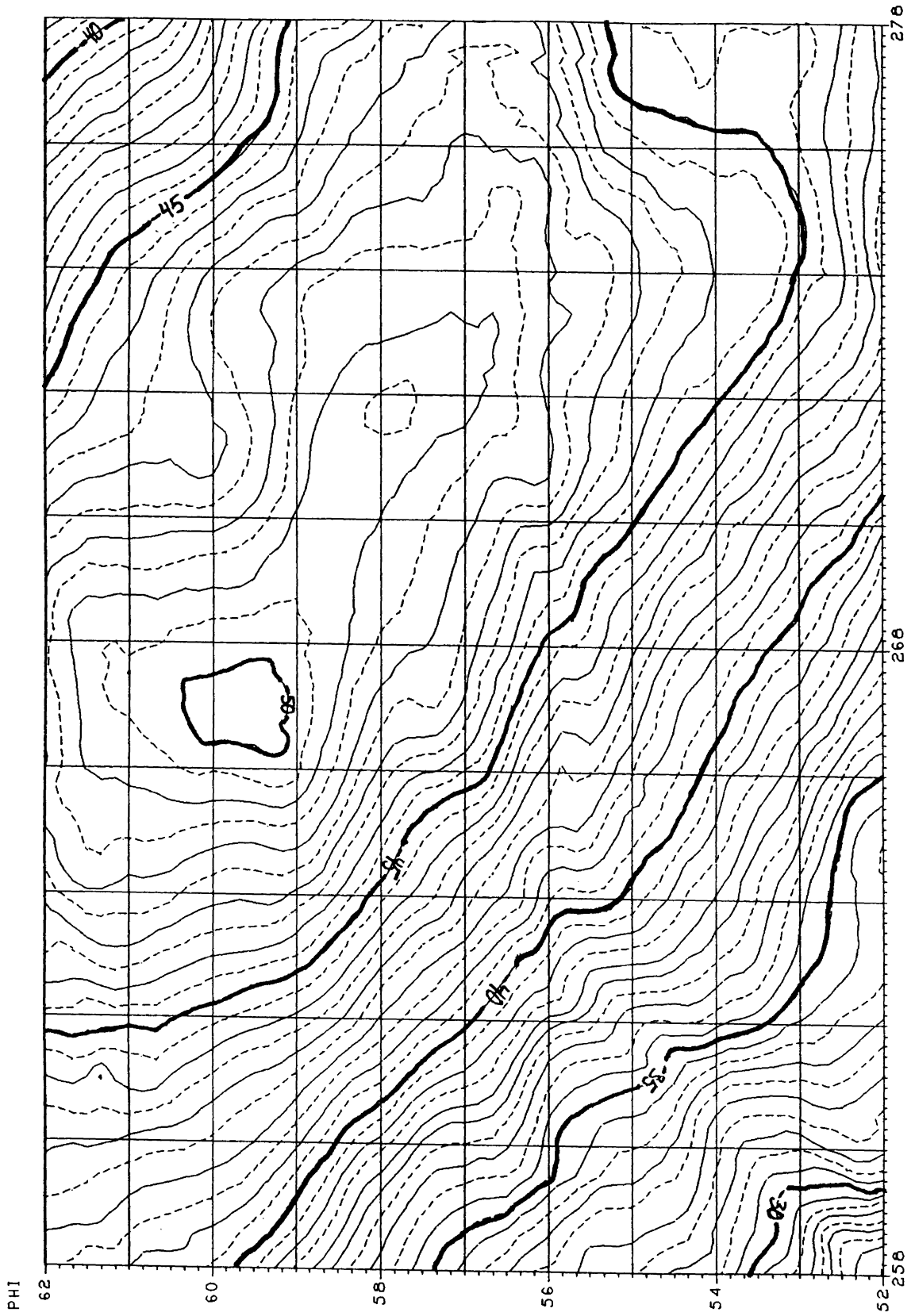

Figure 3.16: The gravimetric geoid.

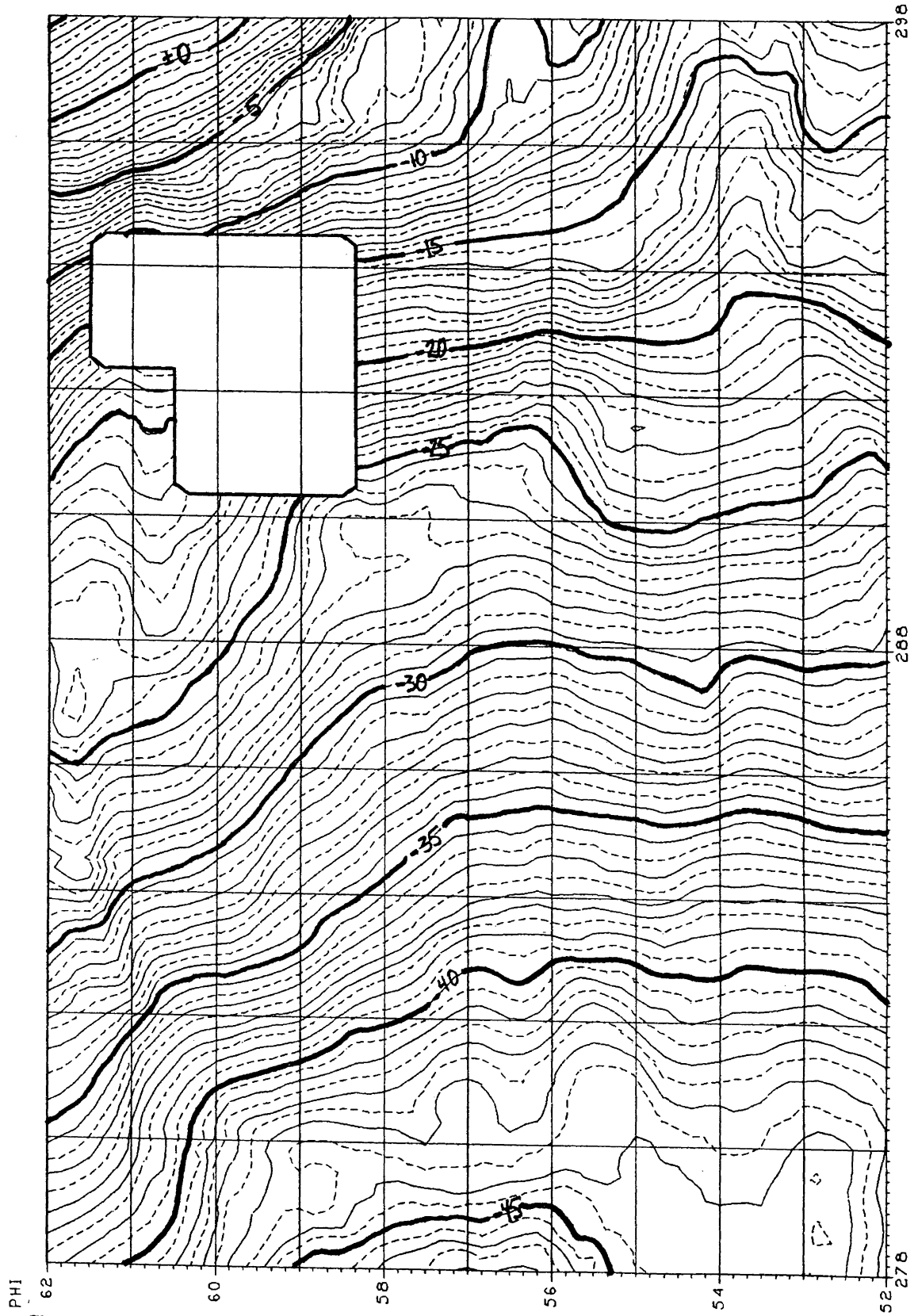

Figure 3.17: The gravimetric geoid.

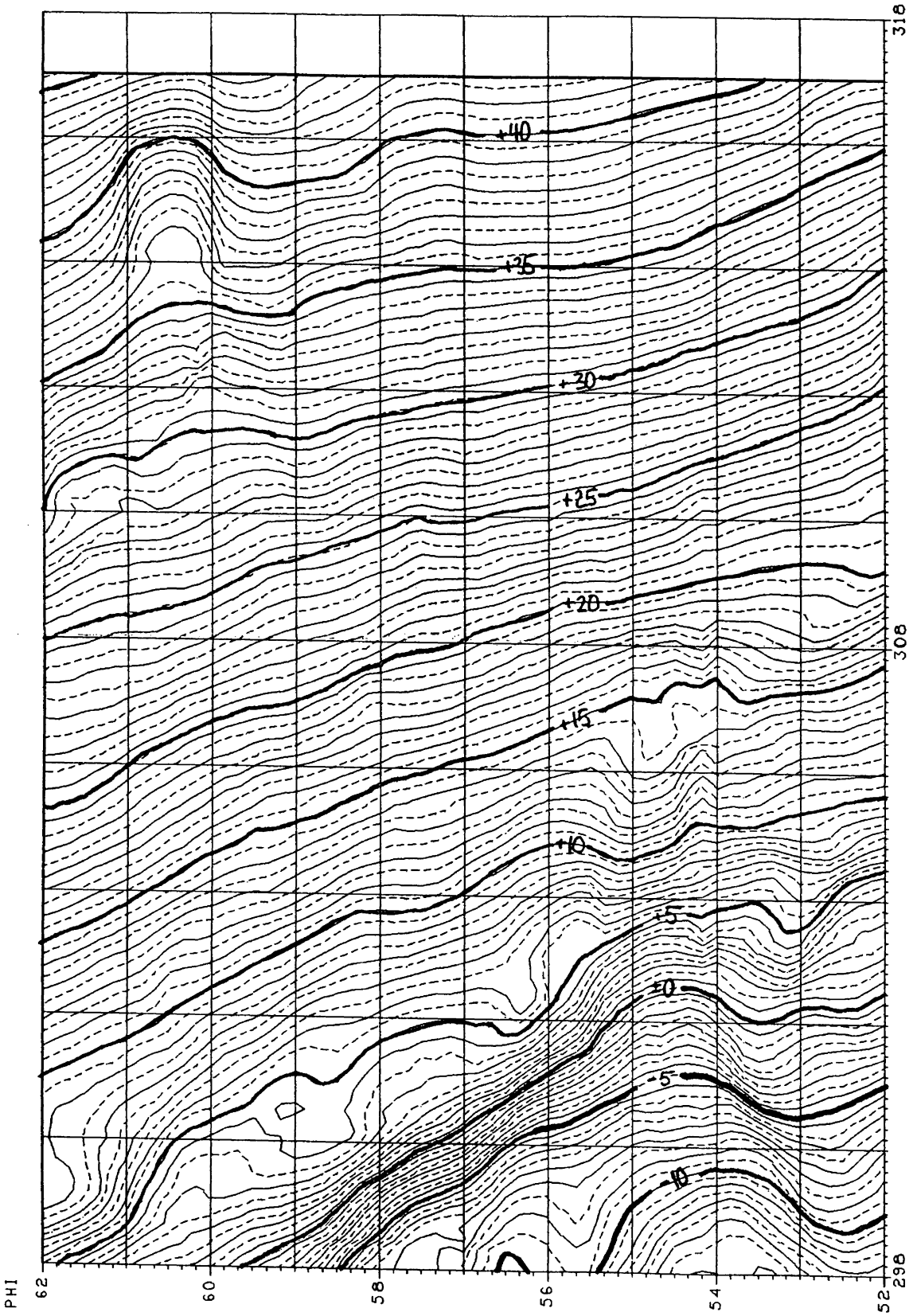

Figure 3.18: The gravimetric geoid.

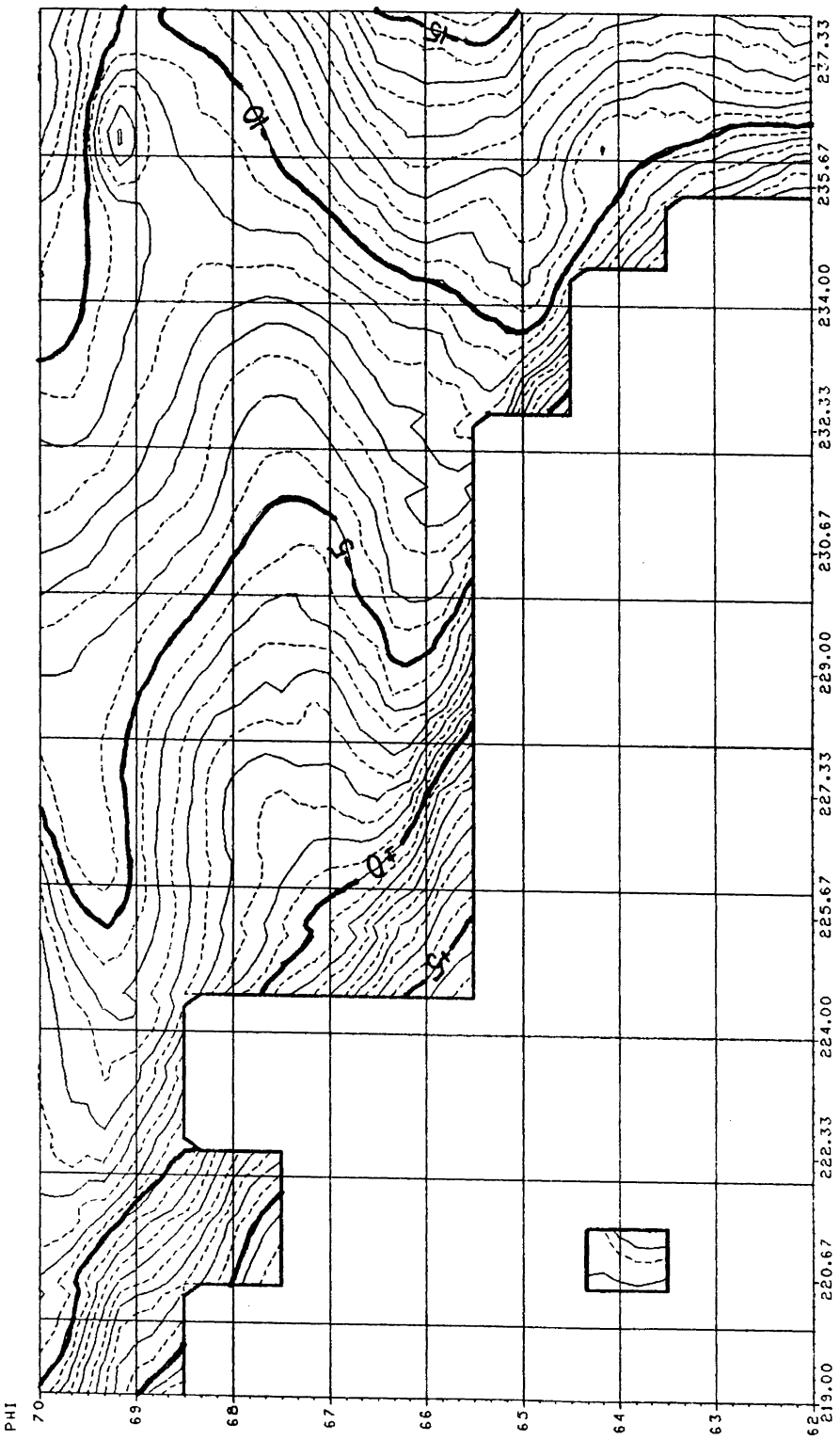

Figure 3.19: The gravimetric geoid.

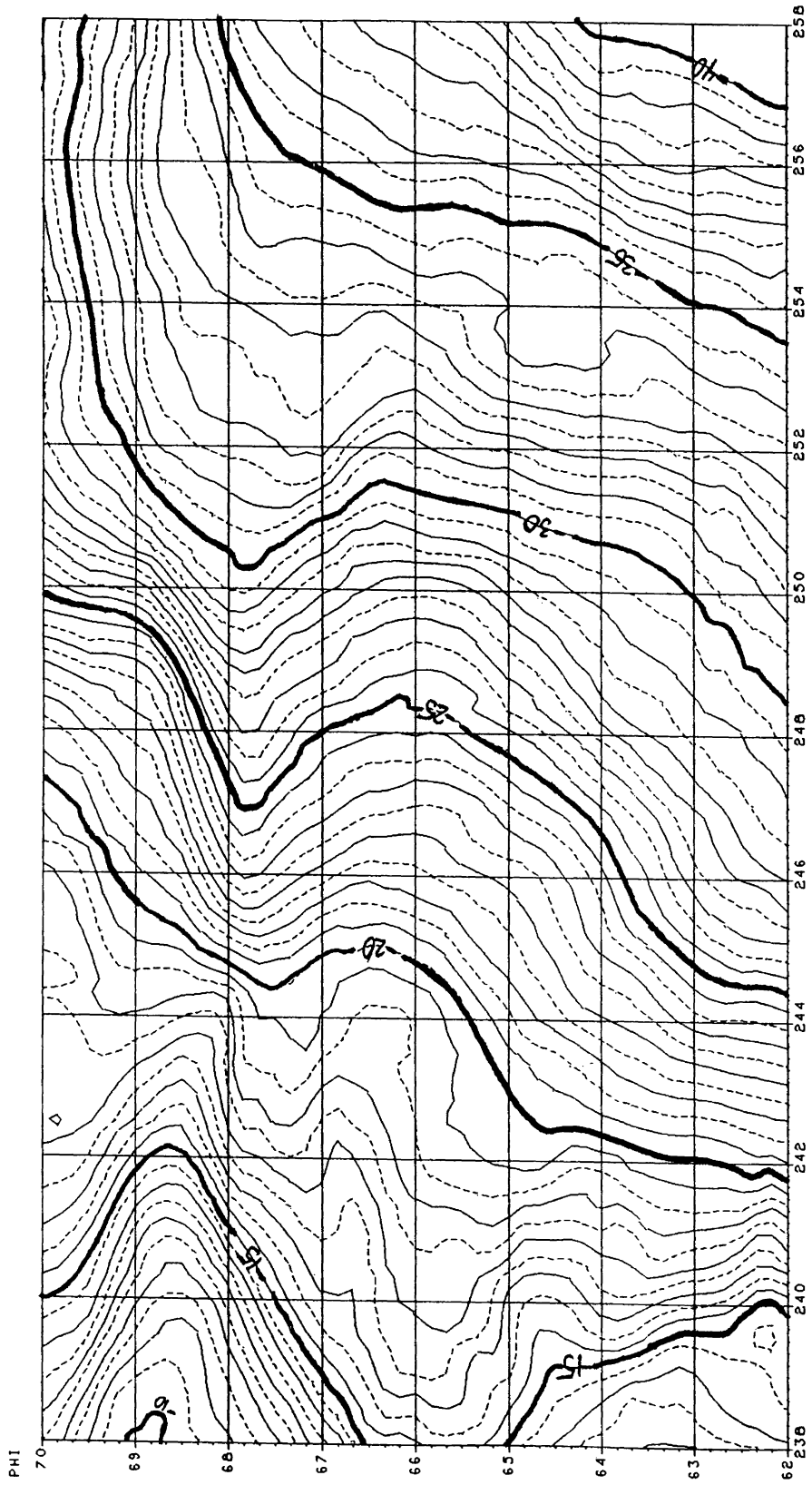

Figure 3.20: The gravimetric geoid.

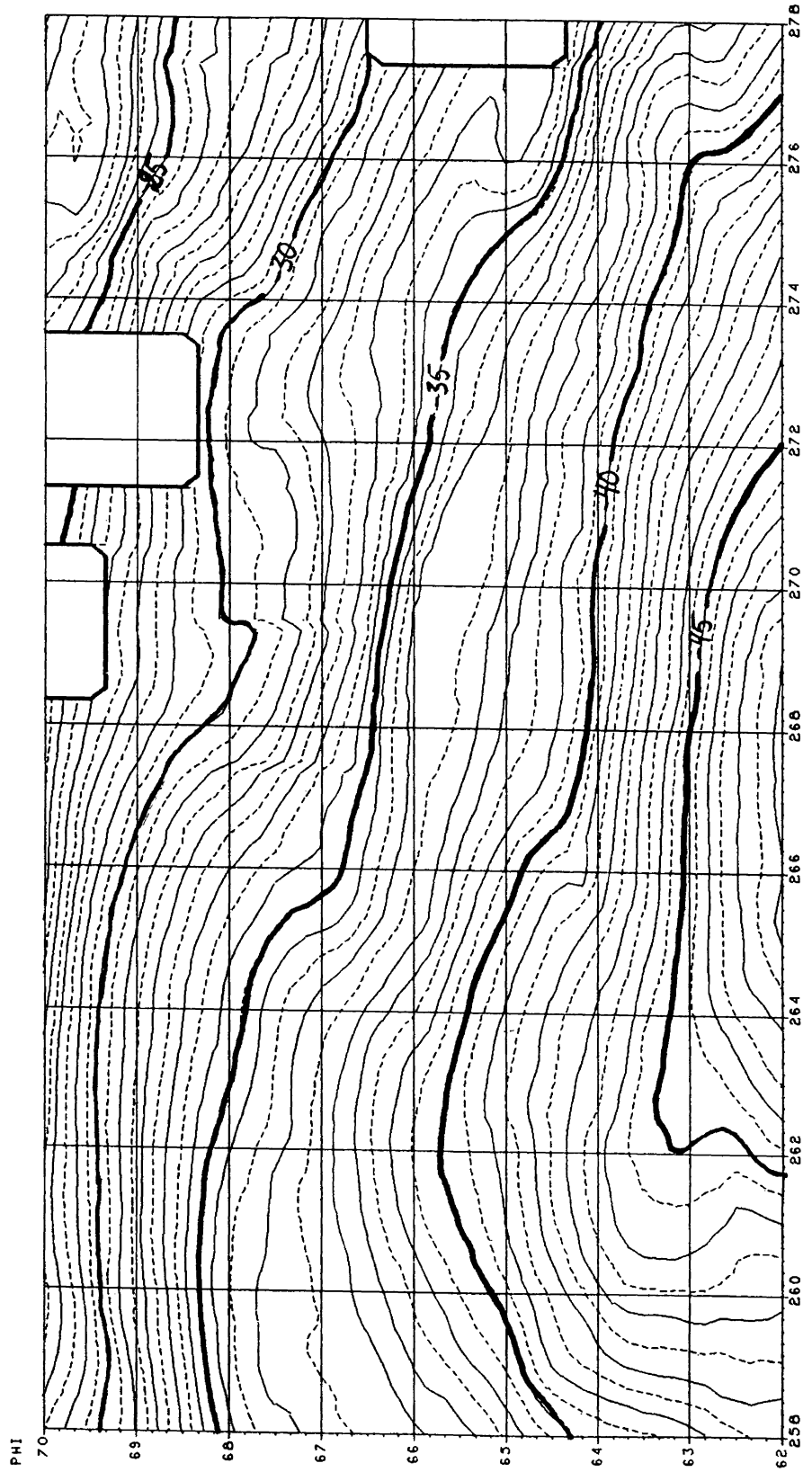

Figure 3.21: The gravimetric geoid.

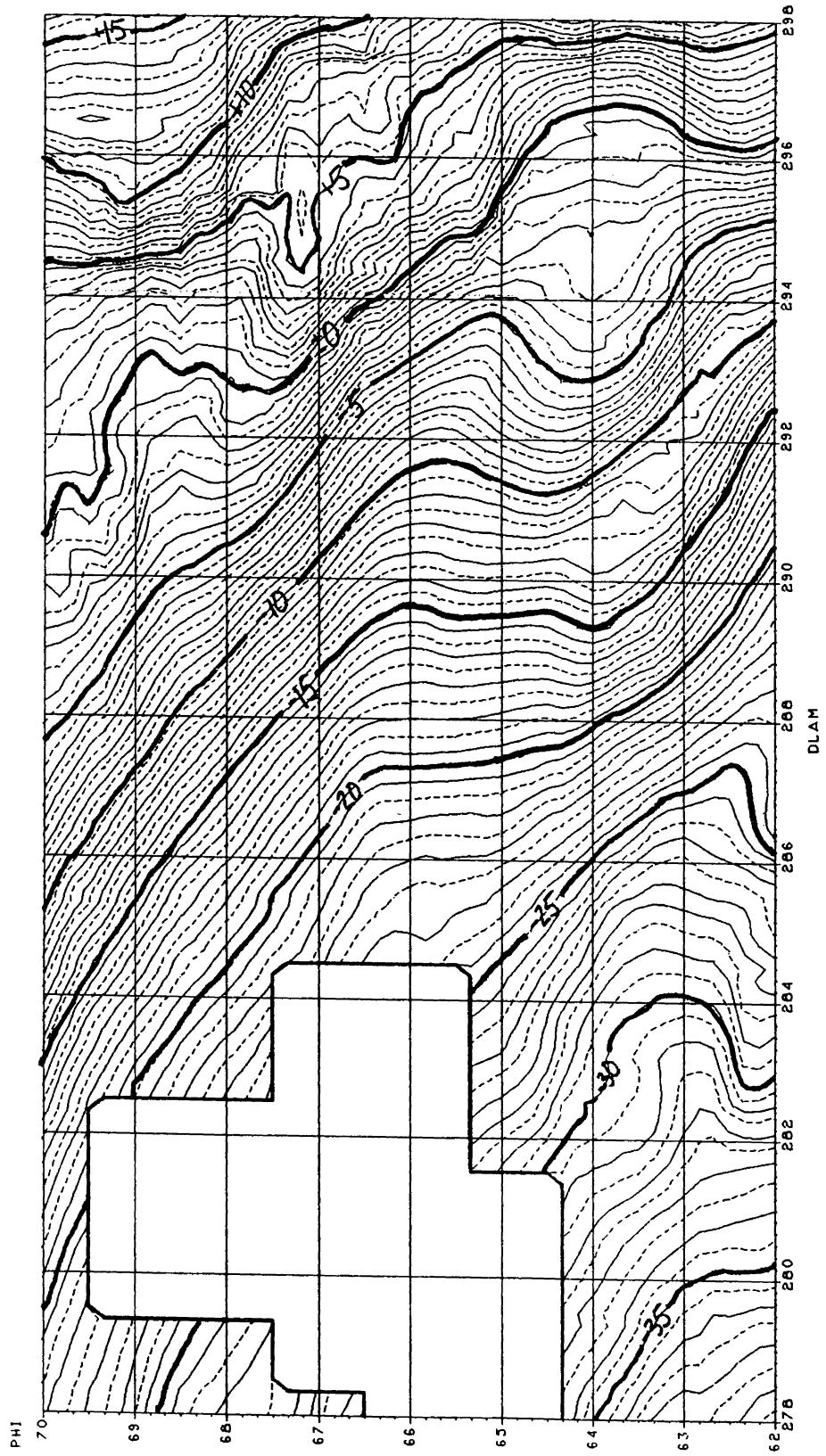

Figure 3.22: The gravimetric geoid.

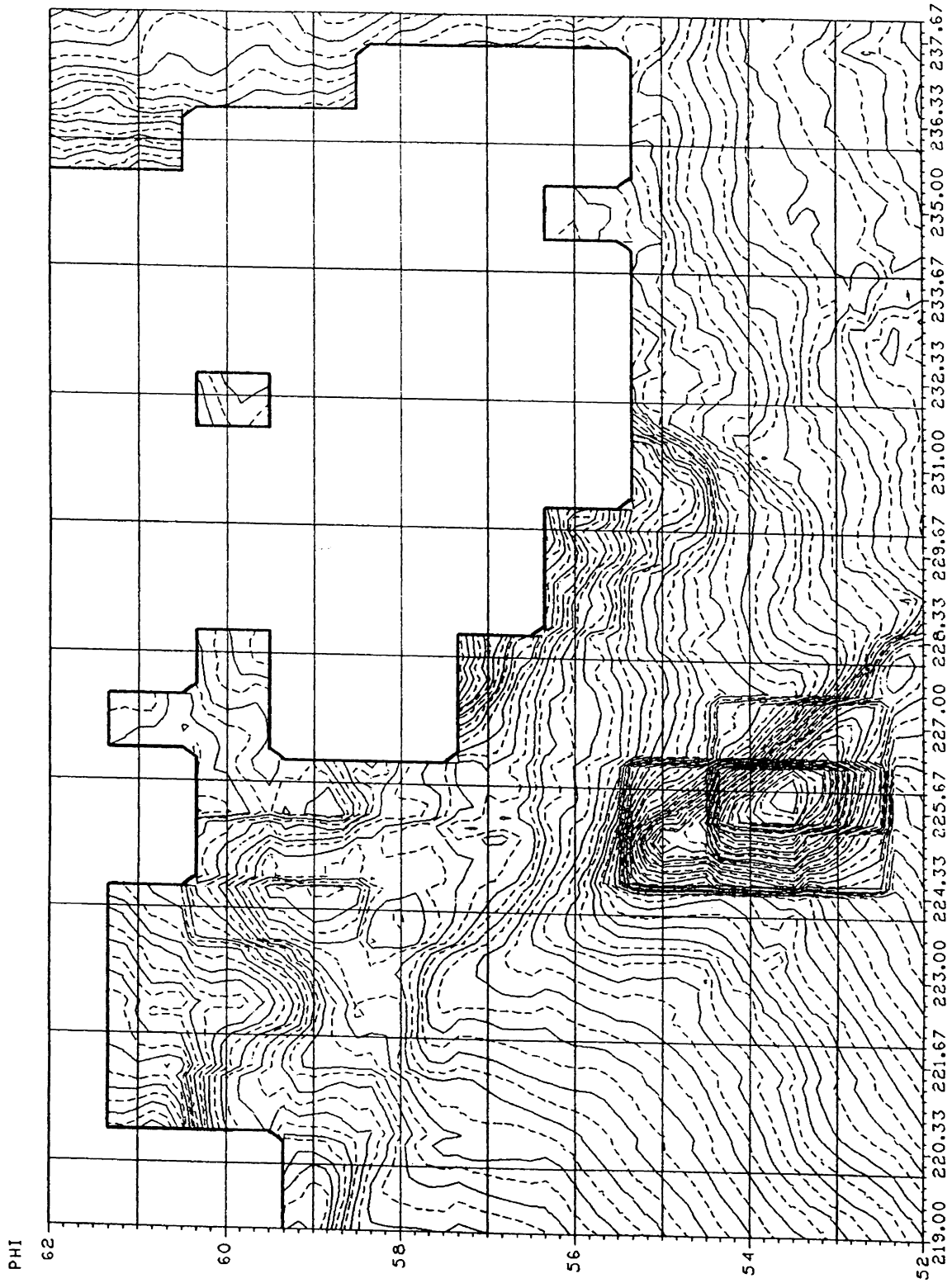

Figure 3.23: Illustration of an artifact of blunders in the data.

3.3.2 Comparison with Rapp's 180 × 180 Solution

To further test the accuracy of our gravimetric solution, the values on the 1° by 1° grid have been generated (Figure 3.24) and compared to corresponding 1° by 1° values of Rapp's 180 × 180 solution [Rapp, 1983b]. The differences (UNB-Rapp) are plotted in Figure 3.25. We can distinguish two quite different features; a long wavelength difference with an amplitude of 1 to 2 metres, and several localized variations of similar amplitude.

The long wavelength discrepancy, extending all over Canada, is most likely due to the differences in the low degree coefficients of the Rapp [1983b] and the GEM9 spherical harmonic expansions. Any error in the GEM9 spheroid leads to small long wavelength errors in the gravimetric geoid (cf. Chapter 2).

Statistical analysis of 1924 geoid differences shows a mean of $\mu = +0.94$ m. The RMS with respect to μ is 1.06 m.

3.3.3 Comparison with Altimetry

In the marine regions, the gravimetric geoid has been compared with the sea surface height derived from SEASAT satellite altimetry—the OSU file (see section 4.2.2). Since no precise altimetry was available for the Pacific areas, this comparison was restricted to the Atlantic Ocean and Hudson Bay. For this purpose, both the gravimetric geoid and the altimetric sea surface height on a 10' by 10' grid were used. The differences, UNB geoid minus altimetry, are plotted in Figures 3.26 through 3.32. No attempt was made to subtract the sea surface topography from the altimetric data set.

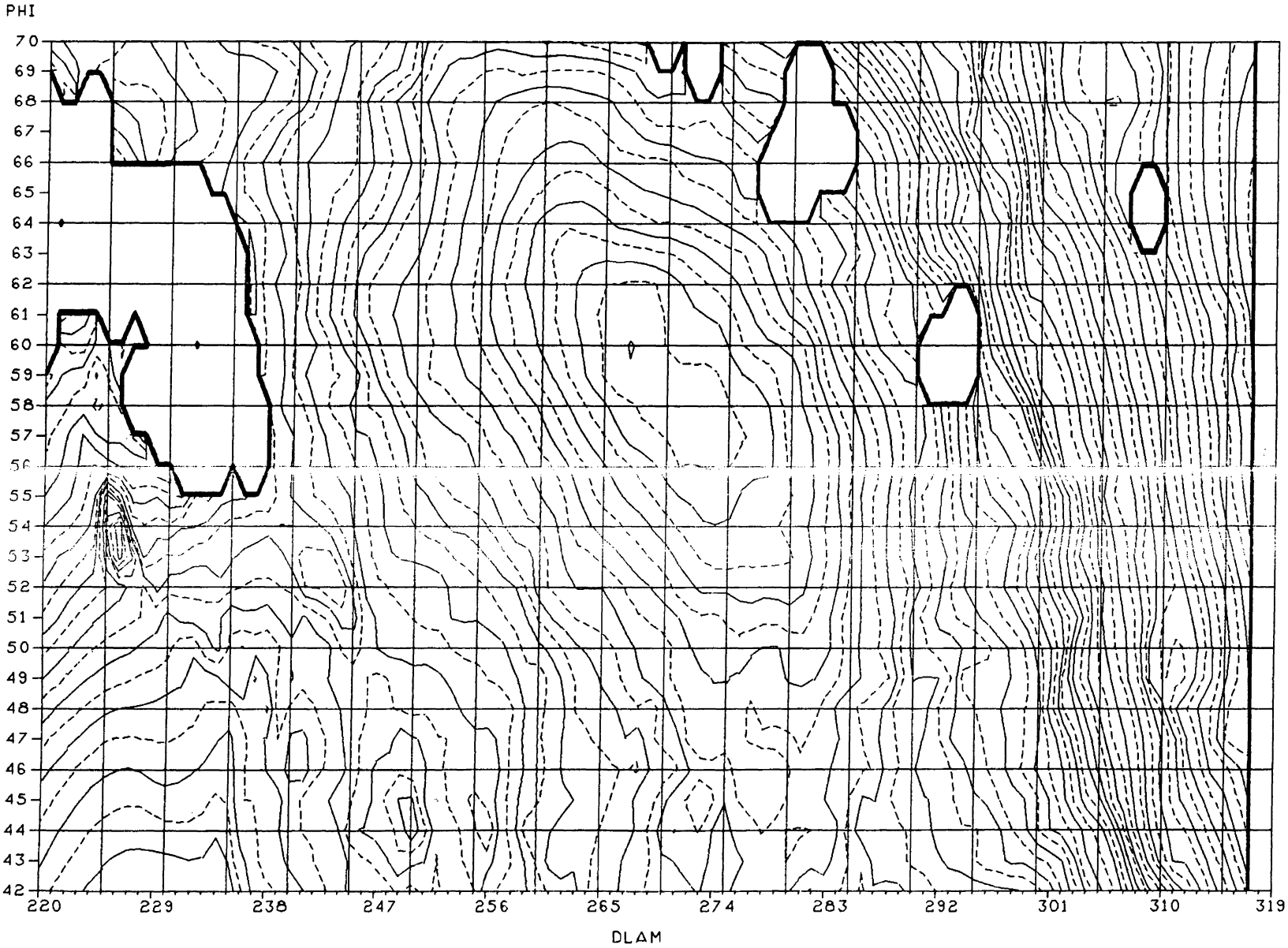

Figure 3.24: The gravimetric geoid.

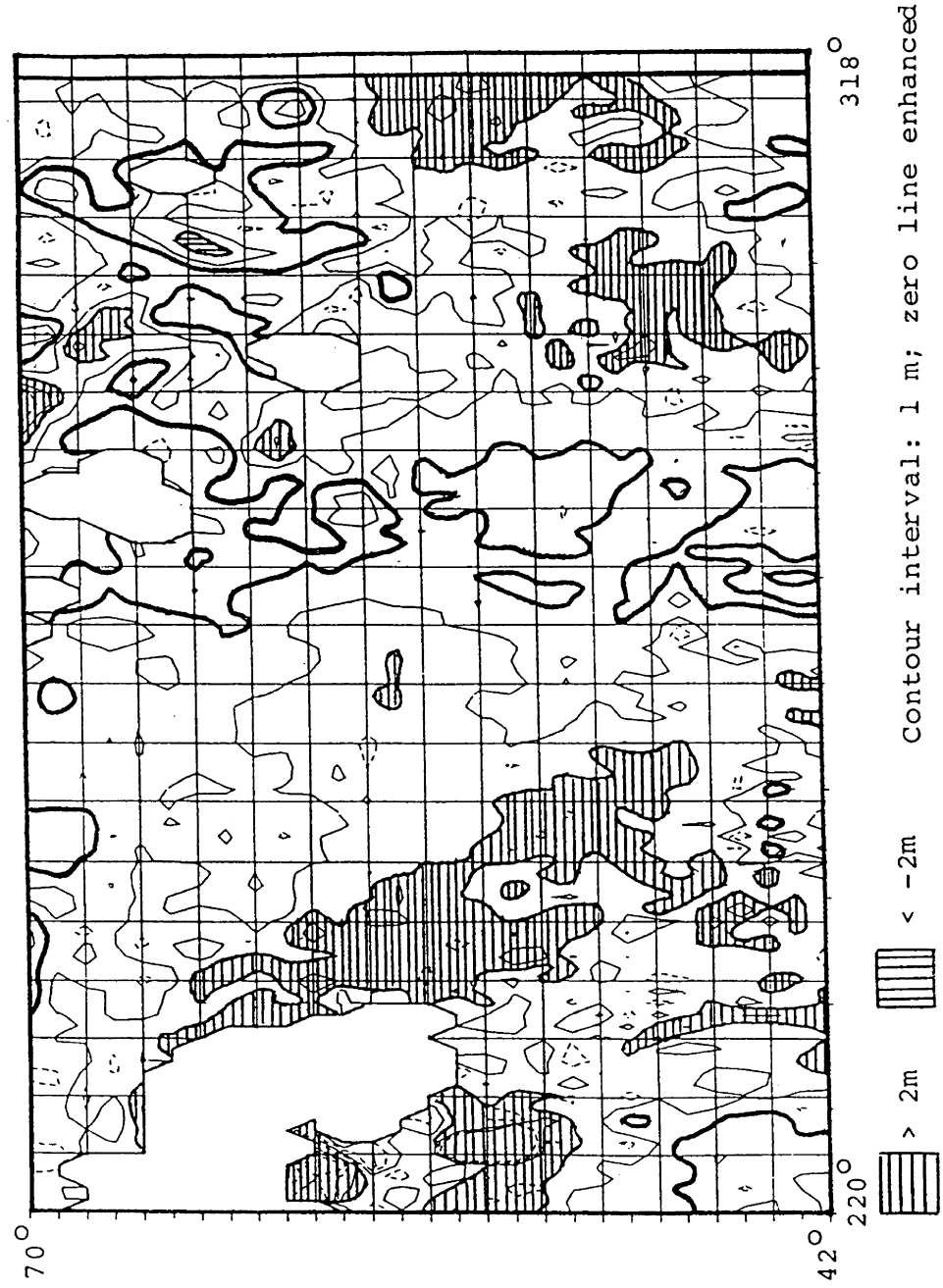

Figure 3.25: UNB gravimetric geoid minus Rapp's 180 x 180 solution.

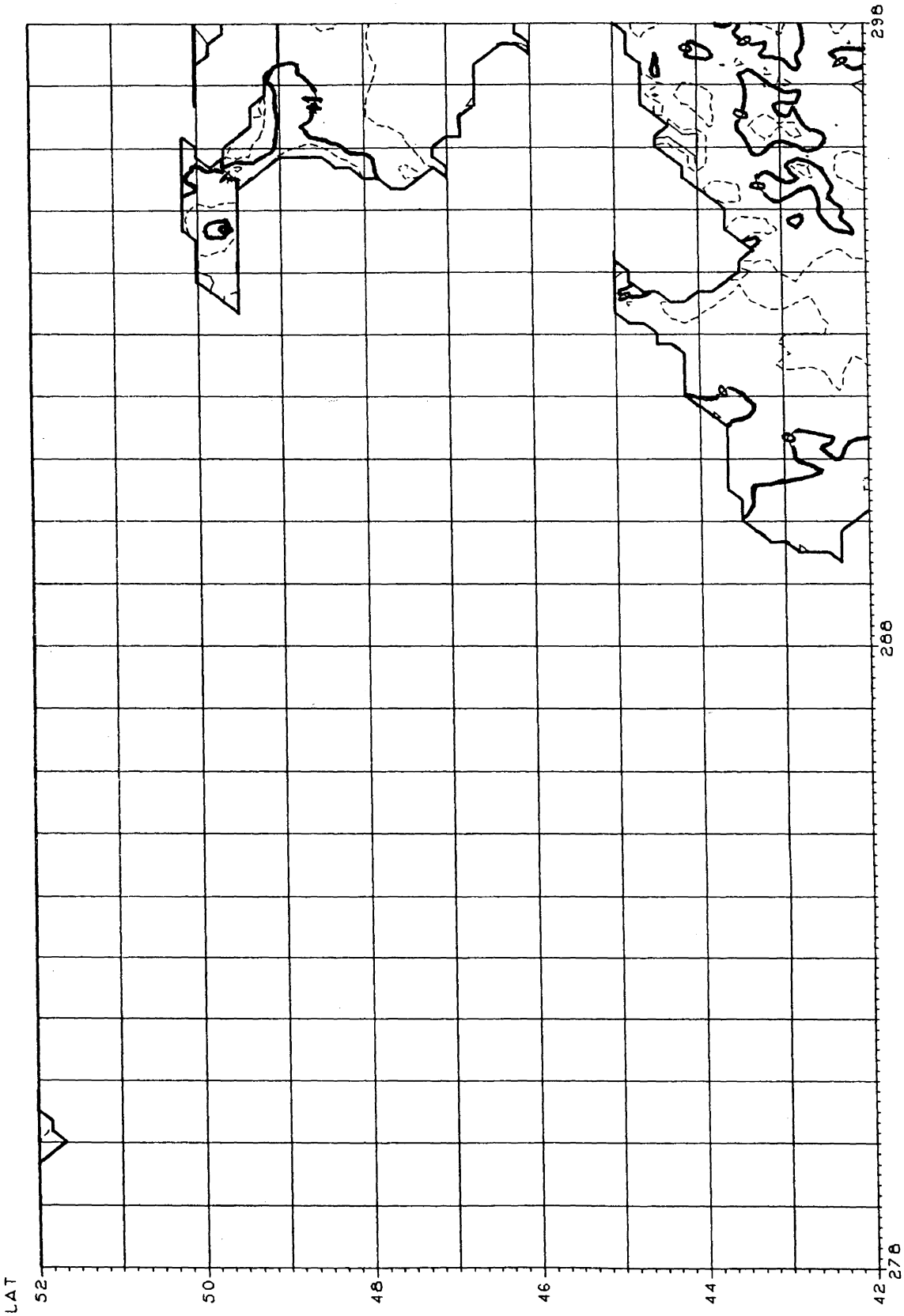

Figure 3.26: UNB geoid minus altimetry.

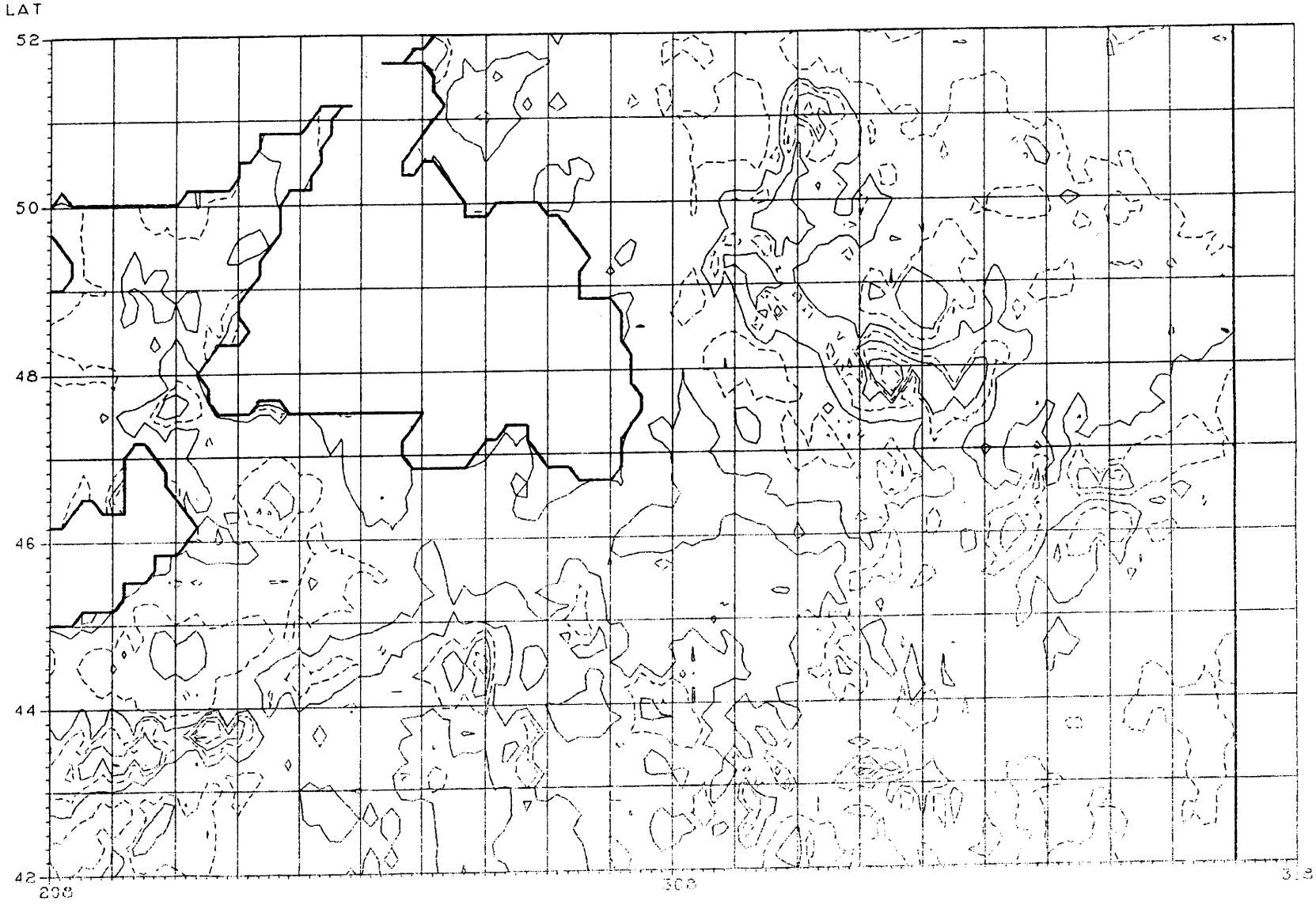

Figure 3.27: UNB geoid minus altimetry

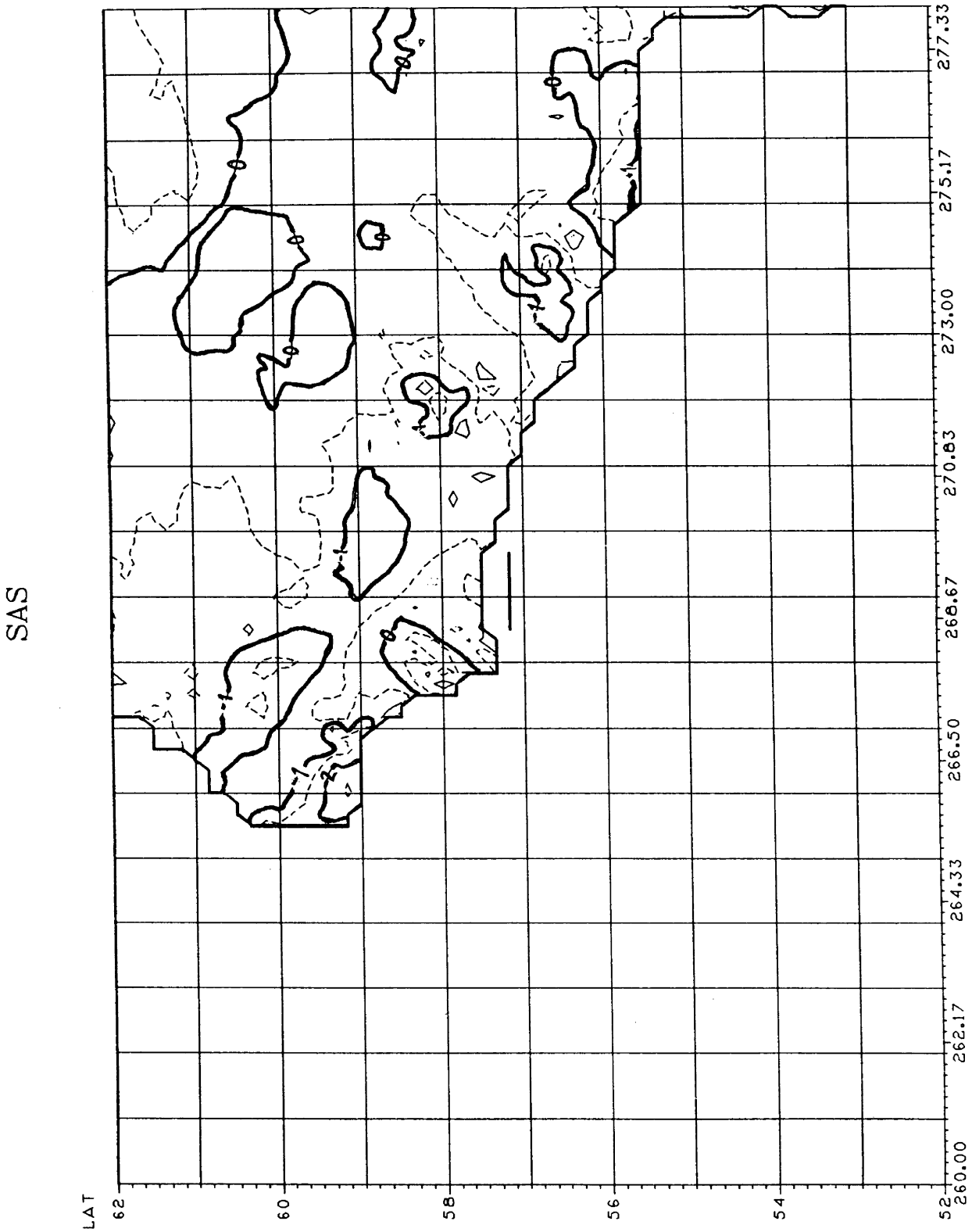

Figure 3.28: UNB geoid minus altimetry.

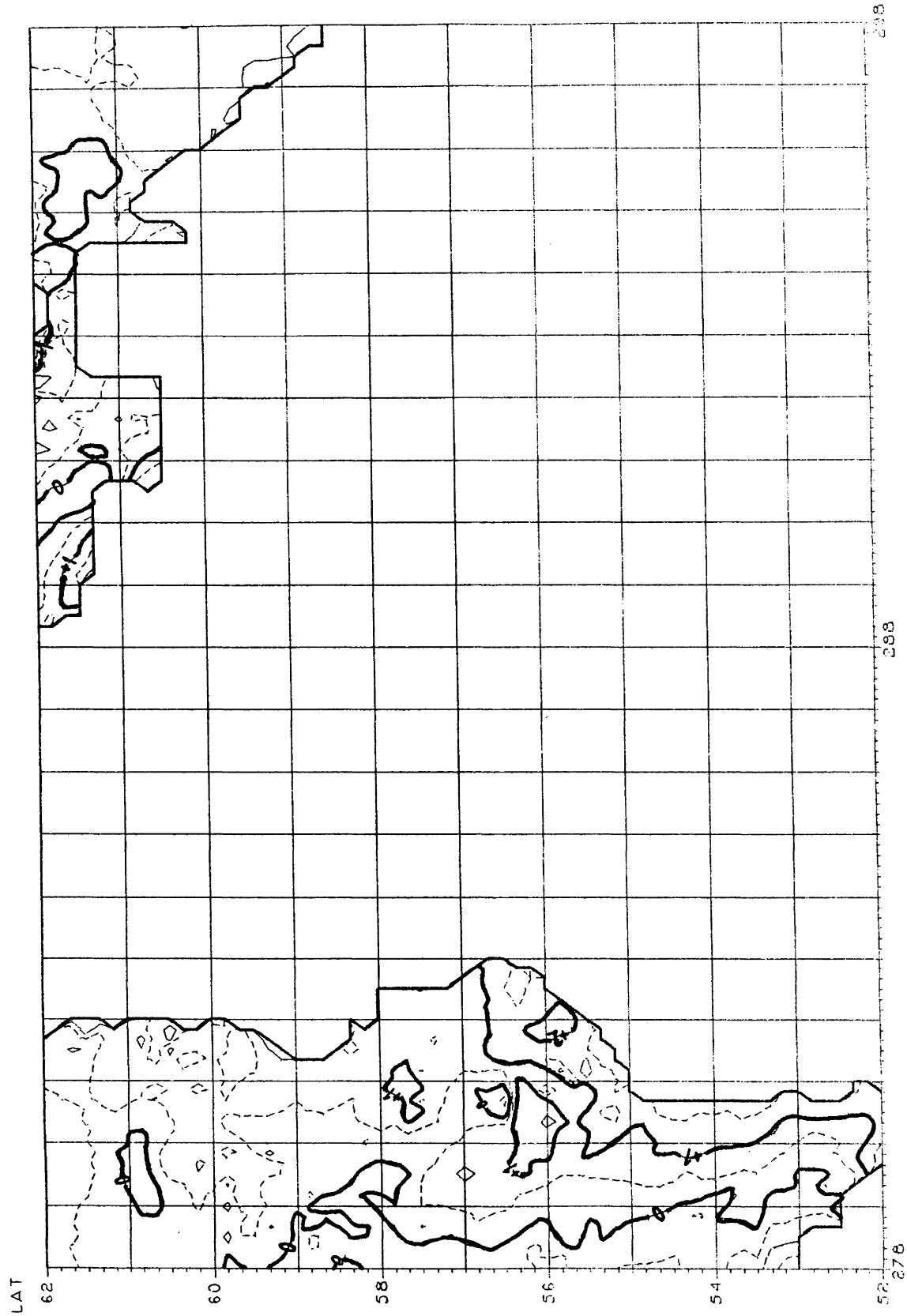

Figure 3.29: UNB geoid minus altimetry.

SAS

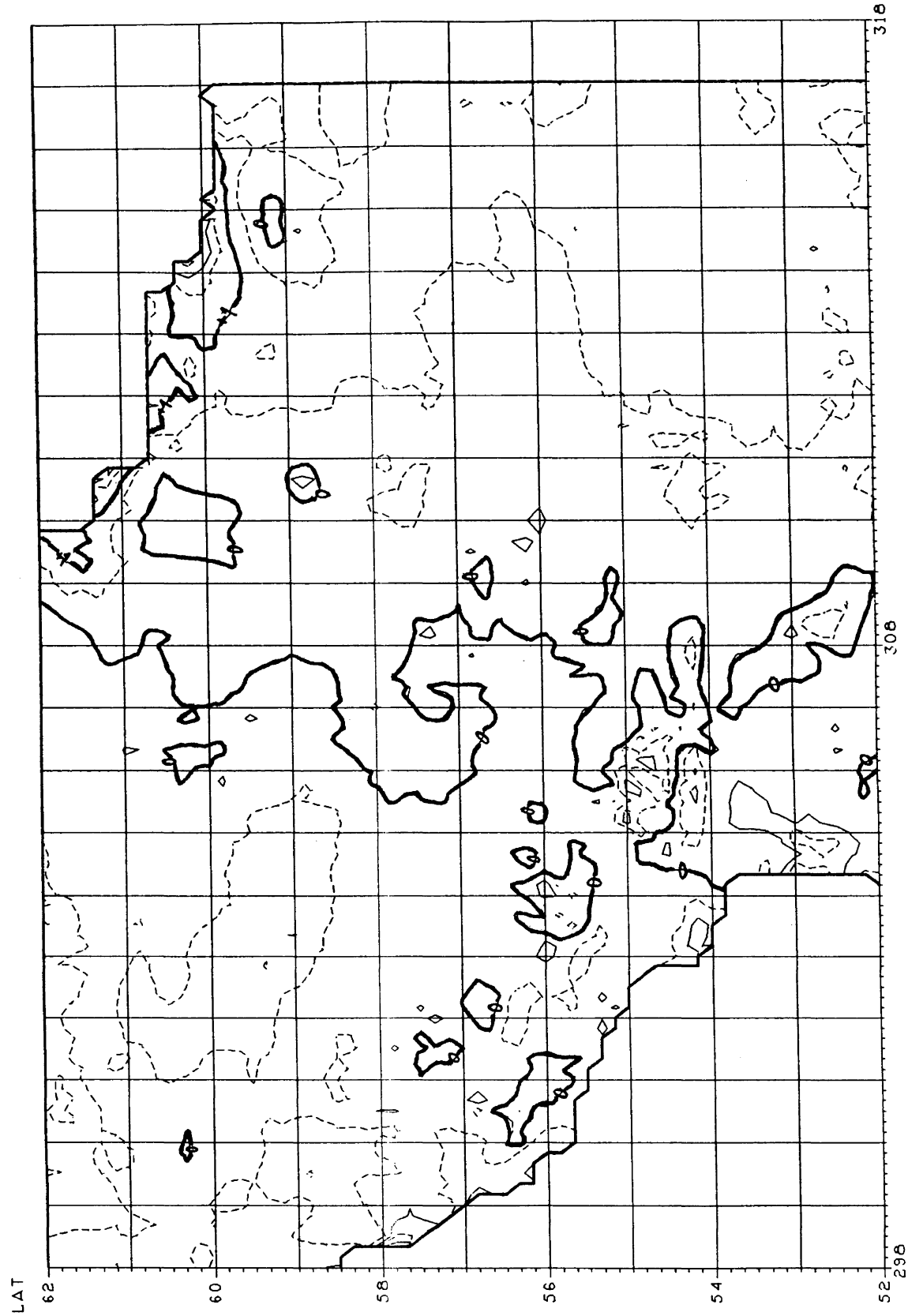

Figure 3.30: UNB geoid minus altimetry.

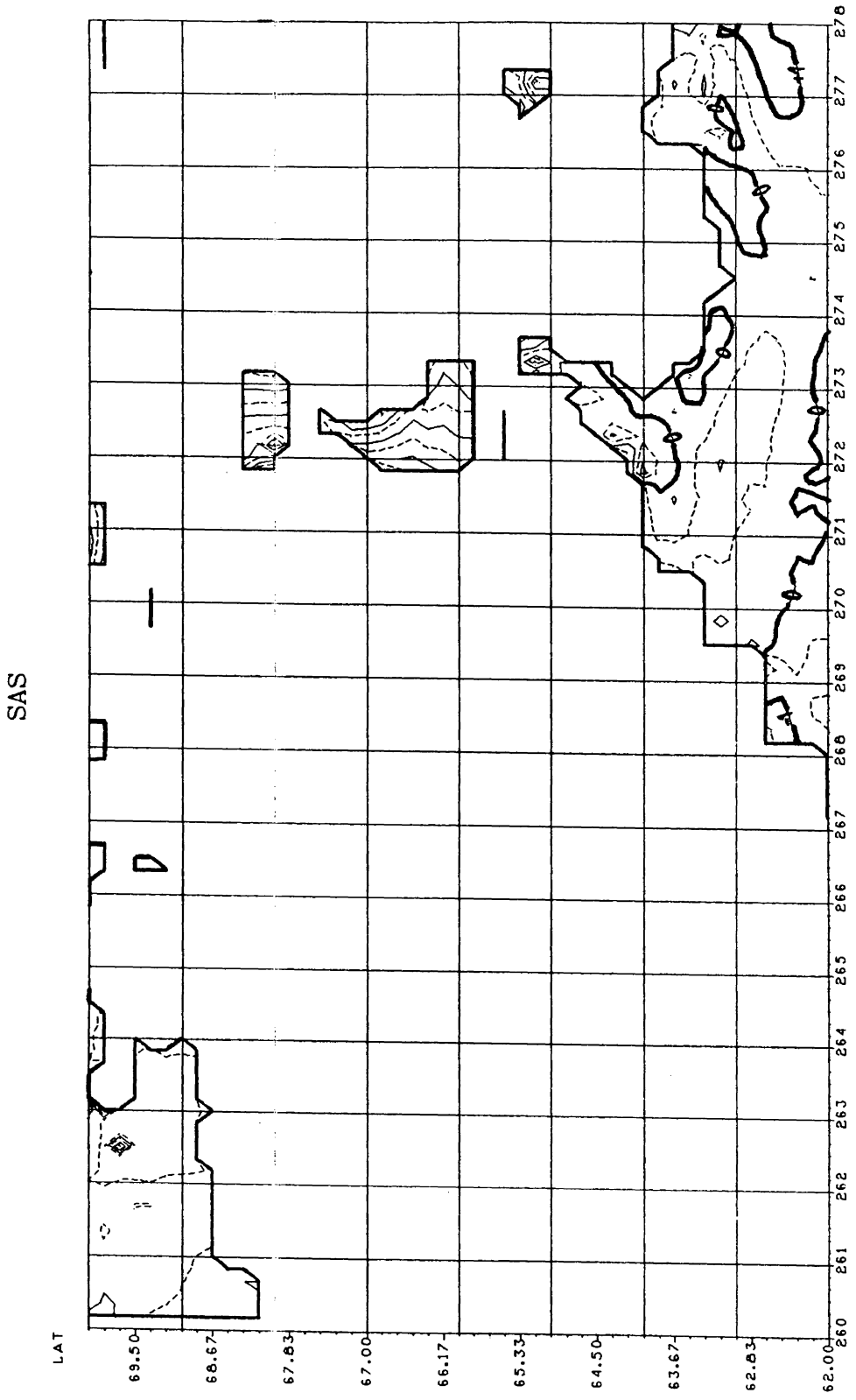

Figure 3.31: UNB geoid minus altimetry.

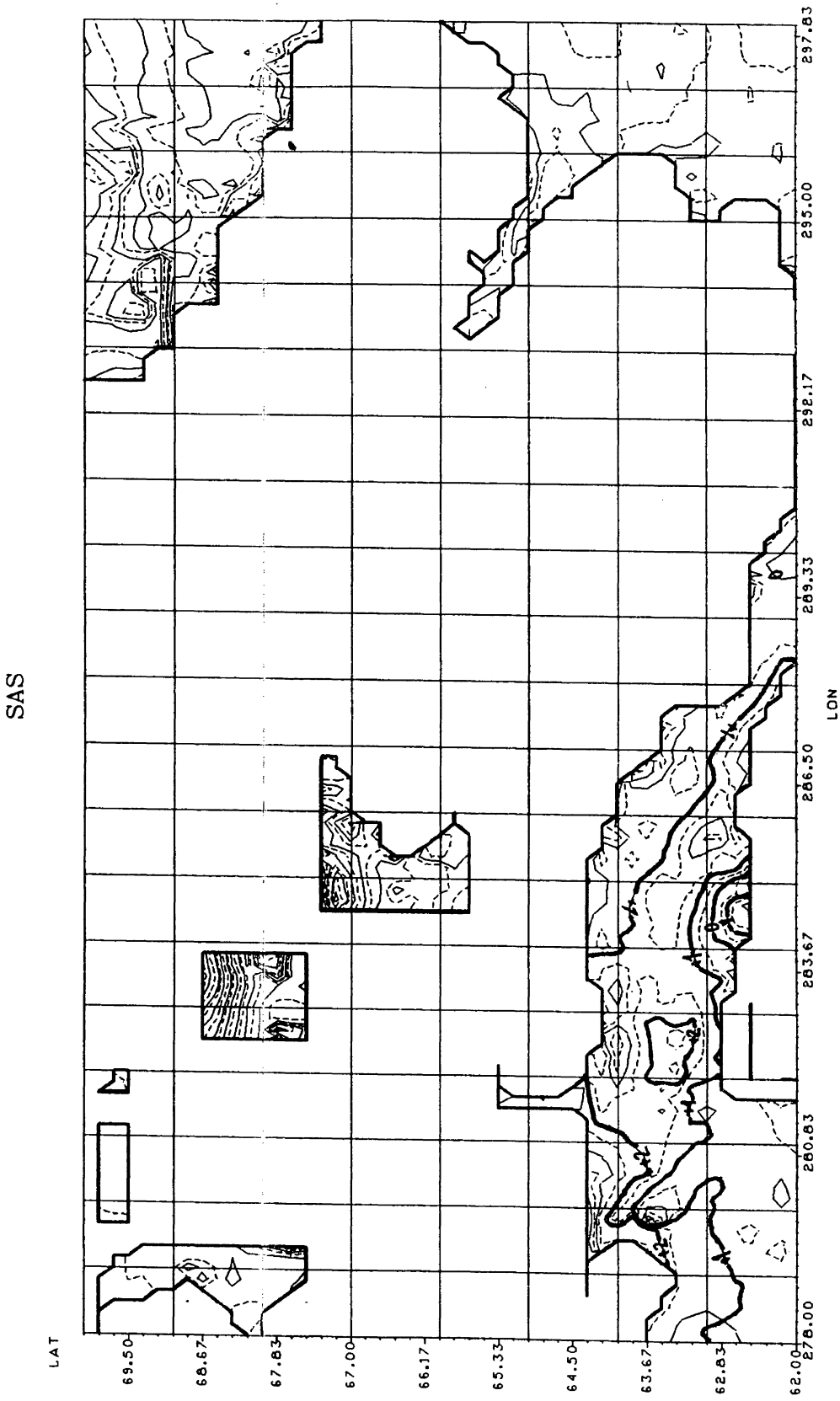

Figure 3.32: UNB geoid minus altimetry.

The surprisingly good agreement between the UNB geoid and the OSU altimetry is characterized by a mean value of μ = -0.19 m for 13 055 geoid differences. The RMS of the differences is 0.65 m, and the RMS with respect to μ is 0.62 m.

4. OTHER SOURCES OF INFORMATION

4.1 Astrogeodetic Deflections of the Vertical

4.1.1 Theory

The astrogeodetic deflection components ξ and η can be obtained directly from the equations

$$\begin{aligned} \xi &= \Phi - \phi \\ \eta &= (\Lambda - \lambda)\cos\phi\,, \end{aligned} \tag{4.1}$$

where $(\Phi,\ \Lambda)$ are the astronomical latitude and longitude, $(\phi,\ \lambda)$ are the geodetic latitude and longitude, if the reference ellipsoid is alligned with the conventional terrestrial (CT) coordinate system.

The shape of the geoid can be determined if the deflections of the vertical are given. The basic equation (astrogeodetic levelling) is due to Helmert [Heiskanen and Mortiz, 1967, p. 197]:

$$N_i = N_{i-1} - \int_{i-1}^{i} (\xi\cos\alpha + \eta\sin\alpha)\, ds\,, \tag{4.2}$$

where α is the geodetic azimuth of the line s connecting the two points P_{i-1} and P_i. The accuracy of this kind of geoid is obviously a function of the spacing and distribution of astronomic observations and the length of the profile.

The least-squares surface fitting technique also can be used to determine the geoid from a given set of deflections. It has been shown [Vaníček and Merry, 1973] that it is preferable to estimate geoidal height variations in a local manner through a two-dimensional approach. In such a two-dimensional approach, the geoidal height N is expressed as a function of position x, y, where the coordinates x, y are taken in a local

Cartesian system defined by, e.g., [Vaníček and Krakiwsky, 1982, p. 533]:

$$x = R(\phi - \phi_0)$$
$$y = R \cos\phi_0(\lambda - \lambda_0) , \qquad (4.3)$$

where (ϕ, λ) are the geodetic latitude and longitude of the point, (ϕ_0, λ_0) are the coordinates of an arbitrary origin, and R is a mean radius of curvature of the earth. Then, the geoidal height $N(x, y)$ at a point (x, y) may be approximated by an algebraic polynomial [Vaníček and Merry, 1973, p. 262]:

$$N(x, y) = P_n(x, y) = \sum_{i,y=0}^{n} c_{ij} x^i y^j , \qquad (4.4)$$

where c_{ij} are obtained by minimizing the sum of weighted squares of $\partial N / \partial x - \xi$, $\partial N / \partial y - \eta$. Here, ξ and η are astrogeodetic deflections which are assumed to have been reduced to the geoidal surface already.

4.1.2 Data and their Accuracy

The astrogeodetic deflection file consists of 937 deflection records in Canada (Figure 4.1). These data were supplied by the Geodetic Survey of Canada [Delikaraoglou, 1985a], and refer to the GRS80 datum. Each record contains:

- latitude (in degrees and decimals of a degree)
- longitude (east, in degrees and decimals of a degree)
- the meridian component ξ of the deflection of the vertical (in seconds of arc, and decimals of a second of arc)
- the prime vertical component η of the deflection of the vertical (in seconds of arc and decimals of a second of arc)
- the total deflection of the vertical (in seconds of arc and decimals of a second of arc)

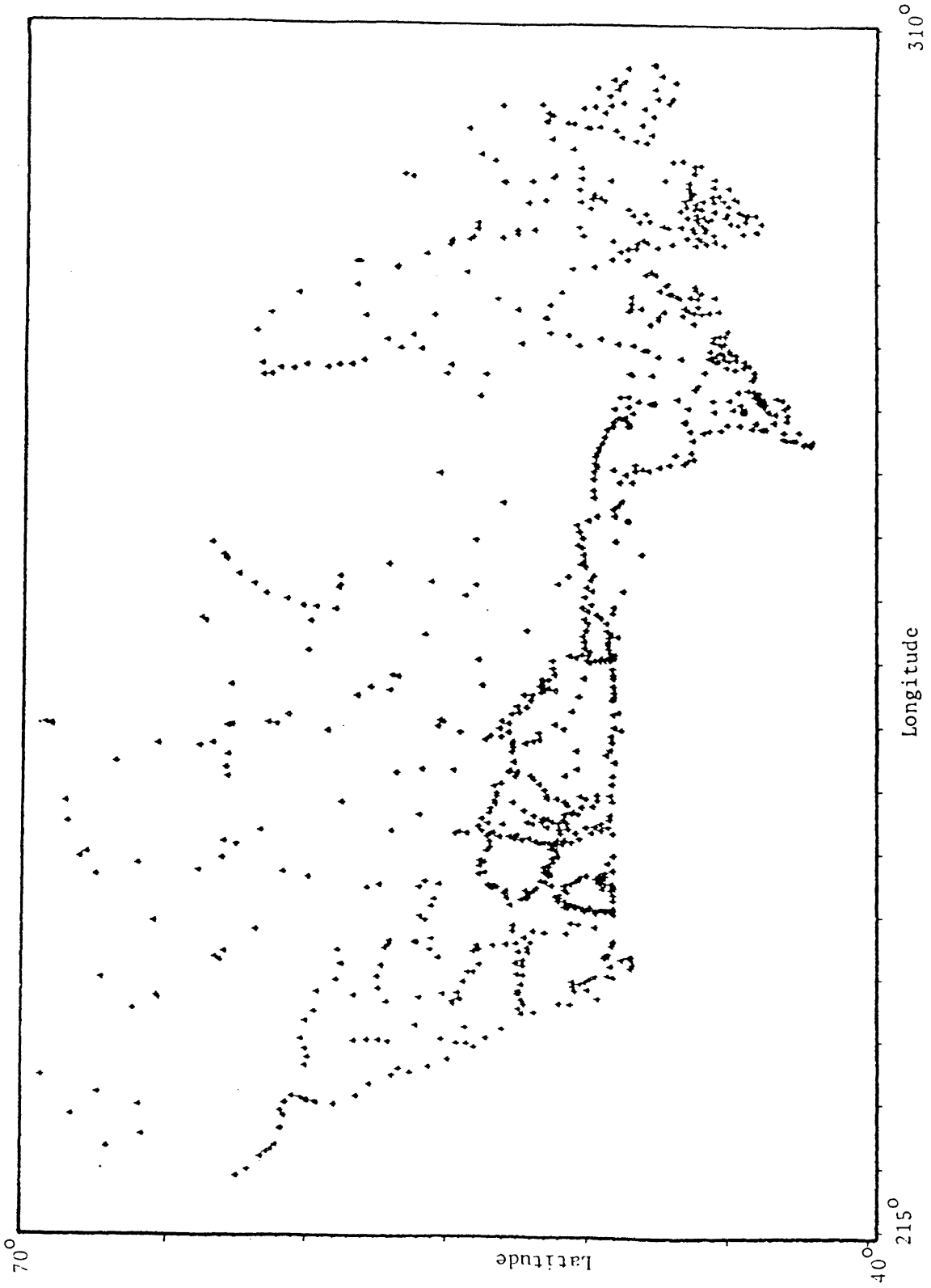

Figure 4.1: Astrogeodetic Deflections of the Vertical

- orthometric height (in metres and decimals of a metre).

The heights of these deflections are obtained from 5' by 5' mean gravity anomaly data files. Heights are needed to account for the curvature of the plumbline—see below.

To derive the standard deviation of ξ and η, it is customary to account for errors only in the astronomical observations and in the computations of geodetic coordinates. In eqn. (4.2), the deflection components ξ and η are supposed to refer to the geoid. This means that the astronomical observations of Φ and Λ must be reduced downward to the geoid in order to make the astronomical and geodetic quantities comparable. But the astronomical coordinates Φ and Λ are not rigorously equal to their corresponding values at the geoid because the plumbline is not straight or, in other words, because the level surfaces are not parallel. This is mainly due to topographic irregularities and crustal density variation [Vaníček and Krakiwsky, 1982, pp. 499-504, 529]. Therefore, there is another source of error arising from the neglect of the curvature of the plumbline.

As a result, if $\sigma^2_{\xi,\eta}$ is the variance that does not account for the curvature of the plumbline and $(\sigma_{\xi,\eta})^2_C$ is the variance due to the curvature, then the total variance $(\sigma_{\xi,\eta})^2_A$ is given by

$$(\sigma_{\xi,\eta})^2_A = \sigma^2_{\xi,\eta} + (\sigma_{\xi,\eta})^2_C \,. \tag{4.5}$$

Taking $(\sigma_{\xi,\eta})^2_C = 1'' \cdot H^2$ [Vaníček and Krakiwsky, 1982], where H is the elevation of the astrogeodetic station in kilometres, and taking $\sigma_{\xi,\eta} = 0.2''$ [Delikaraoglou, 1985b], we obtain

$$(\sigma_{\xi,\eta})_A = 0.2'' \sqrt{1+25 \cdot H^2} \,. \tag{4.6}$$

From this equation we can compute the values of $(\sigma_{\xi,\eta})_A$ using the given H (Figure 4.2).

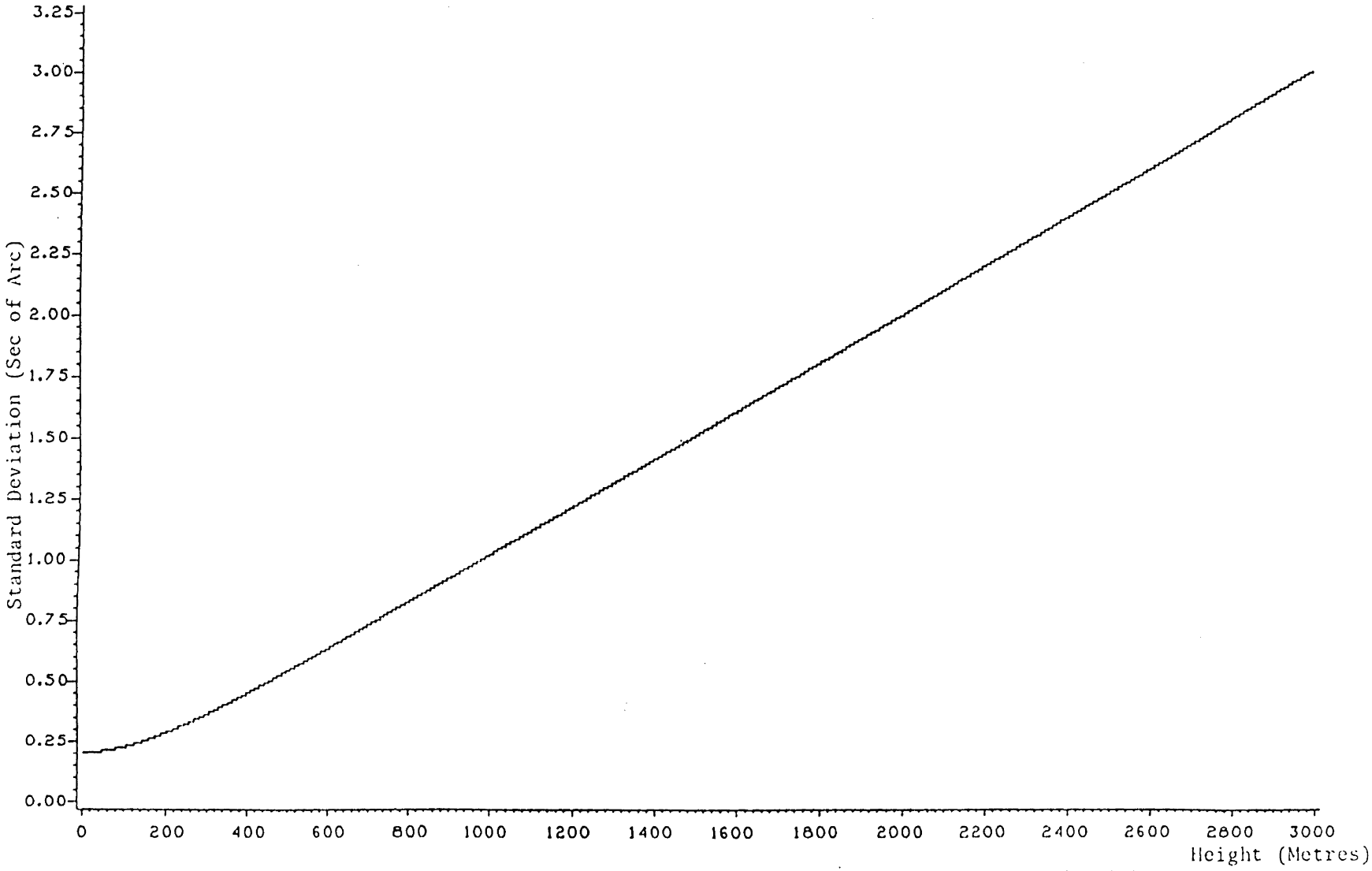

Figure 4.2: Standard Deviation of the Deflection of the Vertical as a Function of Height

4.1.3 Geoid Computation

For small deflections, the following equations are valid [Vaníček and Merry, 1973, pp. 263-268]:

$$P_{nx}(x_k, y_k) = \frac{\partial P_n(x_k, y_k)}{\partial x_k} = \frac{\partial N_k}{\partial x_k} = -\tan\xi_k \doteq -\xi_k$$

$$P_{ny}(x_k, y_k) = \frac{\partial P_n(x_k, y_k)}{\partial y_k} = \frac{\partial N_k}{\partial y_k} = -\tan\eta_k \doteq -\eta_k \,. \tag{4.7}$$

Then the following expressions should be minimized:

$$\rho_x^2 = \sum_k W_\xi [P_{nx}(x_k, y_k) + \xi_k]^2$$

$$\rho_y^2 = \sum_k W_\eta [P_{ny}(x_k, y_k) + \eta_k]^2 \,, \tag{4.8}$$

where W_ξ, W_η are computed as an inverse of the corresponding variances.

Using the matrix notation to represent the observation equations, we get:

$$\boldsymbol{A}\boldsymbol{c} = \boldsymbol{u} \,, \tag{4.9}$$

where the elements of matrix $\boldsymbol{A}$ are given by:

$$a_{lm} = i\, r\langle W_\xi\, x^{r+i-2}, y^{s+j}\rangle + j\, s\langle W_\eta\, x^{r+1}, y^{s+j-2}\rangle \,, \tag{4.10}$$

the elements of vector $\boldsymbol{c}$ are the unknown coefficients c_{rs}, and vector $\boldsymbol{u}$ consists of:

$$u_l = -i\langle W_\xi\, \xi, x^{i-1}\, y^j\rangle - j\langle W_\eta\, \eta, x^i\, y^{i-1}\rangle \,, \tag{4.11}$$

for

$i, j, r, s = 0,\ldots,n;$
$i + j \neq 0;$
$r + s \neq 0;$
$l = i + j + ni.$

Denoting by $\boldsymbol{W}$ the common weight matrix of the two deflection component vectors ξ, η, the unknown coefficients $\hat{c}_{rs}$ are then obtained from:

$$\hat{\boldsymbol{c}} = (\boldsymbol{A}^T\boldsymbol{W}\boldsymbol{A})^{-1}\,\boldsymbol{A}^T\boldsymbol{W}\boldsymbol{u} \,. \tag{4.12}$$

and their covaraince matrix is

$$\hat{\boldsymbol{C}}_{\hat{c}} = \hat{\sigma}_0^2 (\boldsymbol{A}^T \boldsymbol{W} \boldsymbol{A})^{-1} . \tag{4.13}$$

Finally, we can derive the covariance matrix, $\boldsymbol{C}_{\hat{N}}$ for any vector of q estimated geoidal heights, $\hat{\boldsymbol{N}}$. Since each $\hat{N}(x_i, y_i) = P_n(x_i, y_i)$ is a linear combination of the coefficients c_{ij}, then

$$\hat{\boldsymbol{N}} = \boldsymbol{B}\, \hat{\boldsymbol{c}} , \tag{4.14}$$

where $\boldsymbol{B}$ is a q by $((n+1)^2-1)$ matrix of mixed algebraic functions. Then the covariance matrix is given by:

$$\hat{\boldsymbol{C}}_{\hat{N}} = \boldsymbol{B}\, \hat{\boldsymbol{C}}_{\hat{c}}\, \boldsymbol{B}^T . \tag{4.15}$$

4.2 Satellite Altimetry

4.2.1 Theory

Satellite altimetry techniques for observing the ocean surface topography have been one of the fundamental tools of the NASA Ocean Processes Program for more than 15 years [Tapley et al., 1982]. Currently, two major satellite altimetry data sets exist. These are from the GEOS-3 mission (1975-1978), and from the SEASAT mission which was operational for three and a half months in 1978. SEASAT and GEOS-3 raw data are available to researchers from NOAA/NESDIS [U.S. NRC, 1985].

The principle behind satellite altimetry measurements of the ocean surface lies in the fact that the satellite serves as a stable platform from which the radar-altimeter measures the distance of the spacecraft above the instantaneous ocean surface, based on the travel time of short-pulse microwave signals. This distance measurement is an average height over the area covered by the radar footprint, the size of which depends

upon the sea state.

The geometry of the altimeter measurement is shown in Figure 4.3 and it relates:

- h the geodetic height of the spacecraft;
- a the measured altitude above the ocean surface;
- N the geoidal height;
- ζ the height of the sea surface above the reference ellipsoid; and
- ζ_S the dynamic sea surface height;

through the expression

$$\zeta_S = \zeta - N = (h - a) - N \,. \tag{4.16}$$

In eqn. (4.16), it is assumed that the altimeter measurement (a) has already been corrected for a number of effects, such as (see Lorell et al. [1980]):

(a) instrument corrections (instrument delays, altimeter off-nadir pointing errors, antenna centre of mass correction, residual biases, etc.);

(b) propagation medium effects (atmospheric path length corrections due to tropospheric dry and wet component delay and ionospheric delay);

(c) geophysical reductions (corrections due to solid earth and ocean tides, inverse barometer response of the ocean, sea state, wind pile up, etc.).

Orbital errors (such as those due to model gravity field, atmospheric drag, solar radiation pressure) are assumed to have already been accounted for in the geodetic height (h) of the spacecraft.

4.2.2 Altimetric Data Description

Three data sets of altimetric sea surface heights have been acquired and are available at UNB. All three data sets come from the SEASAT satellite mission between 28 June and 10 October 1978, with a little contribution from GEOS-3 in the case of the NASA 2 file (see below). The following conventions will be used to refer to these data sets:

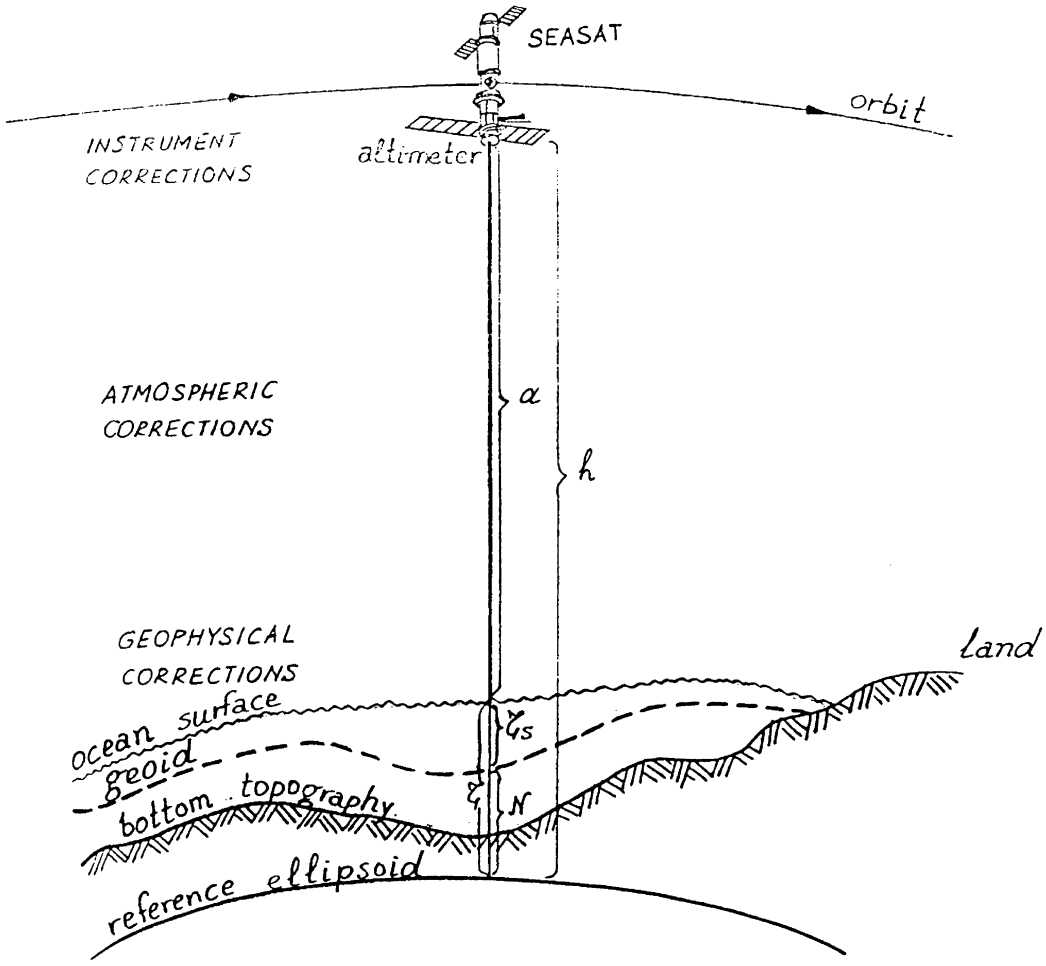

Figure 4.3: Geometry of Altimeter measurements

GSFC-NASA 1: A regional data set of adjusted sea surface height (ASSH) profiles covering the area $35^{\circ}N \leq \phi \leq 72^{\circ}N$ and $260^{\circ}E < \lambda \leq 350^{\circ}E$ in the form of diamond shaped subsets.

GSFC-NASA 2: A global gridded data set of sea surface heights based on a combination of GEOS-3 and SEASAT data. The grid spacing is 1/8 of a degree.

OSU: A regional data set of adjusted sea surface height (ASSH) profiles covering the area $35^{\circ}N \leq \phi 72^{\circ}N$ and $260^{\circ}E \leq \lambda \leq 350^{\circ}E$.

The first two data sets were made available to us by J. Marsh, of Goddard Space Flight Center (GSFC-NASA), and the third by R. Rapp of The Ohio State University (OSU).

The regional data sets came in the form of adjusted altimetry profiles (tracks). The procedures used to produce these results are described in the publications by Marsh et al. [1984], Rapp [1982a], Rapp [1982b], and Rowlands [1981].

Both regional data sets have been gridded using an interpolation procedure described in Yazdani et al. [1985] on a 10' by 10' grid. All three gridded altimetry data files contain the grid coordinates and the ASSH. The two regional grids (GSFC-NASA 1 and OSU) also contain information on the standard deviations of the grid (interpolated) values. The grid points where the interpolation scheme failed to provide results are given default values. All three data sets contain ASSH referred to the GRS80.

The oceanographic signal (i.e., sea surface topography (SST)) is part of the ASSH. Currently, there is work being done to extract this signal from the gridded altimetry data using an independent (oceanographic) estimate of SST from the Levitus dynamic topography determination [Levitus, 1980].

All three gridded altimetry data sets are available on tape upon request.

4.2.3 Accuracy of the Altimetry Files

The accuracy assessment of the GSFC-NASA 1 adjusted sea surface heights is given in Marsh et al. [1984]. The standard deviations associated with the gridded GSFC-NASA 1 data set were computed during the interpolation procedure, and they reflect the distribution and density of the input ASSHs. Since a formal error estimate of the individual adjusted altimetry data points was not available on the acquired tape, a standard deviation of 15 cm was assigned to all points. This was based on the RMS value of the discrepancies after the crossover adjustment over the diamond-shaped areas, which was of the order of 10 cm [Marsh, 1985]. There is no accuracy assessment of the GSFC-NASA 2 file available to us at the moment.

The OSU tape with the adjusted sea surface heights included information about the standard deviations of the individual data points. However, a cut-off value of 25 cm has been enforced for these standard deviations: if the estimated standard deviation of the data points after the crossover adjustment procedure was in excess of 25 cm, then it was set to 25 cm. More information about the accuracy of this data set can be found in Engelis [1983], Rapp [1982a], Rapp [1982b], and Rowlands [1981]. The standard deviations contained in the gridded data set were based on the input file standard deviations; they also reflect the data density and distribution of the input values.

5. THE COMBINED GEOID

5.1 Theoretical Considerations

5.1.1 Algebraic Surface Representation of the Geoid

It is clearly very desirable to utilize all the available kinds of data in the construction of the final geoid. An investment has been made in collecting those data, and the mere fact that we may not readily know how to include these data rigorously should not detract us from the goal of utilizing them.

The only way we know how to combine the different kinds of data is through designing a model for the geoid and using the different data to improve the estimation of the model parameters. This is the way our original computations [Vaníček and Merry, 1973; Vaníček and John, 1983] were conducted. There, the geoid was modelled by a simple two-dimensional algebraic surface and the coefficients estimated, using the least-squares approach, from both the point geoidal heights (e.g., N_G and N_D values) and point slopes (the deflections).

Alternatives do exist. One such alternative—using scaled spherical harmonic functions—was tested by Najafi [1981]. His model, however, was not shown to be superior to the simple algebraic surface.

The mathematics of the two-dimensional algebraic surface and the data combination have been formulated by Merry [1975]. In brief, the geoid is modelled by eqn. (4.4), where the coefficients $c_{ij} \in \boldsymbol{c}$ are to be estimated. The part that is estimated from the deflections of the vertical is given by eqn. (4.12). When point values of N are also available, another set of normal equations is assembled:

$$A_N^T P A_N \hat{c} = A_N^T P N \,, \tag{5.1}$$

where A_N^T is the Vandermonde (design) matrix [Vaníček and Krakiwsky, 1982, p. 26] containing functional values of the kind of $x^m y^n$, N is the vector of point values of N, and P is its weight matrix.

To obtain the best estimate of c from the combination of both types of data, the two sets of normal equations are added together yielding

$$(A^T W A + A_N^T P A_N)\,\hat{c} = A^T W u + A_N^T P N \,, \tag{5.2}$$

and, eventually, the solution $\hat{c}$. The covariance matrix of these coefficients c is given by

$$\hat{C}_{\hat{c}} = \hat{\sigma}_0^2 (A^T W A + A_N^T P A_N)^{-1} \tag{5.3}$$

and the covariance matrix $\hat{C}_{\hat{N}}$ of a predicted vector $\hat{N}$ of geoidal heights is computed from eqn. (4.15).

Program ASROG has been developed (based on Merry's program CONGA2) to implement the above modelling. It produces $(n+1)^2$ estimated coefficients—for an n*th* degree algebraic surface—and predicts $\hat{N}$ on a selected regular grid of points. Input data can be read in either a grid form or individually.

5.1.2 Selection of Mesh Size for Point Input

Focusing on the point input data in a grid form (such as N_G), the question arises as to what size of mesh should be utilized. Different mesh size will produce different algebraic surfaces.

Naturally, the best solution would be obtained from a continuous coverage, i.e., if the mesh size were infinitesimally small. Under these circumstances, the scalar

products that make up the matrices of normal equations (5.2) would be taken in the integral (compact) sense [Vaníček and Krakiwsky, 1982, p. 35] rather than in the discrete sense.

This ideal cannot be achieved, but the mesh size can be made as small as practicable. If it is sufficiently small, then the summation may be regarded as a numerical version of the integration, and the solution will approximate the ideal solution to the same extent that the numerical integration approximates the analytical integration.

Here, we have decided to select the mesh size of 20', twice as coarse as the mesh of the gravimetric solution but fine enough to show most of the detailed geoid structure. With this mesh size, the sums used in constructing the normal equation can be viewed as good approximations of integrals.

5.2 Results

5.2.1 Algebraic Surface Representation of the Gravimetric Geoid

To test just how well the gravimetric solution can be approximated by an algebraic surface, we have taken the rectangle covering the Maritimes and southern Ontario, i.e., $\phi \in \langle 42^\circ, 52^\circ \rangle$, $\lambda \in \langle 278^\circ, 298^\circ \rangle \equiv A_1$ —cf. Figure 3.12. We have selected the highest practical degree of the surface, $n = 9$, which needs 100 coefficients. Figure 5.1 shows the differences between the input (on a 20' by 20' grid) N_G and the predicted N given by the surface. The differences are quite large, reaching more than 3 metres in the positive sense and over 2 metres in the negative sense. Viewed from the point of view of the local accuracy of N_G, which is of the order of only a few decimetres at worst, such differences are unacceptable. Clearly, the algebraic surface

is too 'stiff' to approximate the N_G correctly in the region of strong local variations.

To see how the approximation works in an area of flatter geoidal relief, we have selected another rectangle: $\phi \in \langle 62^\circ, 72^\circ \rangle$, $\lambda \in \langle 258^\circ, 278^\circ \rangle \equiv A_2$ —cf. Figure 3.21. The differences (Figure 5.2, not available as yet) are now much smaller, having a range of about 2 metres and an RMS of about 20 cm. We may conclude that the algebraic surface can be made adequately flexible in this region, but that is of little consolation as far as the other parts of Canada go.

5.2.2 Effect of the Deflections of the Vertical

Next, we tested the procedure for including the deflections of the vertical in the area A_1. For the combination, the deflection components were given standard deviations defined by eqn. (4.6). The standard deviations of the gravimetric geoidal heights were computed as

$$\sigma_{N_G} = \sqrt{1.33^2\ \mathrm{m}^2 + \sigma^2_{\delta N}}\ , \tag{5.4}$$

where 1.33 m is the value determined in section 3.2.1, and $\sigma_{\delta N}$ is the standard deviation of the high frequency contribution.

The differences N_G - $\hat{N}$ are plotted on Figure 5.3. The range of these differences is more than 15 metres and clearly unacceptable. The explanation for this lies probably in the fact that the selected σ_{N_G} is far too high, the 1.33 m referring only to the long wavelength contribution. Hence, the 239 existing deflections swamp the solution. In the area A_2, where there are only 57 deflections, their effect is much less pronounced, the range being 2.5 m and RMS = 0.23 m—see Figure 5.4.

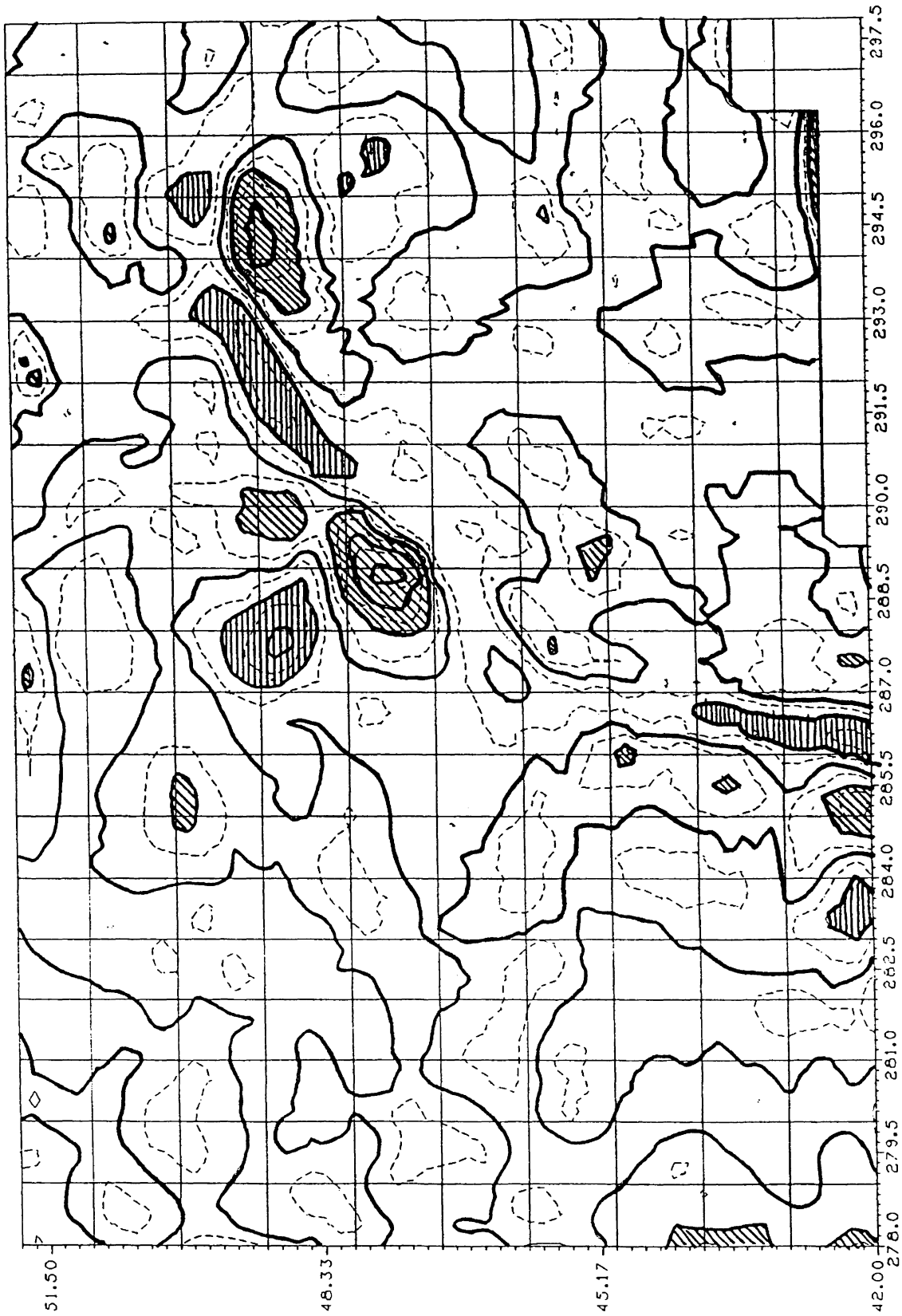

Figure 5.1: Surface fit to N_G

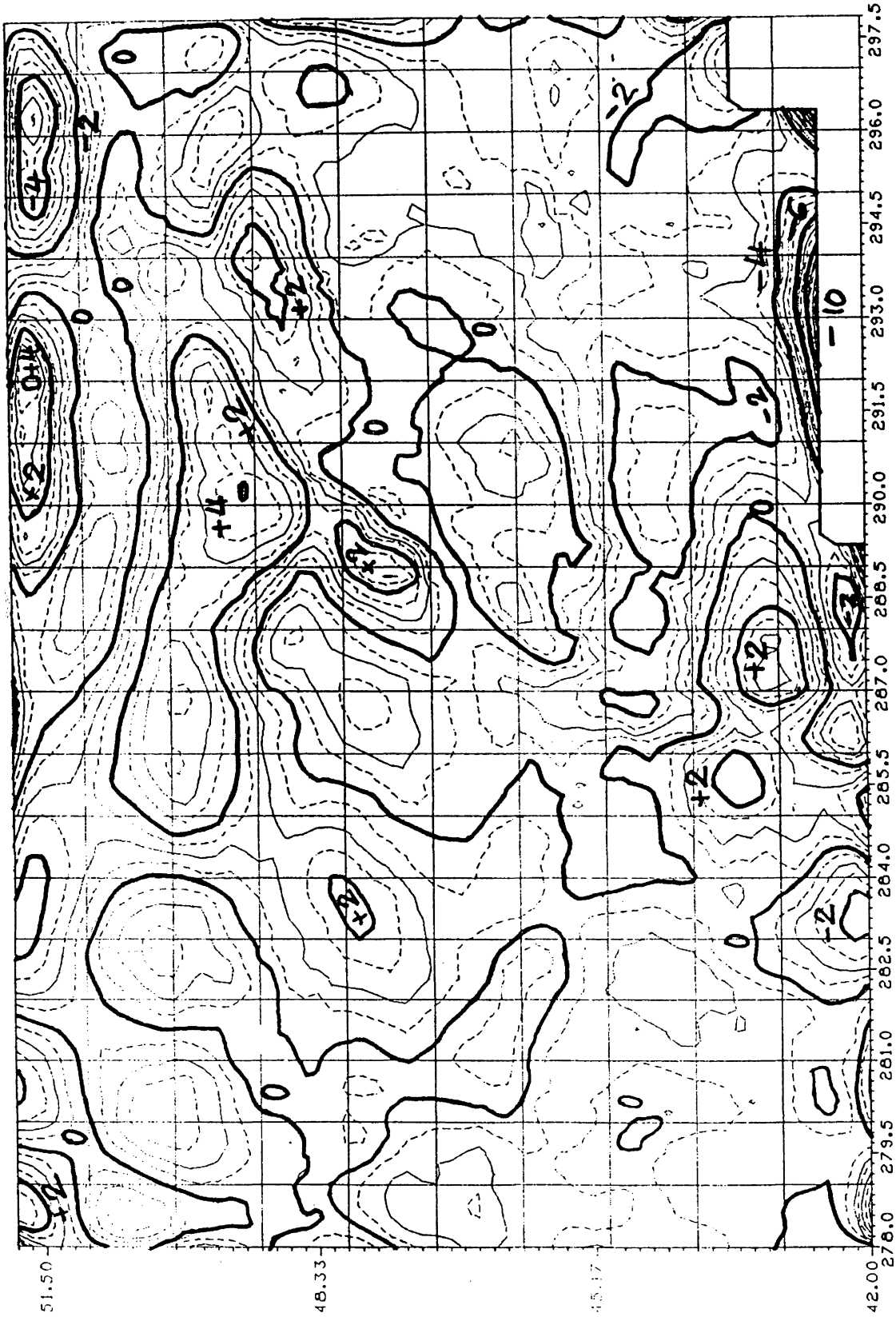

Figure 5.3: Fit to N_G and the deflections

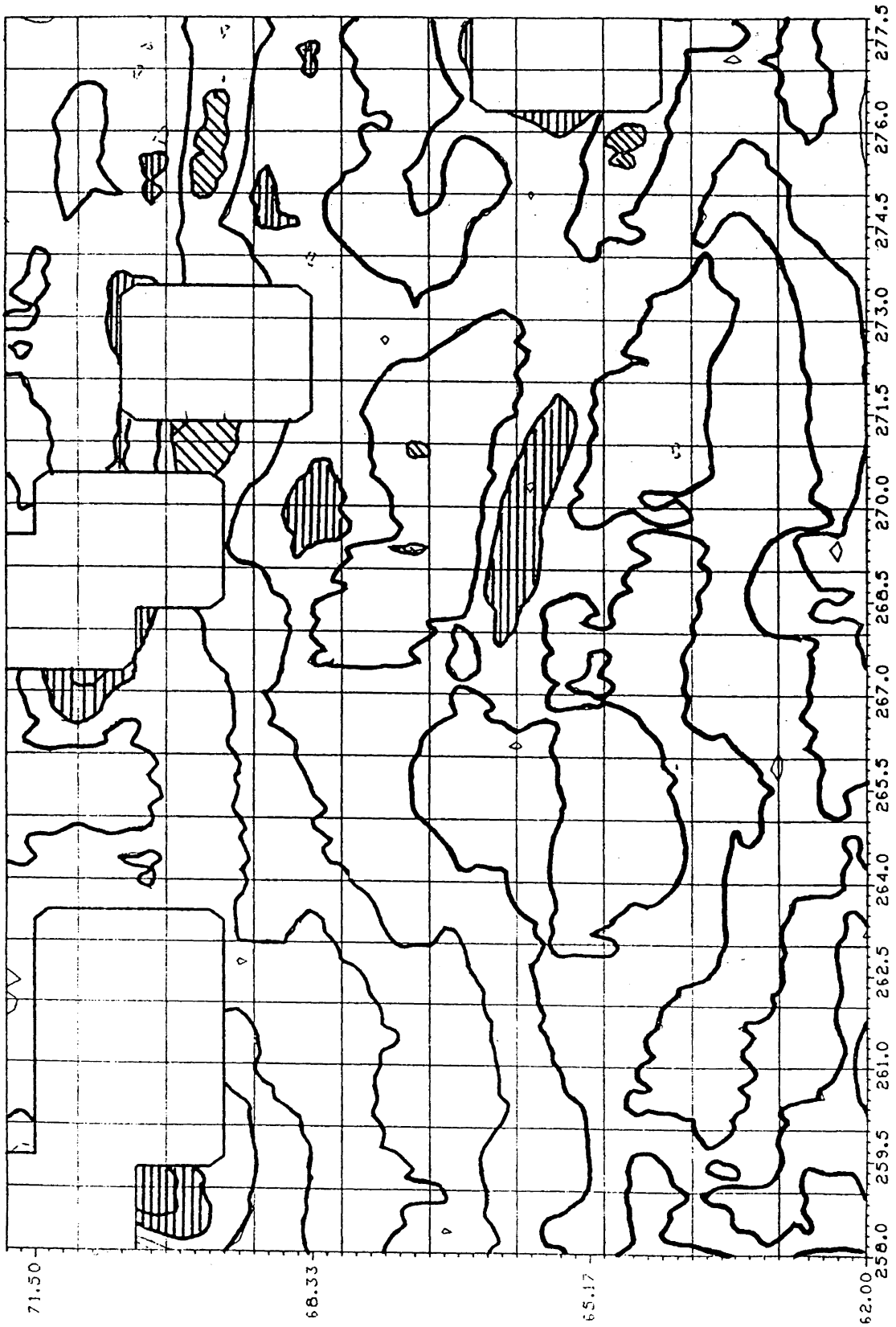

Figure 5.4: Surface fit to N_G and the Deflections

To test the hypothesis that it is the σ_{N_G} which is responsible for the large differences, we have re-run the approximation for A_1 taking $\sigma_{N_G} = \sigma_{\delta N}$. The results—see Figure 5.5—appear to vindicate the hypothesis, with the range coming down to 5.49 m and RMS to 0.52 m.

5.2.3 Effect of the Doppler Derived N

The contribution of the Doppler derived N_D has been tested in area A_2 which contains 9 points with N_D. The standard deviation assumed for N_D was 1.25 m, and σ_{N_G} given by eqn. (5.4). The differences, displayed on Figure 5.6, are not entirely unreasonable, with an RMS of 22 cm and range of about 1.5 metres. Very probably, though, the N_G is underweighted for the same reason as above and does not deserve to be distorted even this much. As we have seen in section 3.2, the Doppler derived N_D are not very reliable.

5.2.4 Effect of the Altimetry

Finally, the effect of the altimetry was tested in the area A_1, see Figure 5.7. Even though the differences between altimetry and N_G are small—see section 3.3.3—the straightforward inclusion of altimetry introduces violent oscillations in the solution. The range goes up to about 12 metres and the RMS is 1.14 m. Clearly, the discontinuity along the coastline has to be treated in a more sophisticated way. Another problem for the future.

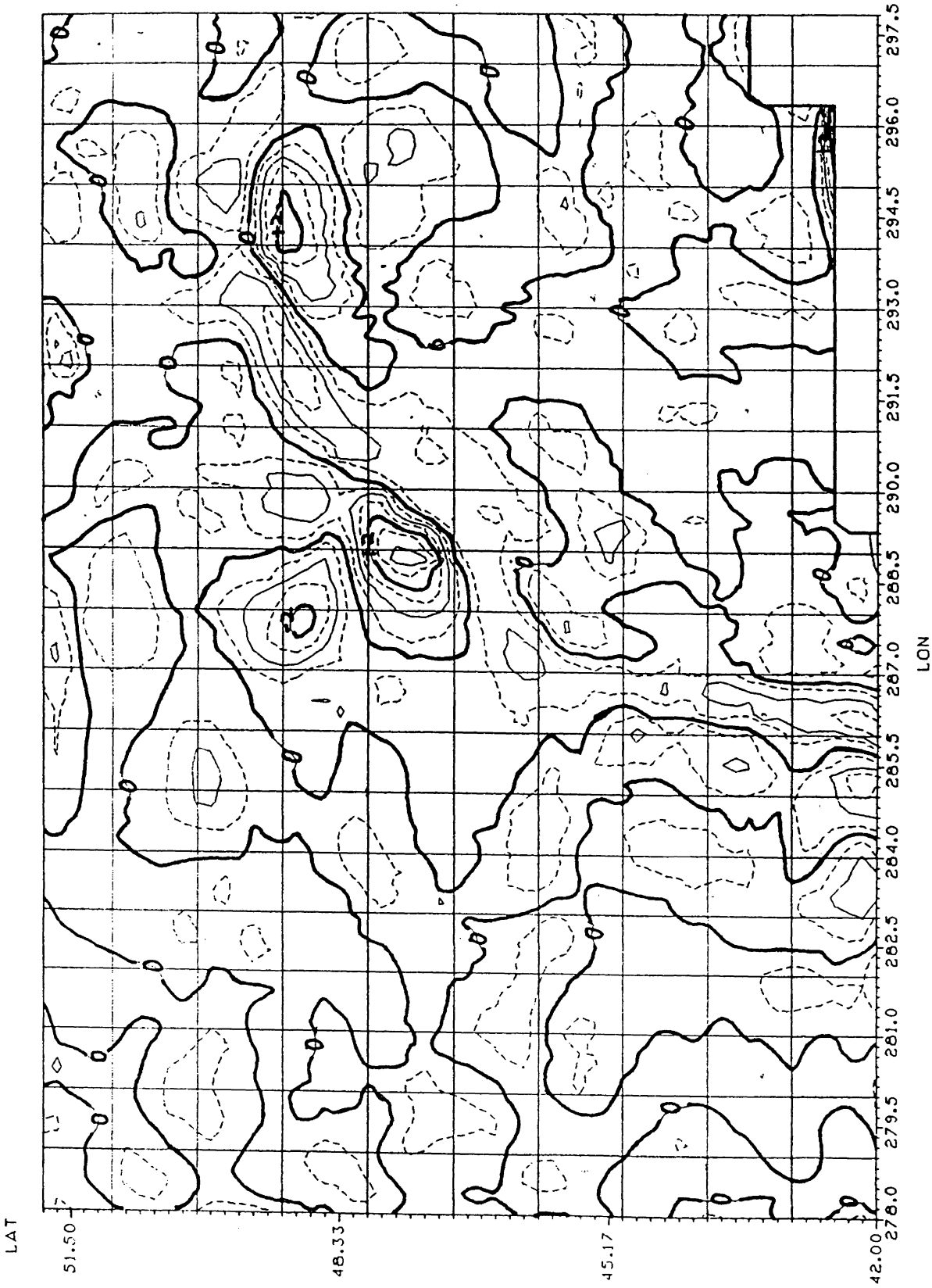

Figure 5.5: Fit to N_G and the deflections

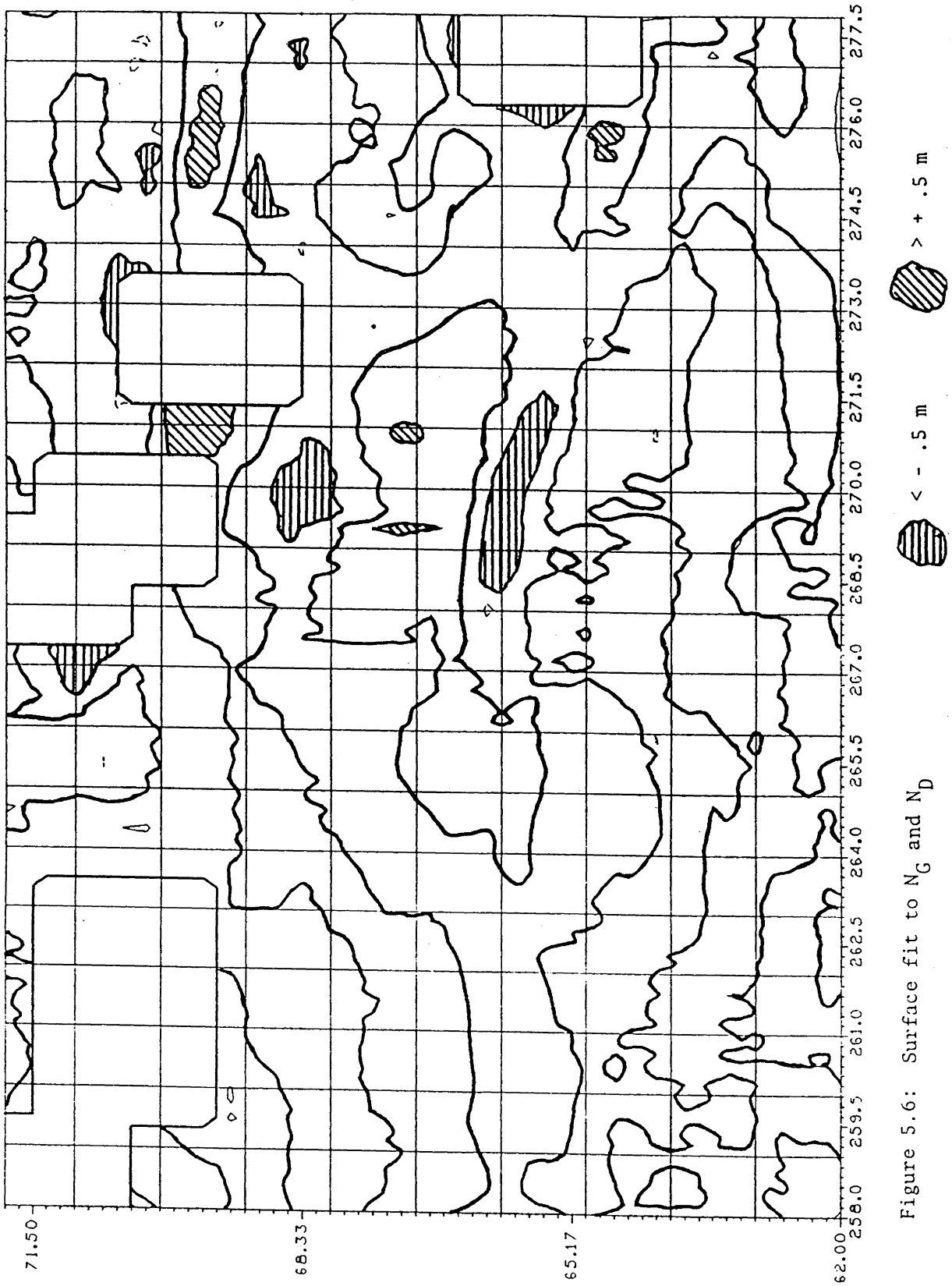

Figure 5.6: Surface fit to N_G and N_D

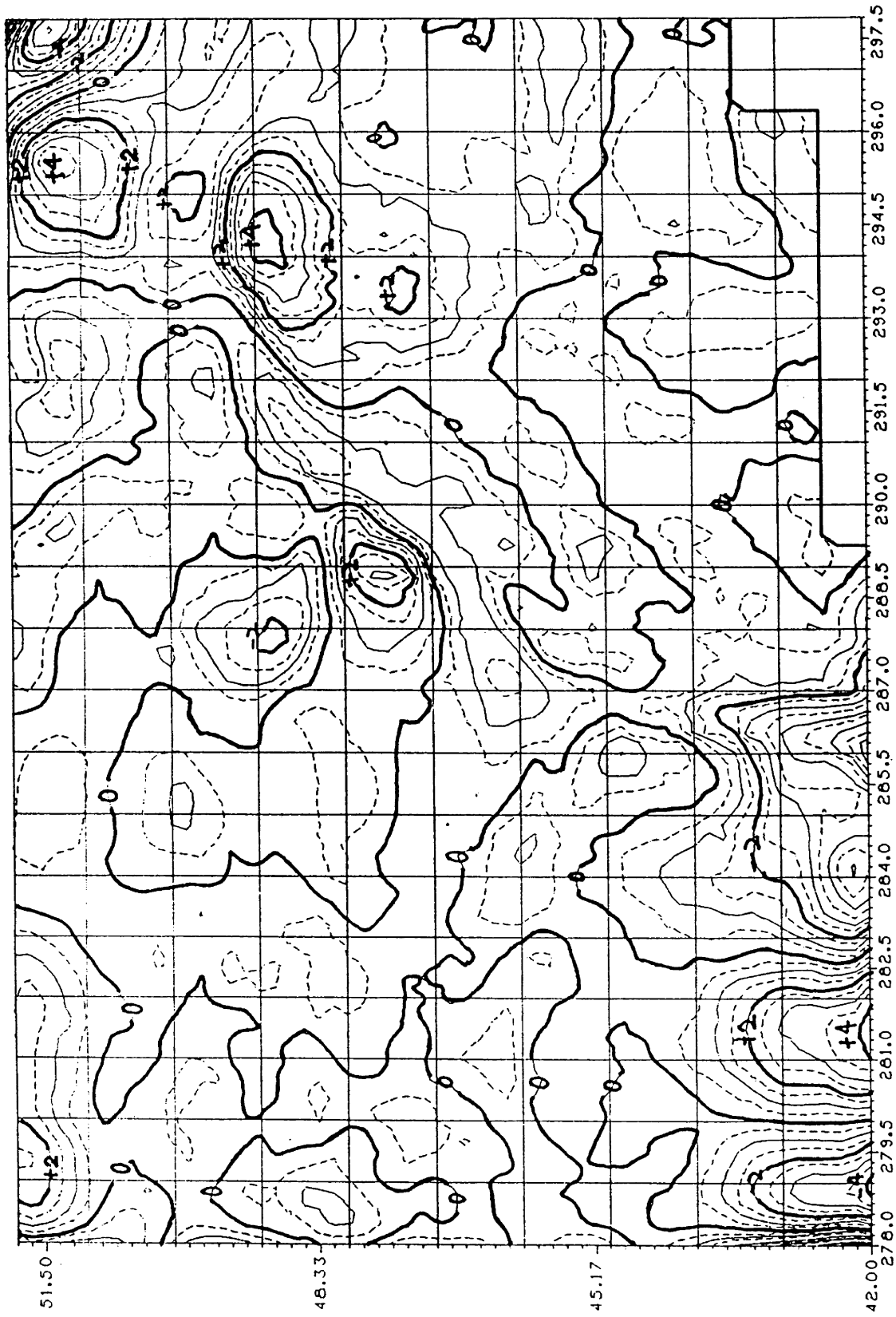

Figure 5.7: Fit to N_G and altimetry

5.3 An Alternative

It appears that the algebraic surface modelling of a detailed geoid is not the way to go. If one wants to keep the number of coefficients to a reasonable level, the surface is too stiff to follow a rugged shape. The price one would have to pay for making the surface sufficiently flexible is to increase the number of coefficients thus making the model much more clumsy.

An alternative solution to the problem of evaluating the contribution of non-gravimetric data that seems to be worth exploring would be as follows:

(a) Construct a system of functions orthogonal in the compact area of interest.

(b) Formulate a system of normal equations for the coefficients $c = c_0 + \delta c$ in such a way that c_0 would be evaluated from gravimetric data and δc from the other data sources following the sequential adjustment technique. (The increment δc is expressed as a linear function of all the non-gravimetric data.)

(c) The increment δc multiplied by the appropriate orthogonal functions represents a corrective surface that can be added to the gravimetric solution N_G in one form or another.

We note that this approach would not require any degradation of the gravimetric solution, which would thus retain all its detail. The deflection and Doppler data would supply only a medium wavelength contribution, while the correction coming from altimetry would have all frequencies depending on the areal coverage included.

6. CONCLUSIONS AND ACKNOWLEDGEMENTS

Building on previous work done at UNB, we have formulated an algorithm for gravimetric geoid determination based on the idea of using a long wavelength spherical harmonic expansion of the gravity potential as a reference spheroid for a spheroidal Stokes's integration.

We chose the GEM9 as the long wavelength spheroid since this earth model is derived from satellite observations only and thus is not correlated with the terrestrial gravity observations.

Experiments with synthetic data determined the optimal truncation radius for the spheroidal Stokes's integration with respect to economy and accuracy. The gravity data used in the integration consisted of point gravity anomalies for the innermost zone ($\psi < 10'$), of 5' by 5' mean gravity anomalies for the inner zone ($\psi < 1^\circ$), and 1° by 1° mean gravity anomalies for the outer zone ($\psi < \psi_0 = 6^\circ$).

Combining the integration result with the long wavelength GEM9 geoid gave the 'UNB gravimetric geoid.' Unexpectedly, it shows in great detail many very localized features which were previously unknown.

The UNB geoid is, on average, some 80 cm below the 'Doppler geoid' (cf. Chapter 3) and some 25 cm above the altimetric sea surface in the Atlantic Ocean and Hudson Bay.

The above mentioned very detailed structure of the UNB gravimetric geoid makes it almost impossible to represent its combination with other data in the form of an algebraic surface. A surface representation would either require a tremendous number of base functions or it would smooth the details in the gravimetric geoid. Clearly, this

cannot be our ultimate goal.

We gratefully acknowledge the financial help from NSERC, in terms of an operating grant to the Principal Investigator, and from the Geodetic Survey of Canada, in terms of a DSS research contract. Our thanks go to the Scientific Authority for the DSS contract, Dr. D. Delikaraoglou, for his help with many aspects of this work.

Prof. R.H. Rapp (OSU), Mr. J. Marsh (GSFC/NASA), Mr. D.B. Hearty and Mr. G. Garrard (both of EMR, Ottawa) have contributed to the success of this investigation through making available to us the various data sets.

Last but by no means least our thanks are due to Ms Wendy Wells for her artistic 'Macintoshing' of this report.

BIBLIOGRAPHY

Abramowitz, M. and I.A. Stegun (1964). *Handbook of Mathematical Functions.* Dover reprint 1965.

Chang, R.G., N. Christou and H. Fashir (1986). "Software for geoid computations." Department of Surveying Engineering Technical Memorandum 10, University of New Brunswick, Fredericton (in preparation).

Delikaraoglou, D. (1985a). Personal communication. Geodetic Survey of Canada, Energy, Mines and Resources Canada, Ottawa.

Delikaraoglou, D. (1985b). Personal communication with the geoid group of the Department of Surveying Engineering. Geodetic Survey of Canada, Energy, Mines and Resources Canada, Ottawa, 20 December.

Ecker, E. and E. Mittermayer (1969). "Gravity corrections for the influence of the atmosphere." *Boll. Geofisica Teor. Appl.* XI, pp. 70-79.

Engelis, T. (1983). "Analysis of sea surface topography using SEASAT altimeter data." Department of Geodetic Science and Surveying, Report No. 343, The Ohio State University, Columbus, Ohio, U.S.A.

Hearty, D.B. (1985). Personal communication. Division of Gravity, Geothermics and Geodynamics, Earth Physics Branch, Energy, Mines and Resources Canada, Ottawa.

Hearty, D.B. (1986). Personal Communication. Division of Gravity, Geothermics and Geodynamics, Earth Physics Branch, Energy, Mines and Resources Canada, Ottawa.

Heiskanen, W.A. and H. Moritz (1967). *Physical Geodesy.* Freeman.

International Association of Geodesy (1971). "Geodetic Reference System 1967." IAG Special Publication No. 3, Paris.

John, S. (1976). "Geoid determination for eastern Canada from astrogeodetic deflections of the vertical, gravity anomalies and Doppler satellite observations." M.Sc. thesis, Department of Surveying Engineering, University of New Brunswick, Fredericton.

Lerch, F.J., S.M. Klosko, R.E. Laubscher and C.A. Wagner (1979). "Gravity model improvement using GEOS-3 (GEM9 and 10)." *Journal of Geophysical Research,* 84(B8), pp. 3897-3916.

Lerch, F.J., S.M. Klosko, C.A. Wagner and G.B. Patel (1984). "Verification of the accuracy of Goddard satellite models." Presented at the American Geophysical Union Fall Meeting, San Francisco.

Levitus, S. (1982). "Climatological atlas of the world oceans." NOAA Professional Paper 13, U.S. Department of Commerce, Washington, DC, U.S.A.

Lorell, J., M.E. Parke and J.F. Scott (1980). "SEASAT Geophysical data record (GDR) users handbook (altimeter)." Jet Propulsion Lab Document 622-97, Revision A, Pasadena, CA, U.S.A.

Marsh, J.G. (1985). Personal communication. Goddard Space Flight Center, Greenbelt, MD, U.S.A.

Marsh, J.G., A.C. Brenner, B.D. Beckley and T.V. Martin (1984). "Global mean sea surface based on the SEASAT altimeter data." Goddard Space Flight Center, Greenbelt, MD, U.S.A., preprint.

Merry, C.L. (1975). "Studies towards an astrogravimetric geoid for Canada." Department of Surveying Engineering Technical Report 31, University of New Brunswick, Fredericton.

Molodenskij, M.S., V.F. Eremeev and M.I. Yurkina (1962). "Methods for the study of the external gravitational field and figure of the earth." English translation by Israel Program for Scientific Translations, Jerusalem

Moritz, H. (1980). "Geodetic Reference System 1980." *Bulletin Géodésique,* 54, pp. 395-405.

Najafi, M.A. (1981). "Local evaluation of the geoid from gravity data." M.Sc.E. thesis, Department of Surveying Engineering, University of New Brunswick, Fredericton.

Paul, M.K. (1973). "A method of evaluating the truncation error coefficients for geoidal height." *Bulletin Géodésique,* 57, pp. 413-425.

Rapp, R.H. (1982a). "A global atlas of sea surface heights based on the adjusted SEASAT altimeter data." Department of Geodetic Science Report No. 333, The Ohio State University, Columbus, Ohio, U.S.A.

Rapp, R.H. (1982b). "A summary of the results from the OSU analysis of SEASAT altimeter data." Department of Geodetic Science Report No. 335, The Ohio State University, Columbus, Ohio, U.S.A.

Rapp, R.H. (1983). "The development of the January 1983 1 x 1 mean free-air anomaly data tape." Internal Report of the Department of Geodetic Science and Surveying, The Ohio State University, Columbus, Ohio, U.S.A.

Rapp, R.H., and R. Rummel (1975). "Methods for the computation of detailed geoids and their accuracies." Department of Geodetic Science Report No. 233, The Ohio State University, Columbus, Ohio, U.S.A.

Rowlands, D. (1981). "The adjustment of SEASAT altimeter data on a global basis for geoid and sea surface height determinations." Department of Geodetic Science Report No. 325, The Ohio State University, Columbus, Ohio, U.S.A.

Sosa-Torres, R. (1977). "Geoid determination from heterogeneous data." M.Sc. thesis, Department of Surveying Engineering, University of New Brunswick, Fredericton.

Tapley, B.D., G.H. Born and M.E. Parke (1982). "The SEASAT altimeter data and its accuracy assessment." *Journal of Geophysical Research,* 87, C5, pp. 3179-3188.

Tscherning, C.C., R.H. Rapp and C. Goad (1983). "A comparison of methods for computing gravimetric quantities from high degree spherical harmonic expansions." *Manuscripta Geodaetica*, 8, pp. 249-272.

U.S. National Research Council (1985). *Geodesy: A Look to the Future.* Committee on Geodesy, National Academy Press, Washington, DC, U.S.A.

Vaníček, P. and S. John (1983). "Evaluation of geoid solutions for Canada using different kinds of data." *Proceedings of symposium on Improved Gravity Field Estimation on Global Basis,* Vol. 2, Hamburg, August, pp. 609-624.

Vaníček, P. and E.J. Krakiwsky (1982). *Geodesy: The Concepts.* North-Holland, Amsterdam.

Vaníček, P. and C.L. Merry (1973). "Determination of the geoid from deflections of the vertical using a least-squares surface fitting technique." *Bulletin Géodésique,* 109, pp. 261-279.

Winter, P.J. (1979). Personal communication. Science and Technology, Energy, Mines and Resources Canada, Ottawa.

Yazdani, R., N. Christou and E. Derenyi (1986). "Processing of SEASAT altimetry data on a digital image analysis system." Paper to be presented at the 10th Canadian Symposium on Remote Sensing, Calgary, Alberta, May.